CHALMERS
UNIVERSITY OF TECHNOLOGY

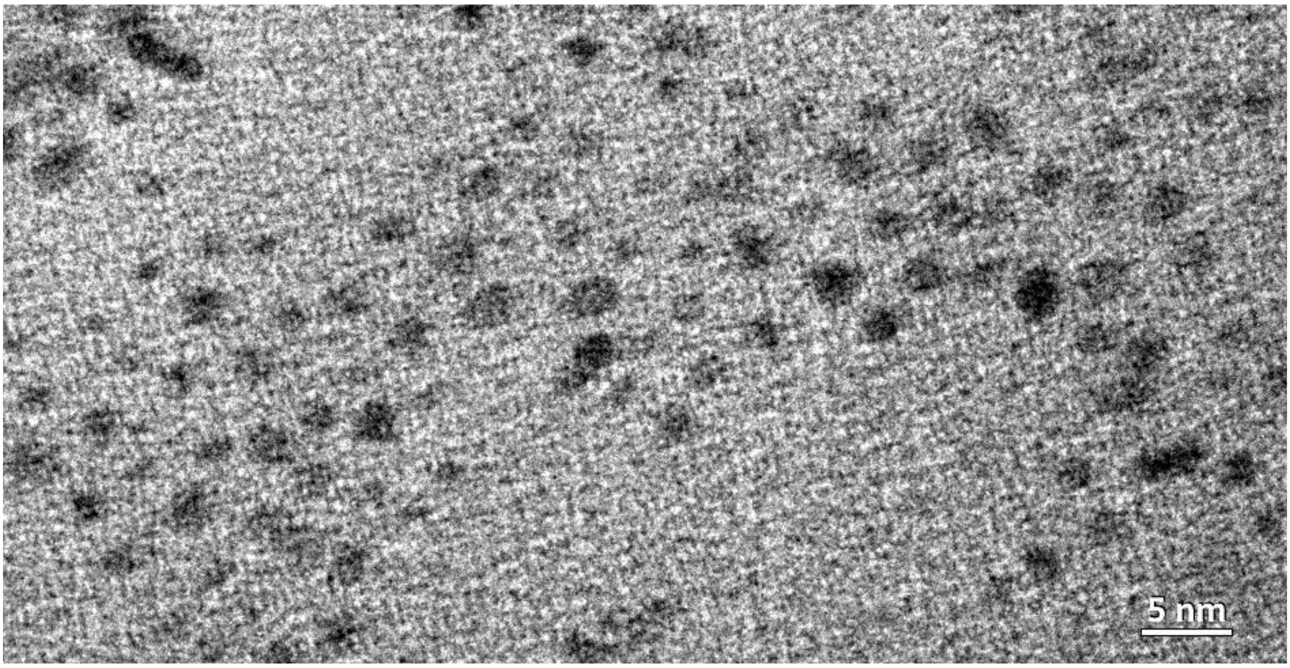

Pt / Pt_3Y Fuel Cell Nanoparticle Catalyst Fabrication via Sputter Deposition onto Liquid Substrates

Master's thesis in Materials Engineering

ROBIN PFEIFFER

DEPARTMENT OF PHYSICS
DIVISION OF CHEMICAL PHYSICS

CHALMERS UNIVERSITY OF TECHNOLOGY
Gothenburg, Sweden 2020
www.chalmers.se

DEPARTMENT OF PHYSICS
DIVISION OF CHEMICAL PHYSICS
CHALMERS UNIVERSITY OF TECHNOLOGY
Gothenburg, Sweden
www.chalmers.se

MASTER’S THESIS 2020

Pt / Pt_3Y Fuel Cell Nanoparticle Catalyst Fabrication via Sputter Deposition onto Liquid Substrates

ROBIN PFEIFFER

CHALMERS
UNIVERSITY OF TECHNOLOGY

Department of Physics
Division of Chemical Physics
CHALMERS UNIVERSITY OF TECHNOLOGY
Gothenburg, Sweden 2020

Pt / Pt_3Y Fuel Cell Nanoparticle Catalyst Fabrication via Sputter Deposition onto Liquid Substrates
ROBIN PFEIFFER

Supervisor: Rosemary Brown, Department of Physics, Chalmers University of Technology
Examiner: Björn Wickman, Department of Physics, Chalmers University of Technology

Master's Thesis 2020
Department of Physics
Division of Chemical Physics
Chalmers University of Technology
SE-412 96 Gothenburg
Sweden
Telephone +46 31 772 1000

Cover: Nanoparticles fabricated by sputtering of Pt onto 1-Ethyl-3-methylimidazolium triflate
Gothenburg, Sweden 2020

Pt / Pt_3Y Fuel Cell Nanoparticle Catalyst Fabrication via Sputter Deposition onto Liquid Substrates

ROBIN PFEIFFER
Department of Physics
Division of Chemical Physics
Chalmers University of Technology

Abstract

This thesis presents an overview on the fabrication of Pt and Pt_3Y nanoparticles via sputtering onto liquid substrates for potential use as catalyst of the oxygen reduction reaction in modern fuel cells. It is shown that spherical nanoparticles with diameters in the range of 1 – 4 nm can be formed by sputtering onto different liquids. Ionic liquids as well as polyethylene glycol proved to be suitable substrates for Pt nanoparticles. However, Pt_3Y reacted with ionic liquids to form undesirable structures and compounds. Sputtering of Pt_3Y onto polyethylene glycol resulted in the formation of nanoparticles without any unwanted reactions. Compared to an ionic liquid substrate, polyethylene glycol produced nanoparticles with a slightly broader particle size distribution due to less effective stabilization mechanisms. Summarized, the liquid polymer turned out to be the best liquid substrate candidate for the formation of Pt_3Y nanoparticles.

The size of the nanoparticles varied slightly with the applied liquid substrate without exhibiting significant trends. Furthermore, the size increased by roughly 20 – 30% by means of a post heat-treatment at 165 °C. An elevated sputtering power resulted in larger particle sizes but an unchanged particle concentration, which points out a particle formation and growth mechanism at the liquid surface. This suggestion could be validated by an investigation of the visual appearance of the sputtered wafers. The nanoparticles fabricated in polyethylene glycol exhibited an electrocatalytic activity for the oxygen reduction reaction in an acidic environment in rotating disc electrode measurements. Alloying the nanoparticles with Y led to an activity enhanced by a factor of 1.67 compared to pure Pt nanoparticles. This proves the particles' potential application in fuel cells and provides motivation for further research on this topic.

Keywords: fuel cell, catalysis, nanoparticles, platinum, yttrium, sputter deposition, liquid substrate, ionic liquid, polyethylene glycol

Acknowledgements

I would like to thank my supervisor, Rosemary Brown, for offering this master's thesis topic to me, and primarily for the interest in and help with my research. Thank you for your helpful advices and meaningful reflections, for assisting me with my experiments and supporting me in my daily work. The same applies to my examiner, Björn Wickman, who invariably had an open ear for questions, problems as well as achievements with my research and gave valuable suggestions for both my experimental and theoretical work. Furthermore, special thanks are directed to Gerard Montserrat Sisó, who always took the time to answer my questions in and around the laboratory and conducted numerous measurements connected to my work.

Finally, I want to thank the rest of my colleagues at the division of Chemical Physics for creating a comfortable and welcoming atmosphere. It was a great pleasure to work with you and I enjoyed coming to the office every day.

Robin Pfeiffer, June 2020

Contents

I List of Abbreviations

[Bmim] [Tf_2N]	1-Butyl-3-methylimidazolium bis(fluoromethylsulfonyl)imide
[Dmim] [OTf]	1-Decyl-3-methylimidazolium triflate
[Dmim] [Tf_2N]	1-Decyl-3-methylimidazolium bis(fluoromethylsulfonyl)imide
[Emim] [FAP]	1-Ethyl-3-methylimidazolium tris(pentafluoroethyl)-trifluorophosphate
[Emim] [OTf]	1-Ethyl-3-methylimidazolium triflate
[Emim] [Tf_2N]	1-Ethyl-3-methylimidazolium bis(fluoromethylsulfonyl)imide
Ag	silver
Ar	argon
$at\%_i$	atomic percent of substance i
Au	gold
CO	carbon monoxide
CPS	counts per second
Cu	copper
CV	cyclic voltammetry
DLS	dynamic light scattering
e^-	electron
EDX	energy-dispersive X-ray spectroscopy
EtOH	ethanol
FWHM	full width at half maximum
GCE	glassy carbon electrode
H^+	proton
H_2	hydrogen
H_2O	water
IL(s)	ionic liquid(s)
IPA	2-propanol
MEA	membrane electrode assembly
N_2	nitrogen
NP(s)	nanoparticle(s)
O_2	oxygen
ORR	oxygen reduction reaction
Pd	palladium
PEG	polyethylene glycol
PEM	proton exchange membrane
Pt	platinum
RDE	rotating disc electrode
RHE	reversible hydrogen electrode
SAXS	small angle X-ray scattering
Si	silicon
TEM	transmission electron microscopy
UV	ultraviolet
UV-Vis	ultraviolet-visible
$wt\%_i$	weight percent of substance i
XPS	X-ray photoelectron spectroscopy
XRD	X-ray diffraction
XRF	X-ray fluorescence spectroscopy
Y	yttrium

II List of Figures

III List of Tables

1 Introduction

1.1 Background and problem overview

Today, there are high demands to find technologies suitable to maintain an ecologically well-balanced planet for future generations [1]. Since fossil fuels have been the dominant source of energy for the past 150 years [2], the transition to renewable energy requires a lot of effort and research for a successful and sensible implementation of novel techniques [3].

Fuel cells represent one promising technology for sustainable power generation [4]. The basic principle of a fuel cell is to convert chemically stored energy into electrical energy. It hence acts as an electrochemical energy converter finding potential application mainly in transportation [4, 5]. The function of a fuel cell is solely dependent on the evolution of hydrogen, which can be produced from renewable energy for example. With water being the only reaction product during operation, the technology does not produce any environmentally harmful combustion products such as carbon dioxide (CO_2), nitrogen oxides (NO_x) or others [6, 7].

The history of fuel cells goes back to the 1830s, when both Christian Friedrich Schönbein and Sir William Robert Grove discovered the underlying fundamental principles [8]. One hundred years later, the first fuel cell of practical use was developed by Thomas Francis Bacon [8]. Since the mid-20th century, numerous new types of fuel cells have been established and continuous research has been conducted on improving their performance [5, 8].

Due to several advantages such as high efficiency, the proton exchange membrane (PEM) fuel cell is the most commonly used cell type today [5]. The basic principle relies on a redox reaction, in which oxygen is reduced at the cathode by the formation of water [9]. This is the oxygen reduction reaction (ORR) - it exhibits slow kinetics and has been determined to be key to improving the overall performance of PEM fuel cells [10, 11]. For this reason, the catalysis of the ORR is an important issue for successfully applying fuel cells in large scale.

To date, Platinum (Pt) is the most used catalyst material for the ORR. However, since Pt is quite expensive, alternative catalyst materials are necessary in order to make fuel cells commercially competitive [9]. One approach to this problem is alloying Pt with other metals. It has been shown that for example Pt alloyed with rare earth (RE) elements can form stable nanoparticles (NPs) exhibiting a significant increase in catalytic activity compared to pure Pt NPs [12, 13]. This makes Pt_3Y a promising material for the explained purpose. However, the size, shape and composition of the NPs are crucial parameters that need to fulfill narrow criteria in order to achieve the desired high activity [12, 13]. For this reason, any method to produce Pt_3Y NPs needs to be capable of controlling the mentioned parameters very precisely. The development of such a technique being scalable (and thus industrially useful) at the same time remains very challenging [13].

1.2 Goal of the thesis

There have been several attempts to produce Pt_3Y NPs with favorable catalytic activity for the ORR. Some have been partially successful, however, they mostly lack scalable production and require laborious methods [14]. This thesis presents a study into a new method for Pt_3Y NP production, using vacuum sputtering onto liquid substrates. Hereby, an assessment of whether and under which conditions these NPs can be fabricated is contemplated. A variety of liquid substrates as well as sputtering parameters are investigated as variables to influence and tune the NPs' characteristics. Since this work deals with a very novel field of research, an important part is to define suitable analysis methods and sample preparation techniques. It is intended to determine typical sizes, size distributions and compositions of the NPs to find optimal conditions for the fabrication of favorable particles within the given boundaries. For Pt_3Y, the issue of the chemical state of yttrium (Y) in the NPs is addressed since the presence of metallic Y is indispensable for the given application. Finally, this thesis seeks answers to the question whether the NPs can be successfully transferred from the liquid substrate to a catalyst ink and examines the capability of the particles to catalyze the ORR in acidic conditions in practice.

Firstly, the necessary background will be presented in order to introduce the fuel cell catalyst systems in question and the applied fabrication technique in chapter 2. This will include the basics of PEM fuel cells and the ORR, the Pt-Y system as well as different aspects of sputtering onto liquid substrates. Then, the applied methods will be clarified in chapter 3, which contains information on practical procedures for sample preparations, analysis methods and data treatment. The results of the conducted experiments will be presented and discussed in chapter 4. This will start with pre-investigations of the system and materials in use, followed by the investigation of Pt_3Y and Pt NPs formed under different conditions. The chapter will be finalized by examinations of the particle formation and growth mechanism as well as an electrochemical characterization of the fabricated NPs. The thesis will close with a summary of the most important results and outcomes in chapter 5.

2 Theory

This chapter provides the relevant theoretical backgrounds for this work. On the one hand, the fundamentals of the applications this work aims to support and enable are explained. On the other hand, the applied methods and materials are elucidated and motivation for applying them is given.

2.1 The proton exchange membrane fuel cell

Even though a remarkably high number of different types of fuel cells exists nowadays, PEM fuel cells have certainly attracted the most attention during the last decades [5]. Despite being a comparatively novel development, a lot of effort has been made to improve the PEM fuel cell performance, i.e., the catalysis taking place inside the cell in the first place [5].

The basic idea of a PEM fuel cell is the same as for all other fuel cell types. A redox reaction being split up into two half-reactions takes place, where each half-reaction occurs at opposite electrodes. The hereby required electron-flow and ion-flow from one electrode to the other are separated, which offers the possibility to utilize the moving electrons (e^-) to generate electricity and drive a load [15].

The most commonly used fuel in fuel cells is hydrogen (H_2) gas [6, 15]. The fuel is transported to the anode, where the oxidation half-reaction takes place [5]:

$$H_2 \rightarrow 2H^+ + 2e^- \tag{2.1}$$

Oxygen (O_2) is supplied to the cathode and is reduced in the presence of protons (H^+) as well as electrons [5]:

$$\frac{1}{2}O_2 + 2H^+ + 2e^- \rightarrow H_2O \tag{2.2}$$

Combining the two half-reactions (2.1) and (2.2), the net reaction (2.3) is as follows:

$$H_2 + \frac{1}{2}O_2 \rightarrow H_2O \tag{2.3}$$

Summarizing the information above, the fuel cell runs on hydrogen and oxygen, producing water (H_2O) as an emission and electricity.

The main difference between the several fuel cell types is the electrolyte and membrane separating the electrodes and half-cell reactions from each other [15]. In a PEM fuel cell, a membrane is responsible for the transport of the protons from the anode to the cathode. At the same time, it must exhibit a low electrical conductivity, a low permeability to the applied gases as well as chemical stability towards the present chemical substances [7]. Perfluorinated sulfonic acids - mostly Nafion - have been shown to offer a good combination of those properties, which is why they are typically used in modern PEM fuel cells [16]. The acidic character of the membrane determines the pH value inside the active part of the cell, which typically lies in the range of zero [17]. PEM fuel cells are operated at temperatures below 100 °C and hence belong to the low temperature fuel cells [4, 15].

The catalyst-coated electrodes together with the PEM form the so-called Membrane Electrode Assembly (MEA). The general schematic setup and functionality of a PEM fuel cell is illustrated in Figure 1(a).

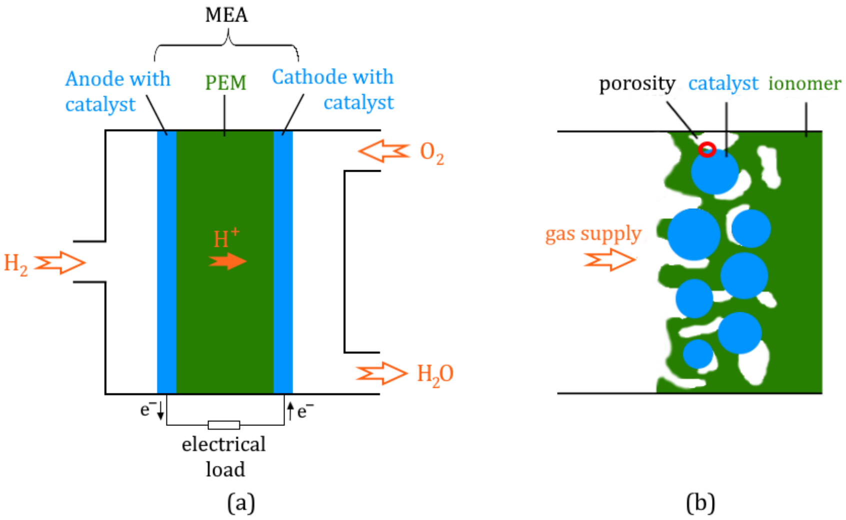

(a)

(b)

Figure 1: Schematic setup of a PEM fuel cell [5, 17]: (a) General setup; (b) Triple phase boundary.

For the reactions (2.1) and (2.2) to run efficiently, the ionomer as the proton conductor, the catalyst as the electron-conductor and the reaction gas need to have common contact areas, the so-called triple phase boundaries [4]. Figure 1(b) shows a zoomed-in image of the corresponding part of Figure 1(a) with an example of a triple phase boundary marked by the red circle. For the implementation in the fuel cell, the catalyst nanoparticles need to be embedded in a supporting structure. For this purpose, carbon is normally applied, utilizing its suitable electrical conductivity, high surface area and corrosion resistance [4].

2.1.1 The oxygen reduction reaction and its catalysis

The reaction given in equation (2.2) is commonly termed oxygen reduction reaction (ORR) [15]. This reaction runs slowly in PEM fuel cells [11, 18] and much research has been done to gain insight into the reaction mechanism [5, 17, 18]. A detailed understanding of the reaction is indispensable to effectively design suitable catalysts. However, it is far from trivial to determine the exact mechanism [19]. Different reaction pathways have been proposed and also the mechanism is likely to depend on the prevailing conditions the reaction takes place in [17]. Making some reasonable assumptions leads to the following associative mechanism, where the * symbolizes a vacant surface site on a catalyst [9, 18].

$$O_2 + {}^* \rightarrow O_2^* \tag{2.4}$$

$$O_2^* + H^+ + e^- \rightarrow HOO^* \tag{2.5}$$

$$HOO^* + H^+ + e^- \rightarrow H_2O + O^* \tag{2.6}$$

$$O^* + H^+ + e^- \rightarrow HO^* \tag{2.7}$$

$$HO^* + H^+ + e^- \rightarrow H_2O + {}^* \tag{2.8}$$

Since four electrons are transferred in the scheme above, this is mostly referred to as the four electron pathway [17].

The ORR being the key reaction in terms of fuel cell performances, it is worth considering some of its properties in more detail. Thermodynamics determine the theoretical maximum voltage generated by a single cell, which is 1.23 V owing to equation (2.3) and the galvanic series [20]. However, under operating conditions, this voltage is lower due to losses originating mainly from the kinetics of the ORR [17]. Low electron transfer coefficients lead to sluggish electrode kinetics of the ORR, which in turn results in high potential losses according to the Tafel equation [21]. The overpotential losses are illustrated in Figure 2.

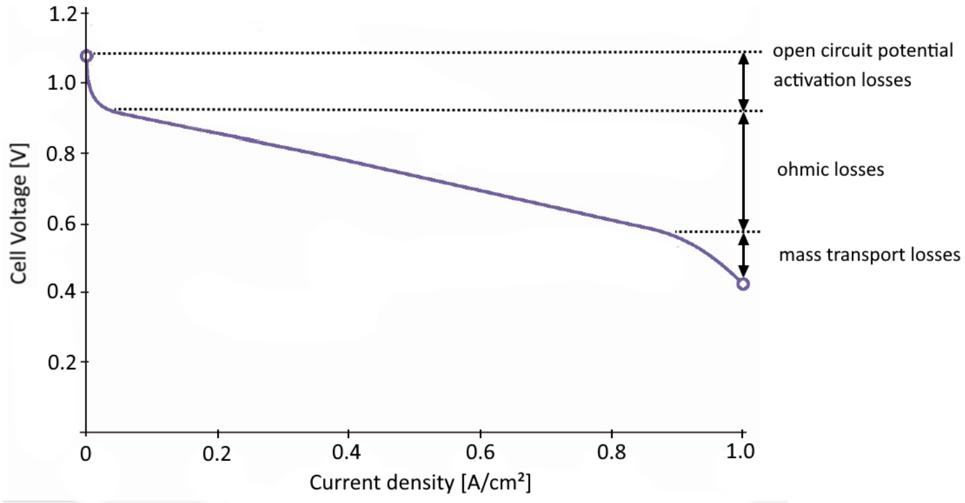

Figure 2: Typical polarization curve for a PEM fuel cell. Adapted from [22].

The open circuit potential is lower than the thermodynamically predicted 1.23 V due to hydrogen crossover from the anode to the cathode [23]. Additional losses are of ohmic and mass transport reasons as well as due to an activation overpotential [4, 5].

The ORR exhibits slow kinetics at the typical operation temperatures, especially compared to the second half-reaction, the hydrogen oxidation reaction [11, 18]. Therefore, the ORR has been determined to be key to improving the overall performance of PEM fuel cells [10, 11]. An important approach to this problem is the application of catalysts to accelerate the ORR.

Generally, a catalyst is a substance that accelerates a chemical reaction by offering a more complex, but energetically more favorable reaction mechanism. In this way, it affects the kinetics of the concerning reaction - the thermodynamics on the other hand remain unchanged. Since a catalyst supports the reaction, but is not actively involved, it is left in its initial state and is not used up during the proceeding reaction.

Noble metals are typically applied as catalysts in fuel cells [4]. To date, Pt is the most used material for the catalysis of the ORR since the metal exhibits superior stability and catalytic activity compared to other materials [18, 24]. NPs are of special interest as they offer a very high specific surface area and therefore a large number of active surface sites for the reaction [17, 25]. In modern PEM fuel cells, a Pt loading of about 0.2 mg/cm^2 [26] and a specific surface area of roughly 90 m^2/g [15] is required at the cathode. In terms of particle size it has been shown that a diameter of roughly 3 nm leads to a peak performance regarding the catalytic activity of Pt NPs [12].

The quality of an electrocatalyst such as Pt for the ORR is typically described by the current density of the reaction of interest [9]. The higher this quantity, the more electrons flow per catalyst area per time, which means a higher catalytic activity. Therefore, cyclic voltammetry (CV) and rotating disc electrode (RDE) measurements are commonly used tools to characterize a catalyst for the ORR. A typical cyclic voltammogram in an inert gas as well the ORR polarization curve for a Pt catalyst are shown in Figure 3 [27].

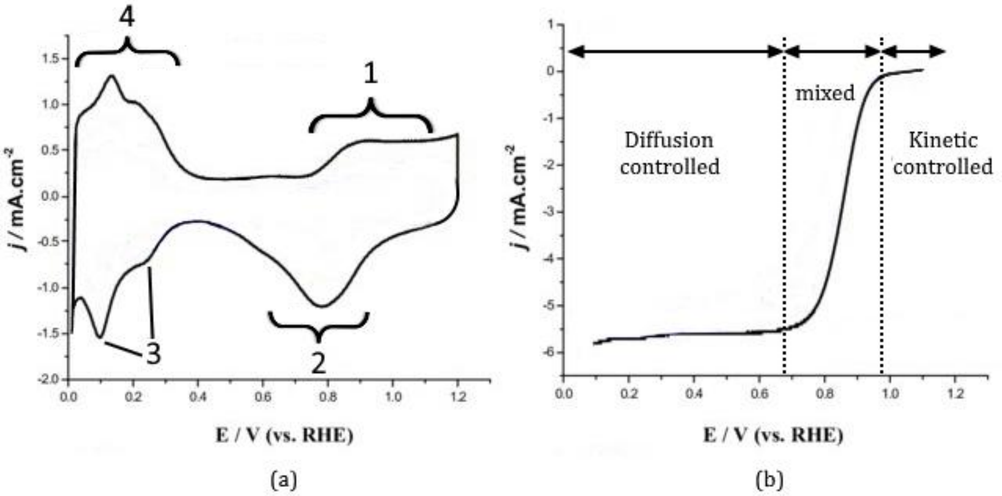

(a) (b)

Figure 3: Electrochemical characterization of a Pt catalyst in aqueous acidic solution: (a) Typical cyclic voltammogram in intert gas; (b) ORR polarization curve. Adapted from [27].

The peaks of the cyclic voltammogram Figure 3(a) are assigned in Table 1 [28, 29]. The ORR polarization curve in Figure 3(b) is characterized by a kinetic and a diffusion controlled regime as well as a mixed area. In the kinetic-limited area, the reaction rate of the ORR is very low due to kinetic hindrance. When decreasing the potential, the reaction rate increases since kinetics represent a smaller barrier in the mixed regime. At even lower potentials, the mass transport of the reacting species limits the rate of the ORR, which is why a plateau is reached in the diffusion-controlled area [30].

Table 1: CV peak assignment for Pt catalyst [28, 29].

Peak number	Electrochemical process
1	water adsorption and Pt oxidation
2	reduction of Pt oxide
3	hydrogen adsorption on Pt
4	hydrogen oxidation and desorption from Pt

Since Pt is very expensive, it is responsible for the high production cost of PEM fuel cells [19]. One possibility to reduce the expenses could be the usage of other, cheaper materials. Alternatively, an enhancement of the catalytic activity for the same base material would reduce the necessary catalyst loading and thereby result in lower costs as well. The latter approach can even be applied to Pt-based catalysts since the currently used pure Pt NPs are not unbeatable when it comes to catalytic activity [13, 19, 26].

The origin of the possibility to increase the catalytic performance of Pt for the ORR is the high stability of some formed intermediates, namely the adsorbed oxygen and hydroxyl species (compare equations (2.4)-(2.8)) [18]. For an optimum catalytic effect, the strength of adsorption of the intermediates to the catalyst surface is subject to a tradeoff. It should be high enough to allow for the adsorption and reaction of the respective species, but still not prevent desorption of the reaction products afterwards, which would then block the active sites [5]. This is generally called the Sabatier's principle [31]. In the case of the ORR, Pt already exhibits a well-suited balance between those two factors compared to other pure metals, which is why it is currently used in fuel cells [18]. The strongest additional increase of the catalytic activity can be achieved for an adsorption energy of oxygen to the catalyst surface of 0.2 eV lower than for pure Pt(111), which could be shown both experimentally and by a computational screening [32]. Graphically, this behavior can be illustrated by a so-called volcano plot given in Figure 4.

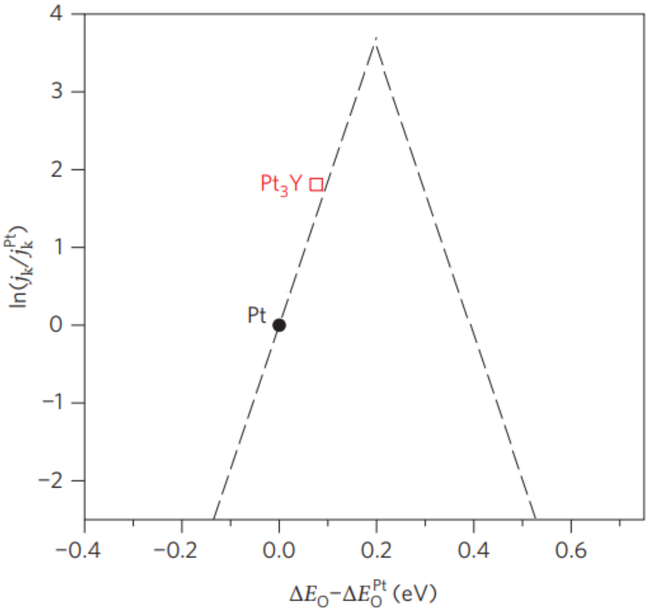

Figure 4: Volcano plot of the ORR for different Pt alloys. Adapted from [32].

In Figure 4, the dashed line indicates theoretical calculations. Already Pt is positioned at fairly high catalytic activities in the volcano plot (compared to other pure metals), indicating once more the suitability of Pt for the catalysis of the ORR [33]. Furthermore, a datapoint for Pt_3Y is plotted, which represents bulk polycrystalline Pt_3Y tested by RDE measurements [32]. A shift towards higher catalytic activities for Pt_3Y compared to Pt can be observed. The reasons for this behavior are explained in the following chapter.

2.2 The Pt-Y system in catalysis

As introduced in chapter 2.1.1, Pt_3Y is a promising material for the catalysis of the ORR. The Pt:Y ratio of 3:1 implies an atomic concentration of Pt of 75 at%. Figure 5 shows the crystal structure of bulk Pt_3Y with the (111) facet at the surface since this is the most investigated Pt_3M surface (M = metal) related to the catalysis of the ORR [19].

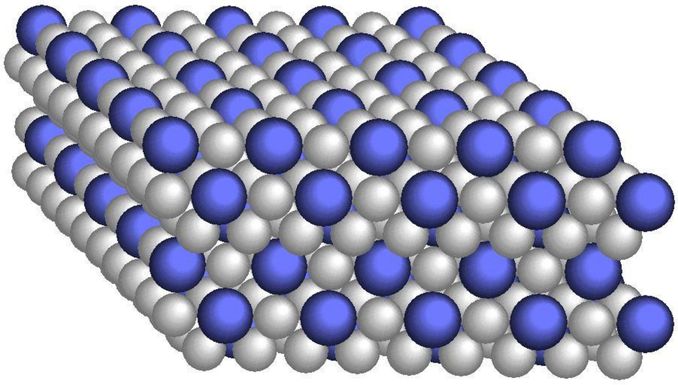

Figure 5: Crystal structure of Pt_3Y (blue: Y atoms; grey: Pt atoms).

The usage of rare earth (RE) elements as alloying elements in electrocatalysts is not a novel idea and was first applied already in the 1970s - not for the catalysis of the ORR though [34]. Over the years, more and more relationships between catalyst properties and their catalytic activity have been investigated and unraveled [35]. The RE elements however lost attention and for several decades were not considered as helpful for the catalysis of the ORR [34, 35]. This changed drastically in 2009, when Greeley et al. studied oxygen reduction electrocatalysts in a new way [32]. Via a computational screening, they investigated several properties of palladium (Pd) or Pt alloys. As a result, they suggested Pt-RE alloys having both an increased catalytic activity compared to pure Pt and a superior stability to other alloys. In particular Pt_3Y and Pt_3Sc turned out to be the most stable of all the Pt alloys [32]. Beside a good catalytic performance, stability is extremely important since alloys tend to suffer from degradation via Ostwald ripening or dealloying over time [13]. The highly negative enthalpy of formation for the two mentioned Pt alloys (especially compared to Pt late transition metal alloys [36]) makes them less prone to this phenomenon [13]. This discovery, combined with an adequate abundance of some RE elements like Y for example [37], revitalized the interest in Pt-RE alloys for the catalysis of the ORR and led to intensive research in this area and the underlying mechanisms.

At this point, the issue of how Pt_3Y provides an enhanced catalytic activity is addressed. In general, the introduction of another element to the pure Pt catalyst can affect the catalytic activity by three different effects [35]. The alloying element can alter the composition of an adsorption site itself, which leads to a change of the surface's properties. This is called the ensemble effect [35, 38]. Alternatively, the ligand effect is a result of the interaction of an adsorption site with neighboring species. Interactions between a Pt and an adjacent Y atom can affect the electronic landscape and therefore the catalytic activity [35, 38, 39]. Finally, strain effects can be of importance since lattice strains have the potential to affect the geometrical and the electronic surface structure [35].

Nowadays, there is strong evidence that the described superior properties of Pt_3Y are a result of a thin Pt overlayer forming on top of the Pt_3Y alloy structure [12, 40–42]. This overlayer forms due to oxidation of the alloy surface. Y oxidizes easily in contact with oxygen (e.g., air) - Pt does not [43]. Oxidized Y, which is confined to the surface, can be dissolved in an acidic environment and is therefore leached from the alloy surface. Pt in contrast is unaffected under acidic conditions (see Pourbaix diagrams for more details [44, 45]). Due to these relations, an acid-treatment of a Pt_3Y alloy removes Y-oxide. Pt atoms remain at the surface and re-arrange to from an overlayer which sits on top of un-oxidized alloy. In literature this is also referred to as a Pt skin [41]. The overlayer has a protective effect, which means that it can prevent further leaching of the less noble element (here Y) [14, 35, 37]. The thickness of the overlayer depends on different parameters like roughness of the surface for example [40]. However, a typical thickness is in the order of a few atomic layers, which corresponds to approximately 1 – 3 nm [12, 14]. A schematic visualization of the overlayer on top of the alloy structure with the (111) facet parallel to the surface is shown in Figure 6.

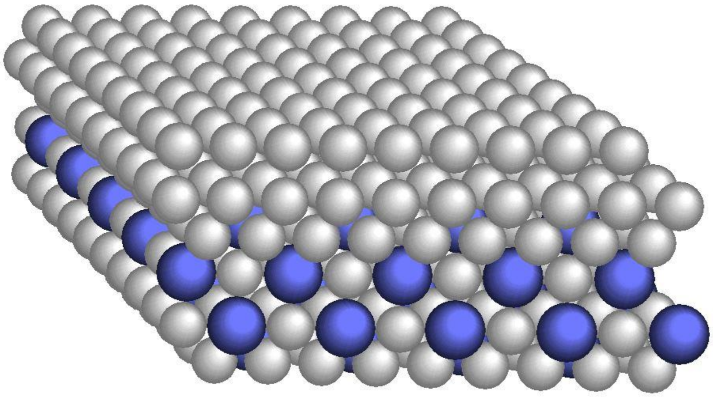

Figure 6: Crystal structure of Pt_3Y with Pt overlayer (blue: Y atoms; grey: Pt atoms).

The surface overlayer composed of pure Pt has an increased catalytic activity for the ORR due to the strain effect described above (the ensemble and ligand effect require the alloy to be directly at the surface) [35]. The bulk Pt_3Y alloy induces a compressive strain in the Pt overlayer due to lattice mismatch and the Pt-Pt nearest-neighbor atomic distance is decreased [10, 34].

It is commonly known that interatomic distances are a key parameter for the adsorption of molecules to the surface [4]. In 1983, Jalan and Taylor showed a correlation between the catalytic activity and the nearest-neighbor distance for Pt-alloys [46]. Leading to a decreased nearest-neighbor distance, a compressive strain causes an energetic downshift of the Pt d-band center compared to unstrained, bulk Pt [35, 47]. According to the d-band model, such a downshift reduces the interaction strength between the catalyst surface and an adsorbent in the case of late transition metals (such as Pt) [35, 48]. From this, it follows that the compressive strain enables an increased catalytic activity. In fact, Y has a larger atomic radius than Pt [49], however, the larger Y atoms distort the fcc structure of pure Pt in a way, that fits more Pt atoms into the overlayer compared to bulk Pt [12].

2.2.1 Pt_3Y nanoparticles for the catalysis in fuel cells

As explained in the previous chapter, the formation of the Pt overlayer results in an improvement of the specific catalytic activity compared to pure Pt. For thin films, an enhancement by a factor of 2.5 compared to pure Pt tested under real fuel cell conditions has been reported [42]. Similar holds for NPs - here an improvement factor of ~6 was determined compared to pure Pt NPs [12]. However, to reach such high values, the dimensions of the Pt_3Y structures must meet certain requirements. If the amount of alloy material underneath the overlayer is too little, there is not sufficient strength of the alloy to force the compressive strain on the overlayer. For this reason, Pt_3Y NPs should be significantly larger than pure Pt NPs for their optimum catalytic activity. Hernandez-Fernandez et al. determined an increasing specific activity up to a particle size of 8 – 9 nm [12]. Larger particle sizes might even increase the strain effect, but this is a trade-off with a decreasing surface area. Furthermore, larger NPs tend to form nanoporous structures instead of a core-shell assembly [37] and a too high strain imposed by the alloy core can possibly lead to a relaxation of the overlayer [10].

A significant problem when producing Pt_3Y NPs is the high affinity of Y to oxygen [13]. It is important that any method does not allow for bulk / core Y to oxidize to maintain the alloy core and attain an enhanced catalytic activity. Therefore, a suitable fabrication process must be conducted in the absence of any oxygen [36]. Chemical methods, which would be convenient for a scalable fabrication of the NPs, mostly fail at this hurdle [13, 43]. Only very recently, Hu et al. published a possibility, which they state to be suitable to produce Pt_3Y NPs of controllable properties containing metallic Y in a chemical approach [37]. This work could represent a remarkable progress regarding Pt-RE NP catalysts. However, further investigations in this topic are still of great interest since this is a very novel field of research with huge potential for improvements [12].

Physical methods may generally be more suitable to overcome the oxidation problem. There are a few reports on a successful preparation of Pt_3Y NPs via physical routes – the gas aggregation technique and co-sputtering onto a solid substrate have been applied [12, 43, 50]. These methods led to satisfactory results on a small scale but are not suitable for the production of larger quantities [37, 43]. Vacuum sputtering is a standard industrial technique being scalable and not involving any oxygen during processing. Therefore, the method of sputtering onto liquid substrates could be a promising approach for a successful fabrication of Pt_3Y NPs. It will be introduced and elucidated in the following chapter.

2.3 The sputter deposition method

As mentioned in chapter 2.2.1, sputtering onto liquid substrates is hoped to overcome some common difficulties in the production of Pt_3Y NPs for the utilization as a catalyst in fuel cells. To properly introduce this method, some basics of sputtering are presented first.

Sputter deposition is traditionally referred to as a thin film deposition technique, which is enabled by the bombardment of a target material with energetic species, typically ions [51]. The roots of modern sputtering go back to 1852, when W.R. Grove reported on film growth via sputtering for the first time [52]. The technology gained popularity very quickly and was already commercially applied starting from the end of the 19th century [52].

Sputtering involves a target material which is deposited onto a substrate in vacuum [53]. The vacuum is created inside the sputtering chamber [51] before a working gas is introduced. For normal sputtering, this is an inert gas (typically Argon (Ar)) that does not react with the target material [53]. A voltage is applied between two electrodes; the target acts as the cathode and the substrate holder as the anode [53]. The generated potential difference affects the electrons and ions existing from background ionization. Electrons are accelerated towards the anode, positively charged ions towards the cathode [51]. On their way through the sputtering chamber, electrons collide with Ar-atoms, which produces Ar^+ ions [51]. These ions bombard the target to knock atoms or clusters off the surface. Those liberated species move through the sputtering chamber towards the target and deposit there. In order to confine the electrons and ions constituting the plasma inside the sputtering chamber, magnets are commonly used. This helps to increase the sputtering rate and prevents excessive sputtering of the substrate [51, 53]. The basic setup of a magnetron sputtering system with a planar magnetron is given in Figure 7 [53].

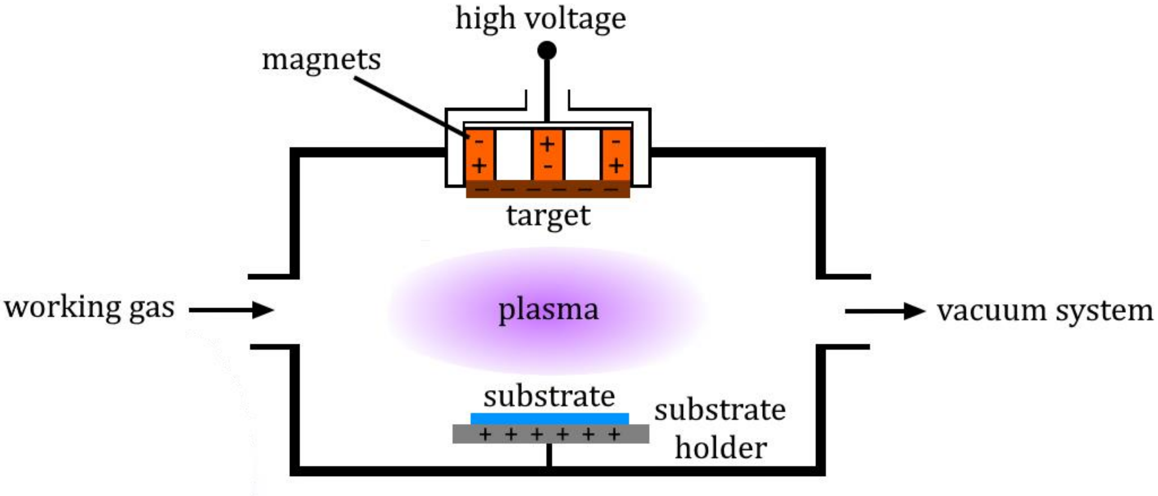

Figure 7: Magnetron sputtering system setup.

One of the most important quantities in sputtering is the sputtering yield, which is defined as the ratio of liberated target atoms to ions impinging on the target [51]. A fundamental approach with regard to the yield is the theory of Sigmund. The underlying equation (2.9) is valid for low ion energies and predicts a linear relationship between the yield Y and the ion energy E_g [51].

$$Y = C \cdot \frac{4 \cdot M_\mathrm{g} \cdot M_\mathrm{t}}{\left(M_\mathrm{g} + M_\mathrm{t}\right)^2} \cdot \frac{E_\mathrm{g}}{E_\mathrm{s}} \tag{2.9}$$

In equation (2.9) C is a constant, M_g and M_t are the masses of ion and target atoms and E_s is the surface binding energy of the target material. As can be seen in the equation, the sputtered material has an influence on the sputtering yield via the atomic mass and the surface binding energy. Even though the composition of the particle flux generally corresponds to the stoichiometry of the target [54], this might lead to the effect of preferential sputtering in the case of an alloy target [52, 54].

The parameter usually controlled during a sputtering experiment is the sputtering power, which is characterized by the discharge voltage and current and typically varies with the used target material [51]. In fact, this power does not primarily lead to the desired sputtering effect, but to heating of the target [53]. The target is thus usually cooled [53]. Similarly, the substrates can be heated during the sputtering process, mainly by the electrons being accelerated towards the anode [51]. This is important to consider when choosing the substrate material for a sputtering experiment. Especially when switching from solid to liquid substrates, this is an interesting aspect since liquids generally exhibit different thermal properties compared to solids. Owing to the higher amount of degrees of freedom in the liquid state, liquids typically show higher specific heat capacities than solids [55], which may reduce the described heating effect of the substrate.

Mostly, sputtering is used to deposit thin films on solid, flat substrates. However, a relatively new approach is to use liquid substrates. This was for the first time performed by Ye et al., who deposited silver onto silicon oil to form thin films [56]. This study opened a completely new direction of research in the sputtering area. Numerous investigations were set in motion and different liquid substrates were tested, such as silicon oil, vegetable oils, liquid polymers and ionic liquids [57–63]. To be used in a sputter chamber, the liquid must have a low vapor pressure to survive the vacuum conditions without evaporating quickly [57, 64]. Liquid substrates have been used to produce thin films, nanoclusters or NPs [57, 58, 61, 65], and the type of liquid as well as the sputtering parameters can determine the nature of the formed material [57, 61]. Important considerations regarding the choice of the liquid substrate will be given in chapter 2.4. More detailed information on the NP formation in the liquid using sputter deposition is provided in the following section 2.3.1.

2.3.1 Nanoparticle formation by sputtering onto liquid substrates

Sputtering onto liquid substrates offers the possibility to produce NPs directly in liquids that are suitable to stabilize those particles over a longer period of time. The species liberated from the target are deposited on the liquid substrate and their concentration is high enough to collide with each other, coalesce and form NPs [66]. For the formation and growth of the particles, the three possibilities illustrated in Figure 8 come into consideration. In path (a), nucleation takes place on the liquid surface. The clusters then sink into the liquid where they grow to NPs. Variant (b) is characterized by nucleation and growth on the liquid surface, before the NPs move into the bulk liquid. In mechanism (c) the sputtered species directly penetrate the bulk liquid, where nucleation and growth of the NPs occur [64]. Independent of the mechanism, the growth of the particles proceeds until the NPs are stabilized by the liquid [65].

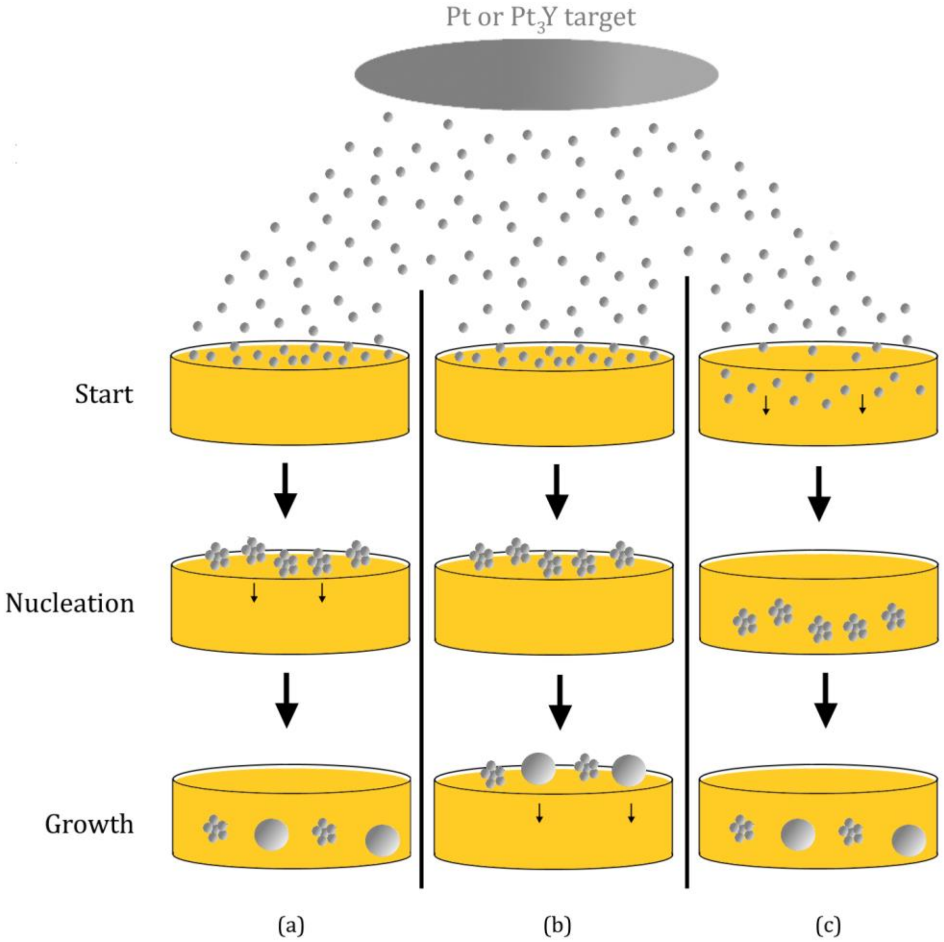

Figure 8: NP formation via sputtering onto a liquid substrate. Adapted from [64].

Torimoto et al. were the first to discover the formation of NPs via the sputter deposition technique onto ILs in 2006 [65]. They performed their pioneering study by sputtering gold (Au) onto N,N,N-trimethyl-N-propylammonium bis(trifluoromethanesulfonyl)imide and proposed some basic relationships regarding the examined method for the formation of NPs [65]. This presented the start for a lot of research on the sputtering NP fabrication method. The majority of the investigations was conducted with Au and different IL substrates [64, 67–69], but also other materials have been of interest. For Pt [70, 71], silver (Ag) [72] and Pd [73], the formation of NPs in the liquid substrate could be observed as well. When it comes to alloys, the Au-Ag [66], Au-Pt [74], Pt-Cu [59] or Au-Cu [75] systems have been applied (Cu = copper). Different studies tried to reveal which formation mechanism is correct or at least predominating. Apparent evidence for each of the mechanisms shown in Figure 8 as well as mixtures between them can be found in literature and the type of the prevalent mechanism is often connected to viscosity, surface tension and the chemical composition of the surface of the capture medium [57, 59, 67, 68]. The contradicting results could be interpreted as a dependence of the NP formation mechanism on the used materials and experimental conditions [64]. A better understanding of the growth process is highly relevant for a better control of the formed NPs in terms of size and shape. Hence, any results that reveal further information about this question are of great importance.

Sputtering onto liquid substrates fills a niche in the NP formation processes since it combines the advantages of the classical chemical methods with those of the physical processes [57]. By means of chemical approaches, well-defined sizes and shapes of the NPs can be achieved [63]. On the other hand, they mostly require the use of additional stabilization or capping agents, partially produce by-products and are not well-suited to exactly control the material's composition in the case of alloy NPs [57, 63, 75]. The adsorbed surfactant molecules often deteriorate the physicochemical properties, such as the catalytic activity, which is naturally disadvantageous in catalytic applications [62, 76]. Physical methods in contrast enable the preservation of a high purity of the starting material and furthermore provide a great range of processible materials, but exhibit issues with the size control of NPs [57, 63]. In the case of sputtering onto liquid substrates, the sputtering as a physical approach ensures a high quality and good control in terms of chemical composition whereas the nature of the liquid substrate provides for narrow size and shape distributions. This method is thus very promising for a well-regulated fabrication of NPs and is in addition of an environmentally-friendly character [57].

2.3.2 Factors affecting nanoparticle size and morphology

The by far most examined properties of the sputtered NPs are their size and size distribution [57, 60, 64, 67, 69, 75]. A large number of studies addressed the question of how to alter these characteristics of the NPs and several, partially contradicting results were found [57, 60, 64, 67, 69, 75]. Many works determined the discharge voltage or current as a size-governing parameter. Mostly reported is a trend of increasing particle sizes with higher voltages and currents [61, 64, 72, 77]. It is typically argued, that a higher power increases the sputtering emission rate and thereby leads to a higher collision frequency of sputtered species on or in the liquid [77]. However, regarding the discharge voltage, also opposite trends have been observed for different systems [61, 67]. This shows that the effect of those parameters is currently poorly understood.

As a further variable, the substrate temperature has been subject to investigations regarding the NP size. Thereby, the temperature can be raised on purpose, but also by elevated sputtering times or powers. Hatakeyama et al. reported an increased particle size at higher temperatures of the capture medium [60, 69]. They ascribed this effect to elevated temperatures enhancing kinetics and decreasing the viscosity of the surrounding medium. Thereby, diffusion velocities are increased and collisions between the diffusing species become more likely. In this way, larger particles can grow [69]. Other studies predicted smaller particle sizes for lower liquid viscosities. They argued with an increased viscosity leading to a hindered dispersion of the sputtered species into the bulk liquid, which in turn leads to an enhanced particle growth in the proximity of the liquid surface [78]. A similar discussion has been going on for the surface tension of the capture medium. On the one hand, a high surface tension may decrease the diffusion velocities of the sputtered species within the liquid and result in small particles [59]. On the other hand, it could lead to enhanced particle growth at the liquid surface due to a prolonged staying time of the sputtered species at this surface [78]. Wender et al. followed a completely different idea and suggested the particle size is neither dependent on the viscosity nor on the surface tension, but only on the surface composition of the liquid [61, 64].

Finally, the effects of sputtering time and target-to-substrate distance have been investigated. There is consensus on that an increased time and a decreased distance enlarge the nanoparticle concentration in the liquid substrate [59, 62, 64, 65, 67]. Most of the research groups followed Torimoto's et al. initial thesis of an increased sputtered species / NP concentration not influencing the particle size significantly as long as the arrival rate of sputtered species at the surface is unchanged [62, 64, 65]. However, other groups argued that a higher total concentration of the species again results in a higher collision frequency and thereby increases the final NP size [59, 78].

The shape of the sputtered NPs is by far less intensively studied than the size. NPs prepared by sputtering onto liquid substrates are typically spherical [57], even though - especially in the case of alloys - some non-spherical particles can occur as well. Here, the composition of the NPs is a key factor regarding their shape [75]. It is typically adjusted by varying the composition of the targets [74] and measured via X-ray fluorescence spectroscopy (XRF), X-ray diffraction (XRD), energy-dispersive X-ray spectroscopy (EDX) and X-ray photoelectron spectroscopy (XPS) [57, 74, 75].

The present very short review of factors affecting the characteristics of sputtered NPs shows that there is to date little knowledge on how to exactly and consciously control the NPs' properties, especially their size. Varying one variable often simultaneously changes several parameters in the system, which makes it difficult to track the results back to a certain single parameter. This provides strong motivation to shed light on some important correlations regarding this topic.

2.4 Liquid substrates and their properties

Using a suitable substrate is crucial for a successful fabrication of NPs. On the one hand, the liquid needs to stabilize the NPs to prevent an immediate agglomeration. On the other hand, the choice of the liquid can alter the NPs' properties in a similar way as the sputtering parameters [79, 80].

A serious problem to face when handling NPs in a liquid phase is their tendency to agglomerate [81], which typically results in a loss or at least a decrease in the unique properties the NPs exhibit. Agglomeration occurs due to the high surface energy of the NPs caused by their small size [82, 83]. For this reason, stabilization of the NPs in solution is necessary to maintain their individual existence and hence their required properties. Thus, the stabilization function is a very important characteristic a liquid must exhibit to be suitable as a liquid substrate in sputtering to form NPs.

More detailed, the agglomeration behavior of NPs relies on Van-der-Waals dispersion forces. Local fluctuations of the charge distribution in one NP induce equivalent fluctuations in a neighboring one, which leads to attractive forces between different NPs of the same type [84]. To counteract agglomeration of the NPs, oppositely acting, repulsive forces are necessary to overcome or at least decrease the influence of the Van-der-Waals interactions [80]. Chemical reactions or adsorption processes can induce a surface charge of the particles [85], which leads to the formation of an ionic layer around the NPs due to Coulombic attraction. If two particles approach each other, their ionic layers start to overlap at a certain interparticle distance and an electrostatic repulsion force emerges [84, 85]. This so-called electrostatic stabilization effect is illustrated in Figure 9(a) with a cationic layer. Steric effects represent the second important stabilization mechanism for NPs in solution. It is achieved by large molecules - typically polymer chains - adsorbing to the particle surface. Once adsorbed, the molecular chains arrange themselves in a certain, preferred conformation [84, 85]. When two particles approach each other, this conformation is distorted, which results in a repulsion between the particles - this is the steric stabilization as shown in Figure 9(b) [84, 85]. A combination of electrostatic and steric stabilization is possible as well and is termed electrosteric stabilization [80, 86].

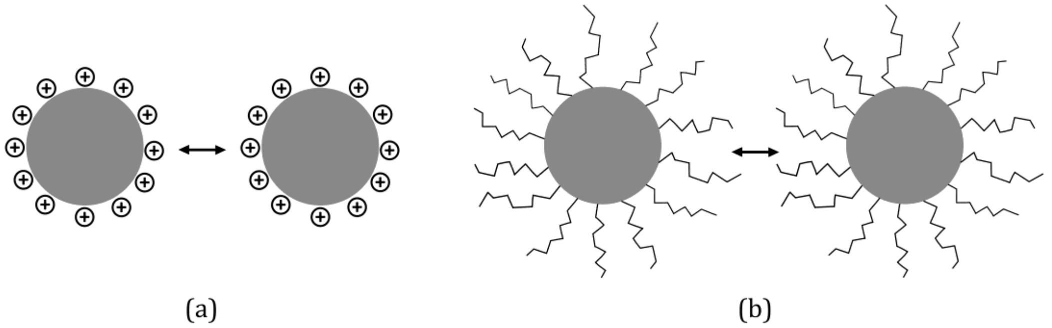

(a) (b)

Figure 9: Nanoparticle stabilization mechanisms: (a) Electrostatic stabilization; (b) Steric stabilization.

Liquid substrates can be chosen to provide at least one of the given stabilization mechanisms. The two different types of liquid substrates used for this thesis research are ionic liquids and polyethylene glycol (PEG), which stabilize the NPs in different ways. The details of these liquids will be presented in the following chapters.

2.4.1 Ionic liquids for nanoparticle stabilization in suspension

Ionic liquids (ILs) are a commonly used liquid substrate for NP fabrication in vacuum [57]. In general, an IL is a liquid substance composed exclusively of ions. ILs exhibit the low vapor pressure required for use in vacuum and are mostly liquid at room temperature due to their large and often asymmetrical molecular geometry [87]. Exemplarily, the chemical structure of a 1-Alkyl-3-methylimidazolium triflate IL is shown in Figure 10.

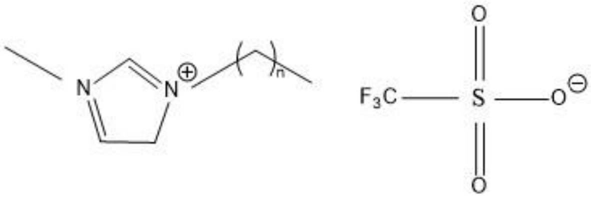

Figure 10: Chemical structure of a 1-Alkyl-3methylimidazolium triflate IL.

Beside the low melting point ILs have further unique properties such as low volatility, high flame-resistance and high potential for recovery after use, which led to ILs being identified as green solvents [76, 79]. Especially outstanding is the high tunability of the IL properties by combining different anions and cations as well as changing certain moieties and chemical groups within the molecules. By doing so, ILs can be 'designed' to perform certain tasks in an optimum way - for example the stabilization of NPs in suspension [79, 88]. ILs offer the possibility to stabilize NPs without the addition of external surfactants, which is why they are very interesting for the fabrication of nanocatalysts [86].

The production of NPs in ILs was performed for the first time by Dshmukh et al. in 2001 [86, 89]. Since then, a lot of research was conducted on the stabilization mechanisms, but they are far from being fully understood [80, 88]. In general, ILs exhibit very ordered (but still dynamic) structures, mainly due to electrostatic interactions between the ions, the formation of hydrogen bonds and Van-der-Waals forces [87, 90]. These liquid network structures act as a kind of template for NPs [90]. ILs provide electrostatic stabilization, however, there is some discussion in literature, whether the anionic or the cationic species of the ILs form the ionic layer directly around the NPs (in Figure 9(a) it is the cationic species) [80, 88]. In fact, this may vary from system to system and could also depend on the size of the NPs [91]. In ILs with rather large molecules (for example with long alkyl chains), a steric stabilization can act additionally. Other, in general less popular stabilization mechanisms for NPs in ILs may play a minor role as well. They are however not important for the general understanding of this work and can therefore be read up on literature as needed [80, 88].

Due to the mentioned tunability of the ILs and the dependence of the stabilization mechanisms on the chemical structure of the liquid, the type of IL can significantly alter the size, size distribution and shape of the formed NPs [79, 80]. Numerous parameters and properties of the ILs such as molecular volumes, coordinating strengths, electrophilicity of the ions as well as viscosity are believed to influence the characteristics of the NPs [80]. A relationship between growing NP size and larger anionic molecular volumes has been reported in literature very often [80]. Also, the alkyl chain length in imidazolium-based cations has been suggested to play a role for the NP size [79, 80]. Plenty of further relationships have been found by individual groups [79, 80, 88]. However, they often contradict each other and do not seem to be universally valid.

Despite all the uncertainties, the vast majority of studies on this topic agrees on the fact that ILs are very suitable to effectively stabilize and control the size of NPs, leading to sufficiently mono-disperse systems for most applications [79, 80].

2.4.2 Liquid polymers for nanoparticle stabilization in suspension

Liquid polymers may cause steric stabilization of NPs in solution by surface adsorption to the NPs [84]. The physical adsorption of polymers to a NP's surface occurs via Van-der-Waals forces, dipole-dipole interactions or hydrogen bonds [92]. Adsorption groups can attach polymers to the NP's surface to increase coverage [93]. Polymers have a large molecular volume, which enables them to effectively separate two particles from each other.

PEG, used for this thesis, stabilizes NPs sterically [93]. Similarly to ILs, PEG exhibits a very low vapor pressure, which decreases with increasing molecular weight [94]. PEG 600 (indicating a molecular weight of 600 g/mol) is liquid at room temperature [60]. The general structure of PEG is illustrated in Figure 11.

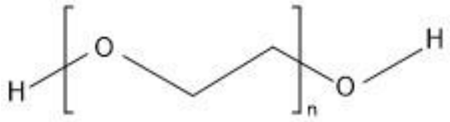

Figure 11: Chemical structure of PEG.

PEG can interact with NPs via Van-der-Waals forces and hydrogen bonds [95, 96]. For metallic NPs, the oxygen atoms of the PEG most likely coordinate directly to the NPs [60]. It has been reported that the stabilizing properties of PEG for metal NPs depend strongly on the type of metal [59], and that Pt and Pt-containing alloy NPs can be stabilized to a satisfactory extent by PEG [59]. An important advantage of PEG compared to ILs is the lower cost of the polymer, which makes the use of generated NPs in a large scale more profitable [60]. On the other hand, PEG may not be able to stabilize NPs as effectively and long-termed as ILs due to the absence of an electrostatic effect [60].

3 Methods

This chapter contains information on all the experimental methods applied during this work. Firstly, the materials used will be described along with experimental procedures, then the fundamentals of the exerted analysis methods are explained as far as necessary for the understanding of the subsequent analysis.

3.1 Material overview

The Pt and Pt_3Y sputtering targets represented the base materials for this study. They were both purchased from Goodfellow with a purity of 99.99%, a thickness of (1.5 ± 0.1) mm and a diameter of (38.1 ± 0.5) mm.

Different liquid media were applied as substrates for the sputtering process. They were all stored under nitrogen atmosphere and used during sputtering without any additional purification / treatment. Table 2 provides an overview of the liquid substrates.

Table 2: Overview of used liquid substrate materials.

Liquid	**Abbreviation**	**Manufacturer**	**Purity**
1-Ethyl-3-methylimidazolium triflate	[Emim] [OTf]	Iolitec Ionic Liquids Technologies GmbH	99.0%
1-Ethyl-3-methylimidazolium bis(fluoromethylsulfonyl)imide	[Emim] [Tf_2N]	Iolitec Ionic Liquids Technologies GmbH	99.5%
1-Ethyl-3-methylimidazolium tris(pentafluoroethyl)-trifluoro-phosphate	[Emim] [FAP]	Merck Chemicals GmbH	99.0%
1-Butyl-3-methylimidazolium bis(fluoromethylsulfonyl)imide	[Bmim] [Tf_2N]	Iolitec Ionic Liquids Technologies GmbH	99.5%
1-Decyl-3-methylimidazolium triflate	[Dmim] [OTf]	Iolitec Ionic Liquids Technologies GmbH	99.0%
1-Decyl-3-methylimidazolium bis(fluoromethylsulfonyl)imide	[Dmim] [Tf_2N]	Iolitec Ionic Liquids Technologies GmbH	98.0%
Polyethylene glycol 600	PEG 600	Alfa Aesar by Thermo Fisher Scientific	95.0%

For cleaning, washing and sample preparation purposes, several further liquids were applied. Their basic specifications are listed in Table 3.

Table 3: Overview of used process liquids.

Liquid	Abbreviation	Manufacturer	Purity
Acetone	-	VWR International	99.5%
Acetonitrile	-	Sigma-Aldrich, Inc.	99.5%
Ethanol	EtOH	Solveco	99.7%
2-Propanol	IPA	VWR International	99.7%
Ultrapure water	-	Merck KGaA	Type 1

In the case of ultrapure water, Merck KGaA is the manufacturer of the Synergy UV water purification system. The purified water is commonly termed Milli-Q.

3.2 Sputtering procedure for nanoparticle and thin film preparation

The instrument used for the fabrication of all samples was a custom-made sputter coater. The process chamber was pumped by an Edwards nXDS10i scroll pump and a Pfeiffer TMU 521 P Turbomolecular drag pump. Sputtering was performed with a base pressure between $1.3 \cdot 10^{-7}$ and $9.2 \cdot 10^{-7}$ mbar. For thin films, small pieces of pure Si-wafers were used. To hold the liquid substrates, wafers with a diameter of 1 inch were used - namely either Si-wafers (UniversityWafer Inc.) or fused silica wafers (Mark Optics Inc.).

Before being inserted into the sputtering chamber, each wafer was ultrasonic cleaned in acetone, ultrapure water and IPA for 15 minutes in each using an Elmasonic P 60 H ultrasonic cleaner at 37 kHz. Afterwards, the wafer was dried with nitrogen and placed into a stainless-steel petri dish with a diameter of 7.5 cm (Bochem Instrumente GmbH). For sputtering onto a liquid substrate, 200 µl of the liquid was dropped on the wafer. The dish was subsequently inserted into the sputtering chamber and centered below the target. After adjusting the target-to-substrate distance to the desired value, the sputter chamber was closed and pumped. To provide for sufficient vacuum and remove as much water from the liquid substrate as possible, pumping was conducted for at least 24 hours. For the actual sputtering step, an Ar-flow of 300 sccm was regulated by a mass flow controller and the power was delivered to the cathode by an MDX 1K Magnetron Drive (Advanced Energy Industries, Inc). Sputtering was performed with power regulation mode; the voltage and current were automatically adapted by the power supply. Before opening the shutter, pre-sputtering was applied for 5 minutes to clean the target. Sputtering was performed for a well-defined time span by opening and closing the shutter. For samples fabricated with a sputtering time of 15 minutes, sputtering was performed in three discrete intervals of 5 minutes to prevent excessive heating of the substrate during the process. The interruptions between the different cycles lasted 20 minutes to allow for cooling of the liquid. This sputtering time is referred to as t = 3 x 300 s in the course of this work.

The Ar-pressure during sputtering varied between $6.6 \cdot 10^{-3}$ mbar and $7.2 \cdot 10^{-3}$ mbar for the different samples. An overview of all samples and sputtering parameters can be found in Appendix A.

After sputtering, the liquid samples were collected from the wafers and stored in Eppendorf tubes. Batches that were subject to a post heat-treatment or an ink-preparation procedure were kept in lockable glass vials.

The concentration of sputtered species in the liquid substrates can be approximated using existing calibration measurements. At a power of P = 50 W and a target-to-substrate distance of W_d = 8 cm (parameters used for the most promising batches in this thesis), the sputtering growth rates v_s of Pt and Pt_3Y thin films are:

$$v_{\mathrm{s,Pt}} = (0.33 \pm 0.05)\ \frac{\mathrm{nm}}{\mathrm{s}}$$
$$v_{\mathrm{s,Pt_3Y}} = (0.46 \pm 0.07)\ \frac{\mathrm{nm}}{\mathrm{s}}$$

Based on these values, an estimation of the concentration can be made, knowing the sputtering time t as well as the volume of the liquid substrate V_l. During this study, the best results were achieved for $t = 3 \text{ x } 300 \text{ s} = (900 \pm 5)$ s and $V_\mathrm{l} = (200 \pm 10)$ µl. The sputtered concentration per volume of the liquid substrate c_s can be calculated according to equation (3.1), where m_s is the sputtered mass onto the liquid substrate, ρ_s the density of the sputtered material, V_s the sputtered volume onto the liquid substrate, A_w the area of the wafer, d_s the sputtered thickness and D_w the diameter of the wafer (1 inch).

$$c_\mathrm{s} = \frac{m_\mathrm{s}}{V_\mathrm{l}} = \frac{\rho_\mathrm{s} \cdot V_\mathrm{s}}{V_\mathrm{l}} = \frac{\rho_\mathrm{s} \cdot A_\mathrm{w} \cdot d_\mathrm{s}}{V_\mathrm{l}} = \frac{\rho_\mathrm{s} \cdot \pi \cdot \left(\frac{D_\mathrm{w}}{2}\right)^2 \cdot v_\mathrm{s} \cdot t}{V_\mathrm{l}} = \frac{\rho_\mathrm{s} \cdot \pi \cdot {D_\mathrm{w}}^2 \cdot v_\mathrm{s} \cdot t}{4 \cdot V_\mathrm{l}} \tag{3.1}$$

The densities of Pt and Pt_3Y are

$$\rho_\mathrm{Pt} = 21.50\ \frac{\mathrm{g}}{\mathrm{cm}^3}\ [97]$$
$$\rho_{\mathrm{Pt_3}Y} = 16.62 \frac{\mathrm{g}}{\mathrm{cm}^3}\ [98].$$

The particle concentrations per volume of liquid substrate are calculated for Pt and Pt_3Y using equation (3.1):

$$c_\mathrm{s,Pt} = (16.18 \pm 2.59)\ \frac{\mathrm{\mu g}}{\mathrm{\mu l}}$$
$$c_\mathrm{s,Pt_3Y} = (17.43 \pm 2.80)\ \frac{\mathrm{\mu g}}{\mathrm{\mu l}}$$

It needs to be stated explicitly that this is the concentration related to the volume of the *initially* used liquid (the volume of the sputtered species is not considered in the calculation). Therefore, the given values should be regarded as an approximation.

3.3 Post heat-treatment

Some of the samples were heat-treated immediately after the sputtering process. A glass vial was flushed with nitrogen, filled with the sample and flushed with nitrogen once more before the lid was closed in order to ensure a complete nitrogen atmosphere within the vial. The vial was subsequently placed in a silicon oil bath at room temperature. The bath was heated up to 165 °C by a hot plate and the temperature was controlled by a thermocouple. As soon as the temperature reached 165 °C, the sample was kept in the oil bath for 1 more hour.

3.4 Preparation of carbon supported nanoparticles

For an electrochemical characterization of the ORR activity of the NPs, they needed to be immobilized on a glassy carbon electrode (GCE). For this purpose, a catalyst ink was produced. All the glassware and tools used during the ink preparation were ultrasonic cleaned in IPA and dried in an oven at 80 °C beforehand. 2.8 mg of Vulcan XC-72 carbon black was ground manually with a spatula, before 75 µl of the sputtered PEG+NPs was added. The carbon powder was dispersed in the liquid by sonicating the mixture at 37 kHz for 30 minutes below 40 °C by the use of an ice bath. Subsequently, the mixture was heated in an oil bath at 150 °C under constant stirring by a magnetic stirring bar for 5 hours to allow for the adsorption of the NPs to the carbon particles. After finishing this treatment, 500 µl IPA was added and mixed using a vortex mixer. A wet powder was then isolated by transferring the mixture to an Eppendorf tube, centrifuging at a relative centrifugal force (RCF) of 2600 for 5 minutes and removing the liquid supernatant. After drying in air for several minutes, 1.0 mg of the solid was weighed in a glass vial and ground again manually with a spatula. A 2 wt% Nafion solution was prepared by mixing 483 µl of a Nafion D-521 dispersion (Afla Aesar) (5 wt% Nafion dispersion in water and 1-Propanol) with 1400 µl IPA. 500 µl of this Nafion solution was added to the catalyst powder and the mixture was dispersed by sonication at 37 kHz below 40 °C by the use of an ice bath for 1 hour. Finally, a GCE was ultrasonic cleaned in acetone, ultrapure water and IPA for 15 minutes each and dried in an oven at 80 °C. 15 µl of the prepared ink was dropped on the GCE and dried in air in a petri dish with closed lid for 1 hour. Parts of the ink preparation procedure were adopted from previously reported methods [99, 100].

3.5 Centrifugation for nanoparticle extraction

In the course of a pre-study (chapter 4.1.1), the NPs were tried to be extracted via centrifugation in a Mikro 22 R centrifuge by Hettich Zentrifugen. 150 µl of the pure sample was mixed with 600 µl EtOH and the mixture was inserted into a 1153 rotor (Hettich Zentrifugen). The centrifugation speed was set at the maximum possible speed of 14000 rpm, which corresponded to an RCF of 20600. After centrifugation for t = 120 min, the mixture was examined for possible sedimentation by eye.

3.6 Analysis methods and data treatment

This subchapter is dedicated to the analysis methods applied in the study to characterize materials, thin films and NPs used or fabricated during the experiments. Hereby, the preparation of the samples from the initial as-sputtered particles as well as the basic principles of the analysis methods are elucidated. Furthermore, information on the treatment of the received data is given if necessary.

3.6.1 Raman spectroscopy

In order to test the quality of liquid substrates used for the sputtering process, Raman spectroscopy was applied. Therefore, 10 µl of the liquid was dropped on a glass plate, which was subsequently inserted into a WITec alpha300 R Raman microscope. For the identification of a suitable measurement position, an objective with a magnification of 10x was used and the instrument was focused on a position within the liquid sample drop. The sample was then irradiated with a laser of a wavelength of 532 nm and a power of 75 mW at the laser output.

In Raman spectroscopy, the electromagnetic waves interact with the molecules of the sample and a small portion of the photons is inelastically scattered. Thereby, a photon can excite particular vibration modes of the sample molecules if its energy is sufficient. The energy of the photon E_{ph} can be written as [101]

$$E_{\mathrm{ph}} = \mathrm{h} \cdot \tilde{\nu} \cdot \mathrm{c} \tag{3.2}$$

with Planck's constant h, wavenumber $\tilde{\nu}$ and speed of light c. When exciting a molecular vibration, the energy of the photon is reduced by the difference between the initial and the excited energetic state of the molecule. According to equation (3.2), the change in the photon energy also changes its wavenumber. This effect is known as Raman scattering and the deviation from the initial and the scattered wavenumber is called Raman shift [101, 102].

The scattered light is focused by an optical system and guided to a grating monochromator [103]. The intensity of the scattered light can thereby be measured by a detector as a function of the wavelength (i.e., the Raman shift). To construct a Raman spectrum, the intensity is typically plotted against the Raman shift. Since molecules or certain moieties of molecules exhibit distinct vibrational states, the Raman shifts are characteristic for certain species and provide so-called fingerprints of the present substance [101, 102, 104].

In the Raman spectroscopy experiments performed in this study, Raman shifts between 250 and 3500 cm^{-1} were recorded. To generate a spectrum, 10 accumulations with an integration time of 1 s were collected. Control of the instrument and data acquisition was accomplished via the Control FIVE 5.0 software (WITec).

3.6.2 Transmission electron microscopy

Transmission electron microscopy (TEM) was used to image the particles. In contrast to other methods applied in this thesis, it allowed for a direct observation of species and did not rely on complex data treatment. The images prepared by TEM were analyzed for an estimation of the sizes and size distributions of the fabricated particles.

To enable the imaging of the particles, these needed to be isolated from the liquid they were dispersed in. Removal of IL was particularly important as remaining IL molecules interacted with the electron beam within the microscope due to their ionic character and thus made imaging impossible. Therefore, a well-defined preparation procedure for the TEM samples was applied. To visualize the small particles, TEM grids with an ultrathin carbon film (less than 3 nm) on a holey carbon support film were used (TED PELLA, INC.). For preparation, a grid was held with crossed tweezers and 4 µl of the sputtered liquid substrate was dropped onto the carbon-coated side. The grid was then left for the adsorption of particles for at least 4 hours. Subsequently, the tweezers with the grid were attached to a slightly inclined platform with the carbon-coated side facing down. Using a syringe, the grid was washed dropwise with pure acetonitrile. Hereby, as many drops were dripped on the grid until 3 drops fell off the carbon-coated side. This was repeated every three minutes for one hour in total. To remove liquid accumulating in between the tweezer arms due to capillary forces, the space between the arms was cleaned with acetonitrile after 15 minutes and 30 minutes. After finishing this washing procedure, the grid was dried gently in a nitrogen stream for 10 minutes. The setup for the TEM grid preparation is illustrated in Figure 12.

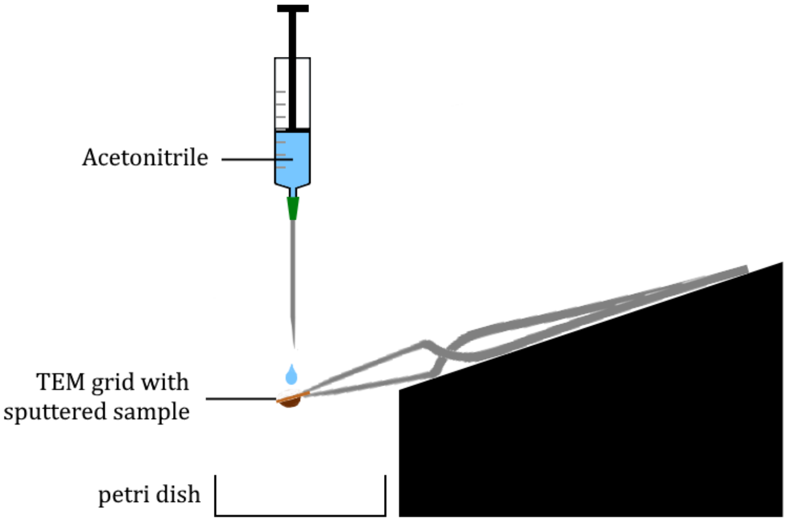

Figure 12: Illustration of the TEM grid preparation procedure.

For imaging, a FEI Tecnai T20 microscope equipped with a LaB_6 filament cathode came into operation and an acceleration voltage of 200 kV was used. Since only brightfield imaging was applied in this study, this setup is explained briefly in the following.

In general, the electrons extracted from an electron source are focused using a set of lenses, interact with the sample and finally impinge on a phosphorescent screen or a CCD camera forming an image. In the brightfield mode, only electrons passing the sample without changing their direction can contribute to the image. This allows for diffraction contrast as well as mass thickness contrast. The latter is likely to predominate for the NPs investigated in this study and relies on electrons going off axis by incoherent elastic scattering during interaction with the sample. Also, the Z-value of the material plays a role for the probability of a scattering event. However, since TEM is not used to distinguish between different phases in this work, this is not further explained here. [105]

As mentioned before, TEM images were used to construct size distributions of the NPs. Therefore, at least 5 images recorded on different areas on the grid and a minimum of 175 particles per sample in total were examined. Analysis was performed with the 'ParticleSizer' ImageJ plugin by Thorsten Wagner. To achieve the best analysis results, contrast and brightness were optimized for every image initially. The minimal ferret diameter was set to a pixel-value corresponding to 0.7 nm in order not to detect small-sized noise as particles. The particle shape was not restricted to spherical or elliptical forms, even though most of the particles exhibited at least a near-spherical shape. Subsequently, the minimum object-to-background intensity difference (threshold value) as well as the smoothing factor were adjusted individually for each image to optimize the recognition of the particles. For most of the images, some particles recognized by the software had to be sorted out manually to prevent incorrect analysis. In order to generate a size distribution as reliable as possible, the threshold value was typically set to slightly larger values than required. In this way, only particles with a good contrast were identified. An example of the particle analysis is shown in Figure 13, where the red marked areas are recognized as NPs.

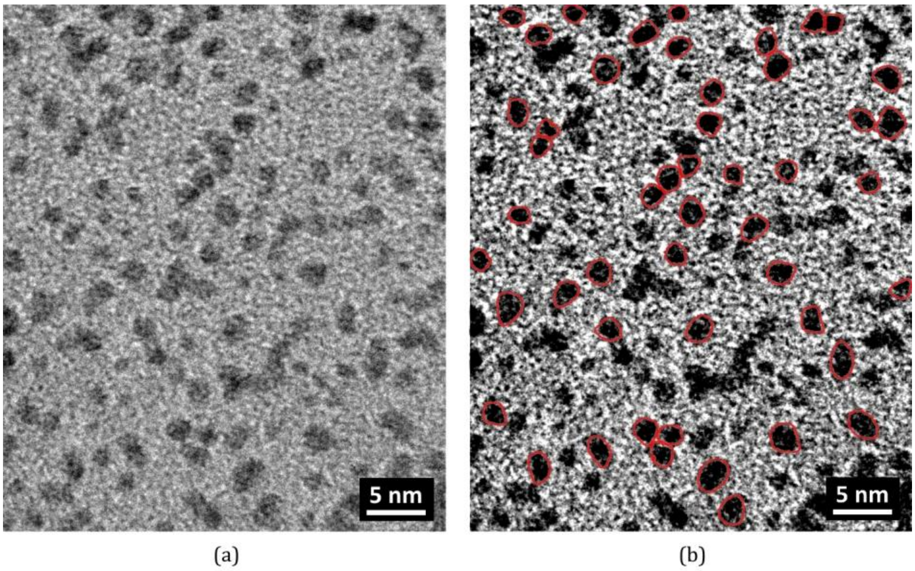

Figure 13: Particle size analysis from a TEM image via ImageJ: (a) Original image; (b) Analyzed image (red: recognized particles).

Despite the described procedure, it was at least challenging to determine the size of the small NPs correctly due to strong noise, overlapping particles or poor contrast. This made the correct recognition of individual particle edges not trivial. The determined sizes and size distributions can thus be regarded as an approximation of the real conditions, but it should be kept in mind that they are afflicted with certain errors due to the described analysis method.

During TEM investigations, EDX was used to study the chemical composition of the particles. This was done using an EDAX X-ray system attached to the FEI Tecnai T20. Only the thin films used for the pre-investigation of the Pt_3Y target (chapter 4.1.2) were investigated with a silicon drift detector the Zeiss Supra 60 VP scanning electron microscope was equipped with.

In EDX, sample atoms can be ionized by the liberation of core level electrons due to inelastic collisions with beam electrons. After a certain time, a generated 'hole' in the electron shell can be occupied by an electron of the same atom from a higher energy level. Thereby, an X-ray with a wavelength λ is emitted, which is determined by the energy difference ΔE between the two electronic states. This is represented in equation (3.3), where h is the Planck's constant and c is the speed of light [106].

$$\Delta E = \mathrm{h} \cdot \frac{\mathrm{c}}{\lambda} \tag{3.3}$$

Because the electronic energy levels are characteristic of the chemical element, the wavelength (i.e., the energy) of the X-rays provides information on the chemical composition of the sample. For a quantitative analysis, the areas under the peaks are considered. Therefore, the peaks are fitted and the areas are weighed with sensitivity factors specific for the individual elements. The depth of information lies in the range of 1 – 5 µm for EDX. [104, 107]

In this study, the TEM Imaging & Analysis software (TIA) version 4.15 SP1 by FEI was used for analysis of the EDX data. A quantification example performed by the software is given in Appendix B.

3.6.3 Scanning electron microscopy

Scanning electron microscopy (SEM) was the second direct imaging technique applied in this work. The used microscope was a Zeiss Supra 60 VP model which employed a Schottky field emission electron source. The electrons were accelerated towards the sample by an acceleration voltage of 5 kV.

Compared to TEM, SEM was used less frequently and only for monitoring the dried catalyst inks. The method is described very briefly in the following.

When impinging on the sample, the beam electrons can be backscattered and generate secondary electrons by ionization of sample atoms by inelastic collisions. Both secondary and backscattered electrons are registered by a detector. Depending on the angular relations between the local sample surface, the primary electron beam and the detector axis, the number of electrons reaching the detector can be smaller or larger - a topographic contrast is the consequence. Furthermore, shadowing effects and different backscattering coefficients for different materials can cause additional contrast. During imaging, the primary electron beam successively scans the whole image area and the strength of the signal is transferred to a corresponding brightness in the image. [108]

In this study, an In-Lens detector was used for imaging, which is why secondary electrons contributed to the signal in the first place [108].

3.6.4 Small angle X-ray scattering

Beside direct imaging via TEM, small angle X-ray scattering (SAXS) was an important technique used in this work to determine the size of the fabricated particles. It was a very viable method since it could be performed directly on the liquid phase.

The SAXS measurements were performed in a Mat:Nordic system by SAXSLAB. The instrument used a Rigaku 003+ Cu-radiation source producing monochromatic X-rays with a wavelength of 0.154 nm and a Decris Pilatus 300K detector. All measurements were conducted at roughly 0.1 mbar. To prepare a sample, the liquid was syringed into a glass capillary with an outer diameter of 1.0 mm and a wall thickness of 0.01 mm (Hilgenberg), without including any air bubbles. After sealing the capillary with hot glue, it was mounted onto the Ambient Capillary Plate sample holder. To exactly determine the sample to detector distance, a calibration was performed prior to each measurement with silver behenate. Two different q-ranges were used for this thesis. In SAXS, the sample to detector distance was about 1078 mm, which led to a measurable q-range of up to 0.25 $Å^{-1}$. When applying medium angle X-ray scattering (MAXS), the q-range was expanded up to 0.7 $Å^{-1}$ at a sample to detector distance of 478 mm. The coverage of larger q-values allowed for a better investigation of very small particles compared to SAXS [109]. The beam size was 0.3 mm in SAXS and 0.4 mm in MAXS experiments.

One major process taking place when the X-rays penetrate the sample is absorption [110]. This decreases the intensities, which is why solvents with low absorption coefficients should normally be used. If this is not possible, a long measurement time can be applied instead. The SAXS method relies on Rayleigh and Thomson scattering [110]. Hereby, an irradiating X-ray photon makes the electrons of a sample atom vibrate at a certain frequency connected to the wavelength λ of the photon. Consequently, the electrons themselves emit radiation of the same wavelength, but in all directions [110]. Due to their coherence, the waves emitted from different atoms can interfere with each other. Depending on the scattering angle, the interference can be constructive or destructive as the limiting cases. In this way, all the atoms within one particle generate a two-dimensional interference pattern on the detector screen. The characteristics of this pattern depend on the size and shape of the particle, which is why it carries information about these properties [110]. This part of the scattered intensity is therefore called the form factor [110]. The angle 2θ (compare Figure 14) is typically expressed in terms of the q-value - the length of the scattering vector which is defined as [110]

$$q = \frac{4 \cdot \pi}{\lambda} \cdot \sin(\theta) \tag{3.4}$$

The SAXS setup is schematically shown in Figure 14.

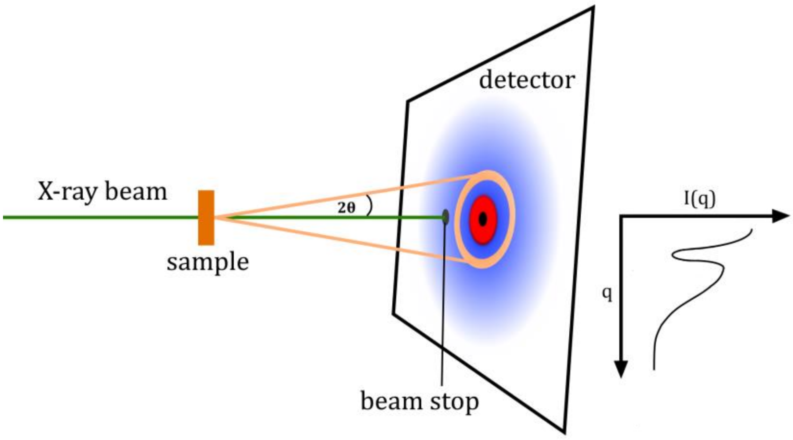

Figure 14: Schematic setup of a SAXS experiment.

Unfortunately, the atoms of the solvent surrounding the particles scatter the X-rays as well and thus contribute to the interference pattern. To nullify their contribution, a second sample consisting only of the pure solvent needs to be measured. The scattered intensity of this reference I_{solvent} can then be subtracted from the sample intensity I_{sample} for every q-value. However, the absorption behavior of the particles may be different than the one of the solvent, which is why the sample intensity must be corrected for differences in the transmission of sample (T_{sample}) and reference (T_{solvent}). The corrected intensity values I_{c} can consequently be calculated using equation (3.5) [110].

$$I_{\mathrm{c}} = I_{\mathrm{sample}} \cdot \frac{T_{\mathrm{solvent}}}{T_{\mathrm{sample}}} - I_{\mathrm{solvent}} \tag{3.5}$$

In a real SAXS measurement, many particles are irradiated by the beam and contribute to the signal. The measurement is hence an average of all particles within the beam [110]. If the particles are diluted enough, the form factors of all single particles can be simply summed to obtain the total form factor $P(q)$ and the final scattered intensity [110].

For solutions with a high concentration of particles, the photons scattered from different particles may interfere with each other and the summed-up form factor cannot describe the intensity recorded by the detector on its own anymore. A structure factor $\mathrm{S}(q)$ taking into account the interparticle interferences has to be included in the observed intensity $I(q)$ [109, 110]:

$$I(q) = P(q) \cdot S(q) \tag{3.6}$$

In this study, the raw intensity data was extracted from the two-dimensional detector image by the software saxsgui v2.23.32 (JJ X-Ray Systems ApS). The basic data treatment applied to the generated SAXS data included background subtraction as well as correction for the particle absorption according to equation (3.5). In order to determine the particle size from the scattering curve, the data was fitted with SasView-5.0.1 and a spherical form factor was used. The model for the signal intensity is presented in equation (3.7), where f_p is the volume fraction of the particles, V_p the volume of one particle, $\Delta\rho$ the difference of the scattering length densities of the particle and solvent material, r the particle radius and B the background [111].

$$I(q) = \frac{f_\mathrm{p}}{V_\mathrm{p}} \cdot \left[3 \cdot V_\mathrm{p} \cdot \Delta\rho \cdot \frac{\sin(q \cdot r) - q \cdot r \cdot \cos(q \cdot r)}{(q \cdot r)^3}\right]^2 + B \qquad (3.7)$$

Scale (i.e., f_p), background and radius were set as variables. The scattering length densities of the particle and solvent substances were calculated using the SLD calculator tool. For most of the measurements, no structure factor was needed to satisfactorily fit the intensity profiles.

If required, the hayter_msa structure factor was applied. Here, scale, background, radius, volume fraction, charge, concentration and dielectric constant were set as variables.

The data used for fitting was restricted to a q-interval with reasonable statistical errors. During fitting, the software weighed the individual datapoints according to their uncertainties in the intensity (increased emphasis on datapoints with small uncertainties).

3.6.5 Dynamic light scattering

Dynamic light scattering (DLS) was applied to measure the particle size for comparison to SAXS and TEM. The ZEN 3600 model (Zetasizer Nano ZS) of Malvern Instruments with a 623.8 nm He-Ne-Laser monochromatic light source was used to determine the particle size directly in solution. The detector was placed at an angle of 175° relative to the incident beam. Analysis was performed via the Zetasizer Software Version 7.10 (Malvern Instruments). To conduct a measurement, the sample was filled into a high precision cuvette made of Quartz with a light path of 10x10 mm (Hellma Analytics; Type 111-QS), which was subsequently inserted into the measurement system. The cuvettes were cleaned with IPA from the inside and outside prior to use. The refractive index and viscosity of the solvent were supplied as input parameters to the software in order to allow for the calculation of number particle size distributions.

Upon irradiation of the sample with monochromatic light, photons are scattered in all directions at the dispersed NPs. The waves, scattered at different particles, interfere with each other and thereby generate a certain intensity measured by a detector. The particle size can be correlated with the change of the intensity over time induced by Brownian motion of the particles. This is characterized by an autocorrelation function. The larger the particles, the slower their movement and the slower the decay of the autocorrelation function. In the case of a polydisperse sample, the autocorrelation function is a superposition of multiple exponentially decaying functions, which are weighed according to the size distribution of the particles. The final function is fitted by the software to determine the particle size distribution. [112, 113]

3.6.6 UV-Vis spectroscopy

Ultraviolet-Visible (UV-Vis) spectroscopy was applied mainly for the comparison of particle concentrations between different solutions and for qualitative conclusions on particle sizes. In order to generate a spectrum, a reference sample consisting of the pure solvent was measured first, before the sample containing the NPs itself was inserted into the system. The measurements were performed in a Cary 60 spectrometer of Agilent Technologies. The liquid substance was inserted into a high precision cuvette made of Quartz with a light path of 10x4 mm (Hellma Analytics; Type 114F). The cuvettes were cleaned with IPA from the inside and outside prior to use. During the experiment, monochromatic light was generated from a continuous light spectrum from a Xenon pulse lamp [103].

The energy E_{ph} of the monochromatic light passing through the sample is connected to its wavelength λ via the Planck's constant h and the speed of light c [114]:

$$E_{\mathrm{ph}} = \mathrm{h} \cdot \frac{\mathrm{c}}{\lambda} \tag{3.8}$$

Whatever chemical species are present in the sample, they can possess different discrete electronic, vibrational and rotational energy states. If the energy of a photon given by equation (3.8) corresponds to the energetic difference between two of those energy levels, the photon can induce a change from the energetically lower to the higher state and is thereby absorbed [103]. In this way, the intensity of the light of this specific wavelength passing through the sample is reduced [103]. To quantitatively describe this effect, the absorbance A is defined as [115]

$$A = \log\left(\frac{I_0}{I}\right) \tag{3.9}$$

with the initial intensity I_0 and the attenuated intensity I. For a specified sample, the absorbance can be calculated by the Bouguer-Lambert-Beer law given in equation (3.10) [115], using the concentration of the absorbing species c, its extinction coefficient ε and the length of the optical path through the sample l.

$$A = \varepsilon \cdot c \cdot l \tag{3.10}$$

By measuring the absorbance for a continuous wavelength range, an absorbance spectrum is obtained.

In the experiments performed during this work, a scan rate of 300 nm/min was applied in the range of 190 – 800 nm. The final data was calculated automatically by the Cary WinUV Scan Application (Agilent Technologies) by subtracting the reference baseline (spectrum of the solvent) from the sample absorbance. By doing so, only the absorbance originating from the dispersed species is illustrated in the final spectrum. Since the available energy states are characteristic for the present species, this spectrum can provide information on the nature of the sample.

3.6.7 X-ray photoelectron spectroscopy

For the samples prepared by sputtering of the Pt_3Y target, XPS was applied on the one hand to determine the surface chemical composition and on the other hand to investigate the chemical state of the elements of interest. Therefore, a Perkin Elmer PHI 5000 C ASCA system with a monochromatic Al Kα X-ray source came into use. The concentric hemispherical analyzer was oriented at an angle of 45° corresponding to the sample normal.

When the generated X-rays penetrate a sample surface, they interact with the atoms of the sample. An inelastic collision can liberate a core level electron from a sample atom [104]. In case the X-ray energy exceeds the binding energy E_B, the excess energy is transferred to kinetic energy of the electron E_kin. Therefore, the kinetic energy relates to the binding energy via equation (3.11), where h is the Planck's constant, ν is the frequency of the primary X-ray and ϕ is a work function term, which is very small compared to the other quantities in the equation [104].

$$E_\mathrm{kin} = \mathrm{h} \cdot \nu - E_\mathrm{B} - \phi \tag{3.11}$$

This kinetic energy is the quantity being measured by an electron analyzer. Every chemical element has specific binding energies for the core level electrons knocked out, which allows for a chemical analysis of the sample. Quantitative investigations are performed by comparison of the areas under the peaks and application of sensitivity factors.

A main advantage of XPS is the capability to determine chemical bonding states of the atoms at the surface. Bonding to other elements shifts the charge density of the valence electrons and as a consequence the potential of the core level electrons is altered [104, 116]. This enables the determination of chemical states of the elements by a precise analysis of the peak positions.

An important practical aspect of XPS is the depth of information. Owing to a small mean free path of the generated photoelectrons in the sample, the typical information depth is only roughly 10 nm for common XPS primary energies [104, 107]. This makes XPS an extremely surface sensitive analysis technique.

In this work, a survey spectrum by scanning the whole binding energy range of 0 – 1200 eV was taken first to identify which elements were present. Then, longer scans of each element were taken repeatedly to get a better resolution.

For the analysis, the complete spectrum was shifted to a characteristic peak of known binding energy (either the C peak corresponding to the C-C bond (284.8 eV [117]) or the metallic Pt peak (71.2 eV [118])) using the MultiPak V6.0A software (Physical Electronics, Inc.). Fitting of the peaks was then performed in the software XPSPEAK 4.1. A Shirley background was chosen to model the intensity differences at both sides of the peak.

For the Pt4f doublets, the spin-orbit-splitting (peak separation) was set to 3.33 eV [118], the Lorentzian-Gaussian ratio to 40% and the peak asymmetry value to 0.19 [40]. The peak position was constrained to (71.2 ± 0.2) eV for the metallic Pt peak ($Pt4f_{7/2}$) [118]. For the oxide, the exact peak position is less clear and different values can be found in literature [118, 119]. For this reason, the position was allowed to vary between 72.4 eV and 75.6 eV [119]. The full width at half maximum (FWHM) of the oxide peak was set equal to the value for the metallic peak.

The Y3d peaks were characterized by a spin-orbit-splitting of 2.1 eV [120]. For the metallic form, the peak position was set to (156.0 ± 0.2) eV ($Y3d_{5/2}$) [118]. The reported values for the oxide peak are again less consistent. The position was restrained to energies between 156.7 eV and 158.6 eV [118, 119]. The FWHM as well as the Lorentzian-Gaussian ratio of the oxide peak were set equal to the values for the metallic peak.

3.6.8 X-ray fluorescence spectroscopy

XRF was the third method applied for compositional analysis in this work and was used for the elemental concentration investigation directly in the liquid phase.

For the measurement, the liquid sample was dropped on a 12 µm thick polypropylene foil inside a plastic cup and loaded into the Axios XRF spectrometer (Malvern-Panalytical). A helium atmosphere was supplied and an X-ray tube with a rhodium anode served as the X-ray source.

The XRF technique can be regarded as a combination of XPS and EDX. The emitted X-rays irradiate the sample and interact with the present atoms. Like in XPS, the X-rays liberate electrons from the sample atoms and are thereby absorbed. The generation of a photoelectron leaves a 'hole' in the electron shell of the atom, which is filled by another electron of the same atom from a higher energy level. From here, the occurring processes are the same as in EDX. An X-ray of a characteristic wavelength (compare equation (3.3)) is emitted by an electron transition with a certain probability and this wavelength provides information about the emitting element. The quantitative analysis in XRF is carried out in the same way as in EDX. With the help of sensitivity factors, the area under the peaks can be transferred to the concentrations of the elements. [104, 106]

Here, solid standard samples had been used for calibration (i.e., for the determination of the sensitivity factors).

3.6.9 Electrochemical characterization

For an electrochemical characterization of the fabricated NPs, a three-electrode setup with a modulated speed electrode rotator AFMSRCE (Pine Research Instrumentation) was employed. The system was controlled by a BioLogic SP-300 potentiostat. Prior to a measurement, the whole cell was cleaned with Piranha solution overnight (3 parts H_2SO_4; 1 part H_2O_2) and rinsed with ultrapure water 10 times. After flushing the cell with Ar, it was filled with 120 ml of the 0.1 M $HClO_4$ electrolyte. A Pt wire served as the counter electrode and was cleaned by flame annealing for ~30 seconds. The $Hg/HgSO_4$ reference electrode was extensively rinsed with ultrapure water before use. The rotator was flushed with nitrogen (N_2) before and after equipping it with the coated GCE acting as the working electrode.

In CV and RDE investigations, the electrical current flowing between the working and the reference electrode is measured in dependence of the working electrode potential. A very common reference electrode is the reversible hydrogen electrode (RHE). The three-electrode setup is completed by the counter electrode, which has the purpose to run the second half-reaction and close the electrical circuit to allow a current to flow. In contrast to CV, the working electrode is rotated at a certain speed in an RDE measurement in order to achieve a sufficient and well-defined constant flow of reactants to the working electrode surface. In this way, results of different experiments can be better compared. However, the extracted curves and parameters depend on experimental parameters like rotation speed and scan rate, which is why it is indispensable to always report these quantities. [9, 28, 121, 122]

To record a cyclic voltammogram, the electrolyte was bubbled with Ar to remove dissolved oxygen. The samples were conditioned by cycling between -0.6 V and 0.3 V against the Hg/$HgSO_4$ reference electrode at 20 mV/s for 50 times, before the actual measurement was performed in a defined potential range. For the subsequent measurement of an ORR polarization curve, the electrolyte was saturated with oxygen by bubbling for 15 minutes prior to the measurement.

In CV as well as RDE measurements, the electrolyte solution itself has a certain resistance, which needs to be corrected to obtain only the potential difference between the working electrode and the reference electrode. Here, this solution resistance was determined by impedance measurements at frequencies of 10 Hz and 20 kHz for both the Ar and O_2 saturated electrolyte.

4 Results and Discussion

4.1 Pre-investigations

In order to test the available equipment for sputtering and verify the suitability of the system as well as the materials used in this study, some pre-investigations were performed.

4.1.1 Sputtering of platinum

Platinum was used for a pre-study as it is the base material for this thesis. It acts as a good control of the sputtering setup and is furthermore the base metal for the alloy. [Bmim] [Tf_2N] was chosen as the substrate liquid as it has been used extensively in literature [64, 75]. Compared to the usually used amount of liquid substrate (200 µl), 400 µl was spread on the wafer in this case (this led to a drainage of the IL from the waver during sputtering, which is why the amount of liquid substrate was reduced in the subsequent experiments). Sputtering was performed at a power of P = 50 W for a time of t = 120 s at a target-to-substrate distance of W_d = 5 cm.

As a starting point, the visual appearance of the liquid is examined. Figure 15 shows an image of the as-sputtered sample.

Figure 15: Photograph of Pt sputtered onto [Bmim] [Tf_2N] for t = 120 s.

The IL is colorless in its pure form, so a color change has taken place during the sputtering process. A yellowish color is a typical feature of Pt NPs suspended in a solvent [123, 124]. This can be explained regarding the experimentally determined absorption spectrum of Pt NPs by Rajathi et al. given in Figure 16 [125].

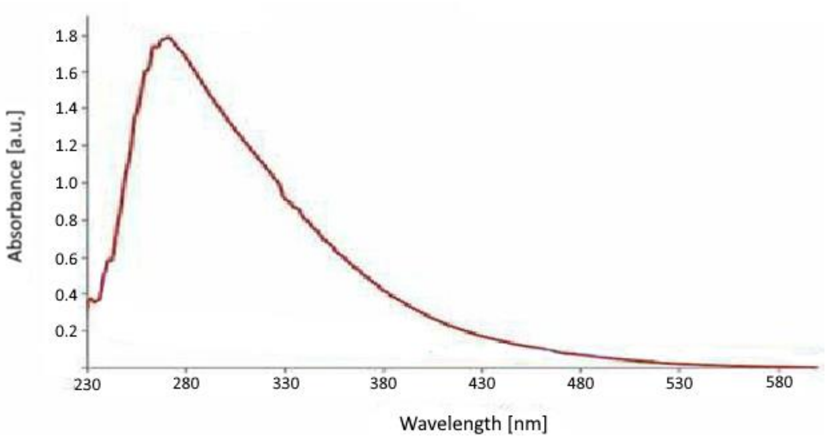

Figure 16: Absorption spectrum of Pt NPs prepared by reduction of a precursor. Adapted from [125].

The peak at 263 nm can be assigned to the Pt NPs. Even though the maximum absorbance is located in the ultraviolet (UV) range, there is still an increased absorbance at small wavelengths of the area of visible light induced by the Pt NPs. This means that some blue / violet light is absorbed. With yellow / orange being the corresponding complementary color [126], the yellowish color of the suspension is the consequence. Hence, this visual impression represents a first hint, that Pt particles have actually been produced using the described procedure.

For a more detailed analysis, SAXS was performed in the course of this pre-investigation. Therefore, a mixture of 20 µl of the pure sample with 600 µl EtOH was used, and a mixture of the equivalent volumes of pure [Bmim] [Tf_2N] with EtOH served as the reference. The measurement was conducted in the MAXS configuration since very small NPs were expected to be present in the suspension based on literature [57]. The exposure time was set to 30 minutes for each capillary. The scattering curve obtained from the experiment including the fitted curve is shown in Figure 17.

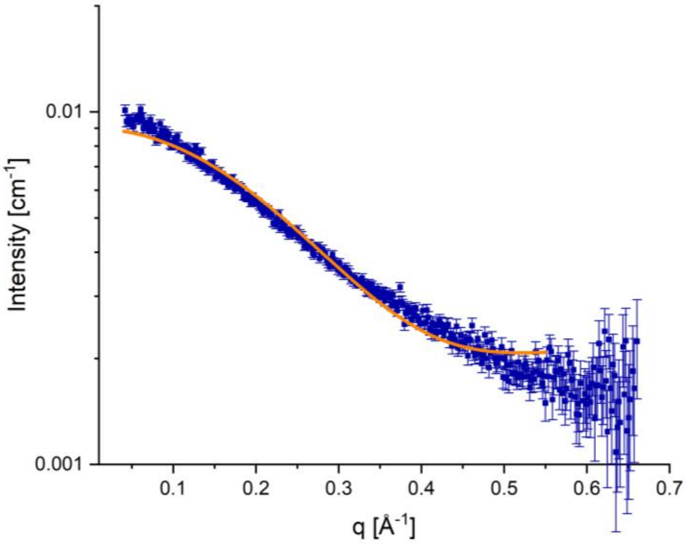

Figure 17: SAXS curve and fit of Pt sputtered onto [Bmim] [Tf_2N] (blue: raw data; orange: fit).

The fit considers all datapoints up to a value of q = 0.55 $Å^{-1}$. Higher values are excluded due to the increasing uncertainty of the datapoints illustrated by the error bars. The fit results in a mean particle size of (1.726 ± 0.007) nm. The very small uncertainty in the particle size accounts for a good agreement between the fit and the experimental data but does not include errors made in the non-trivial data treatment and fitting procedure. Therefore, the obtained mean particle size provides a first guide value in this instance.

The centrifuge was used to try to extract the NPs, applying the procedure specified in chapter 3.5. The extractable particle size relates to the centrifuge speed, so centrifuging can help to determine particle sizes. To calculate the separable particle size, the Stokes law can be used for non-interacting particles [127]:

$$v = \frac{2}{9} \cdot \frac{(\rho_\mathrm{P} - \rho_\mathrm{M}) \cdot g \cdot r^2}{\eta_\mathrm{M}} = \frac{2}{9} \cdot \frac{(\rho_\mathrm{P} - \rho_\mathrm{M}) \cdot g \cdot \left(\frac{d}{2}\right)^2}{\eta_\mathrm{M}} = \frac{2}{9} \cdot \frac{(\rho_\mathrm{P} - \rho_\mathrm{M}) \cdot \mathrm{g}_0 \cdot RCF \cdot \left(\frac{d}{2}\right)^2}{\eta_\mathrm{M}} \tag{4.1}$$

In equation (4.1), ρ_P and ρ_M are the mass densities of the particle and matrix material, v is the sedimentation velocity, g the gravitational field strength, g_0 the standard acceleration due to gravity, r the particle radius, η_M the matrix viscosity, RCF the relative centrifugal force and d the particle diameter. If the velocity is replaced by the travel distance s divided by centrifugation time t and the equation is rearranged to d, the following relationship is obtained:

$$d = 2 \cdot \sqrt{\frac{9}{2} \cdot \frac{\frac{s}{t} \cdot \eta_\mathrm{M}}{(\rho_\mathrm{P} - \rho_\mathrm{M}) \cdot \mathrm{g}_0 \cdot RCF}} \tag{4.2}$$

To apply equation (4.2), the density ρ_M and viscosity η_M of the ethanol / IL mixture need to be determined. After calculating the molar fraction of the IL to $x_\mathrm{IL} = 0.05$ using the volumes as well as the densities and molar masses of the pure substances [20, 128], ρ_M and η_M of this mixture are read from literature [129]:

$$\rho_\mathrm{M} = (0.85 \pm 0.02)\,\frac{\mathrm{g}}{\mathrm{cm}^3}$$
$$\eta_\mathrm{M} = (1.5 \pm 0.2)\ \mathrm{mPa \cdot s}$$

The density of Pt is 21.50 g/cm^3 [97]. Estimating a travel distance of $s = (1 \pm 0.3)$ cm, the extractable particle size can then be calculated to $d = (3.00 \pm 0.50)$ nm using equation (4.2).

After the applied centrifugation, no agglomeration of particles in the bottom of the tube was visible by eye. Even though this could also be attributed to some other reasons such as a low concentration of particles in the mixture, it provides a further hint that the fabricated particles are very small (i.e., smaller than (3.00 ± 0.50) nm).

To finalize the pre-investigation of sputtering Pt, a TEM grid was prepared by dropping 5 µl of the prepared IL+NPs solution on the grid and leaving it overnight, before dipping it in EtOH to remove the excess IL.

An EDX spectrum taken on the TEM grid is shown in Figure 18. No particles could be directly observed by TEM imaging, which is why the spectrum was recorded on a randomly chosen area on the grid.

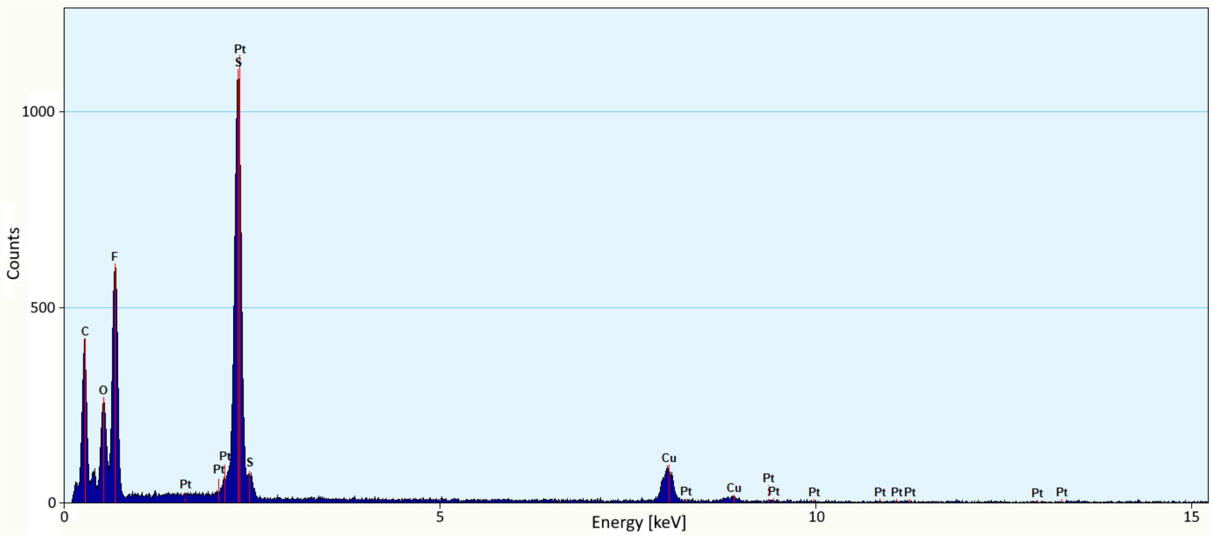

Figure 18: EDX spectrum of Pt sputtered onto [Bmim] [Tf$_2$N] (blue: raw intensity; red: theoretical peak positions).

Apparently, a large amount of IL is left on the grid as indicated by the appearance of carbon, fluorene and sulfur peaks in the spectrum. It cannot be stated clearly if Pt is present on the grid or not since the potentially occurring largest Pt peak overlaps with the large sulfur peak, and the smaller Pt peaks are not observable. This shows that care must be taken in the preparation of the grids in order to preserve a high particle concentration on the grids. For this reason, a more sophisticated grid preparation procedure was applied for further TEM investigations (compare chapter 3.6.2).

In conclusion, the conducted measurements indicate the formation of small Pt NPs by sputtering onto [Bmim] [Tf$_2$N]. Even though the produced NPs seem to be very small and are difficult to image directly, this pre-study demonstrates the capability of the sputtering setup of producing NPs by sputtering onto an IL at least in low concentrations. This provides motivation for further research using this technique and the applied system.

4.1.2 Pt_3Y target quality investigation

After testing the general sputtering setup (chapter 4.1.1), the Pt_3Y target was mounted into the sputter coater to investigate the target quality and characteristics. By examining sputtered Pt_3Y thin films, it was aimed to enable a better understanding for the subsequent NP fabrication in terms of compositions and chemical states. Therefore, sputtering was applied onto two small pieces of a Si-wafer for a time of t = 240 s at a power of P = 50 W and a target-to-substrate distance of W_d = 8 cm.

One of the two produced thin films was acid-treated by dipping it into 0.1 M $HClO_4$ for 20 minutes. The sample was then washed gently with ultrapure water and finally dried with N_2. This sample is referred to as acid-treated, the other one as as-deposited.

The overall composition of the two films was determined by EDX. Figure 19 shows a recorded EDX spectrum of the as-deposited Pt_3Y film. The occuring peaks can be assigned to Si, Y and Pt. The film thickness of roughly 110 nm according to the calibration measurements (compare chapter 3.2) is smaller than the depth from which generated characteristic X-rays can leave the sample [107]. As a consequence, the wafer produces a signal as well, leading to the observed Si-peak.

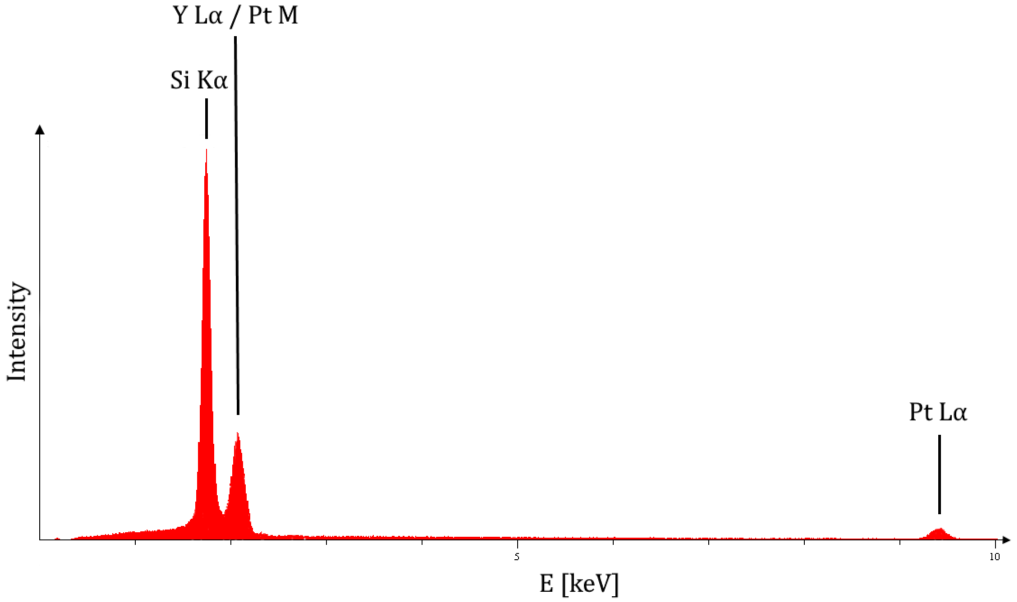

Figure 19: EDX spectrum of as-deposited Pt_3Y film.

The atomic concentrations of Pt and Y are listed in Table 4. The errors represent the standard deviation based on three different EDX measurements per sample.

Table 4: Atomic concentrations of Pt and Y in thin films determined by EDX.

	as-deposited	**acid-treated**
$at\%_{Pt}$	69.08 ± 0.35	69.46 ± 0.20
$at\%_{Y}$	30.92 ± 0.35	30.54 ± 0.20

The Pt:Y ratio of the as-deposited sample calculated from the values in Table 4 is 2.23 : 1. Compared to the theoretical ratio of 3:1, the Pt concentration is slightly lower. This could be a result of preferential sputtering of Y, which in turn can be explained by the evaporation enthalpies ΔH_v of the two metals ($\Delta H_{v,Pt}$ = 510 kJ/mol; $\Delta H_{v,Y}$ = 363 kJ/mol [130]). Despite sputtering being a momentum transfer process and hence the evaporation enthalpies playing a rather minor role for pre-alloyed targets [53, 54], the evaporation enthalpies may still have a certain influence (compare equation (2.9); the surface binding energy can be set equal to the evaporation enthalpy [51]). In this case, the lower value for Y leads to a higher sputtering yield and thus a higher concentration in the sputtered film [51]. However, the deviation from the optimum ratio is rather small, which is why it is still reasonable to assume that the real target composition is nearly Pt_3Y as stated by the manufacturer of the target. This assumption is also made in the context of the errors in Table 4 including the standard deviations but not the errors of each single measurement itself.

The atomic percentages of Y and Pt in the acid-treated sample do not differ significantly from those of the as-deposited one. This results from the acid-treatment only affecting the very top atomic layers of the film. The loss of Y is thus very small and does not show up in a bulk material analysis like EDX.

As a second technique, XPS was applied to both films on the one hand to compare the composition results to the ones obtained by EDX and on the other hand to investigate the chemical state of the sputtered elements in the thin films. Figure 20 shows an XPS survey spectrum of the as-deposited film.

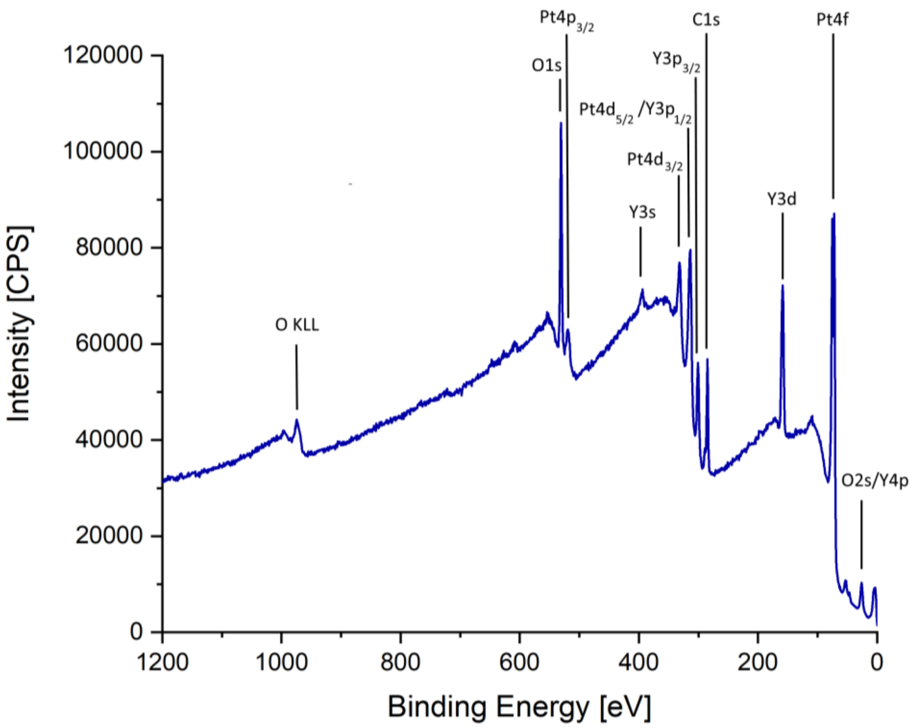

Figure 20: XPS survey spectrum of as-deposited Pt_3Y film.

All relevant peaks are labeled in the spectrum. The majority of the peaks can be assigned to Pt and Y. Also carbon can be detected. This is a common effect owing to the so-called adventitious carbon, which describes a thin layer of adsorbed carbon on samples that are exposed to ambient atmosphere [131]. Similar applies to oxygen, especially in the presence of easily oxidizable species in the sample, such as yttrium.

The survey spectrum of the acid-treated film exhibits qualitatively the same peaks as the one given in Figure 20, which is why it is not shown here.

The atomic concentrations of Pt and Y, provided by the XPS measurements, are listed in Table 5. Again, the errors represent the corresponding standard deviations. It is noticeable that the percentage of Y in the as-deposited sample is significantly higher than the bulk alloy Y-content shown by EDX. This is a commonly observed effect [41, 42], which can be attributed to the oxidation of surface-near Y leading to an enrichment of Y at the surface [41]. The acid-treatment increases the Pt:Y ratio drastically compared to the as-deposited sample. This clearly demonstrates the removal of Y from the surface by the acid, as described in chapter 2.2. The remaining Y signal in the acid-treated sample determined by XPS originates from the bulk alloy material underneath the formed Pt overlayer.

Table 5: Atomic concentrations of Pt and Y in thin films determined by XPS.

	as-deposited	**acid-treated**
$at\%_{Pt}$	54.55 ± 0.64	88.14 ± 0.11
$at\%_{Y}$	45.45 ± 0.64	11.86 ± 0.11

The Pt4f and the Y3d peaks were fitted using the procedure explained in chapter 3.6.7 after shifting the spectrum to the metallic Pt peak at 71.2 eV (it is assumed that the majority of the Pt is kept in the metallic state). Beside the restrictions on the peak positions given before, the binding energies of the different peaks were set to differ by ±0.2 eV between the as-deposited and the acid-treated sample. Figure 21 shows how the Pt4f peaks are constituted by the contributions of metallic Pt and Pt oxides.

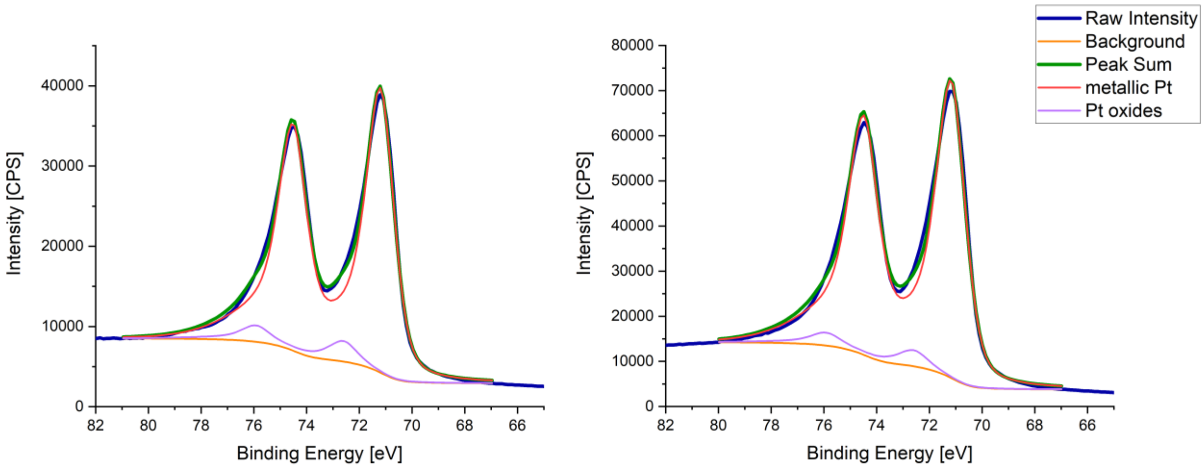

(a) (b)

Figure 21: Fitted XPS Pt4f peaks of thin films: (a) As-deposited film; (b) Acid-treated film.

It can be seen that the spectrum and its contributions do not differ between the as-deposited sample (Figure 21(a)) and the acid-treated one (Figure 21(b)). As expected regarding the inert character of Pt, both films contain mostly metallic Pt and some Pt oxides. The chemical state is not affected by the acid-treatment.

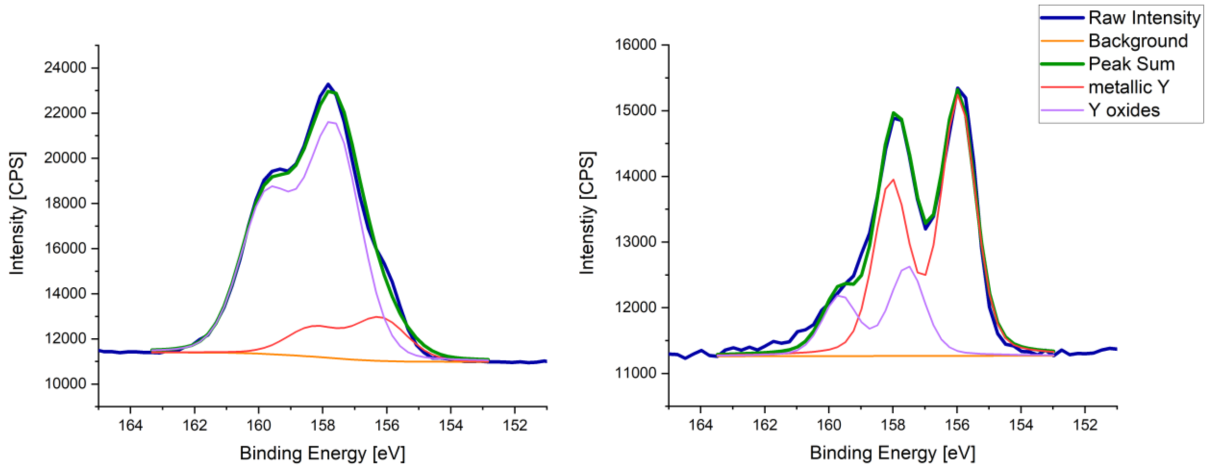

(a) (b)

Figure 22: Fitted XPS Y3d peaks of thin films: (a) As-deposited film; (b) Acid-treated film.

The situation is different for yttrium, as shown in Figure 22. The majority of the Y at the surface is oxidized in the as-deposited sample (compare Figure 22(a)). Not surprisingly, only a little contribution of metallic Y is visible in the fitted spectrum due to the high oxygen affinity of Y. However, the Y-oxide layer is thinner than the depth probed by XPS, so there is signal from the metallic Y which lies in the alloy beneath. This proves the capability to obtain metallic Y in the sputtered species, which is of fundamental importance for the application of Pt_3Y NPs.

After the acid-treatment, the Y3d peak shown in Figure 22(b) shows a lot more metallic Y. As expected, the oxidized Y is removed from the surface and the residual surface-near Y is mainly of metallic nature.

To summarize the pre-investigation of the Pt_3Y target, it can be said that the results of EDX and XPS measurements show the expected trends. There is a good agreement between the fitted Y3d spectra in this work and the ones observed for Pt_3Y films by Lindhal et al. [14]. These outcomes reveal a satisfactory quality of the applied Pt_3Y target and thus ensure an intact material's system for the subsequent research.

4.1.3 Heating experiments of liquid substrates

As explained in chapter 2.3, the substrate may heat up to a certain degree during sputtering [51]. Since the used sputter coater did not contain an in-situ temperature measurement or control for the substrate, the maximum substrate temperature during sputtering was not known. To investigate whether an enhanced temperature would affect the chemical structure of the substrate liquids, Raman spectroscopy was applied for [Emim] [OTf] and PEG 600. 200 µl of both substances was filled in a small glass vial and heated at 160 °C for 300 s.

Figure 23 shows a photograph of the heated (right) and for comparison of the not heated (left) [Emim] [OTf].

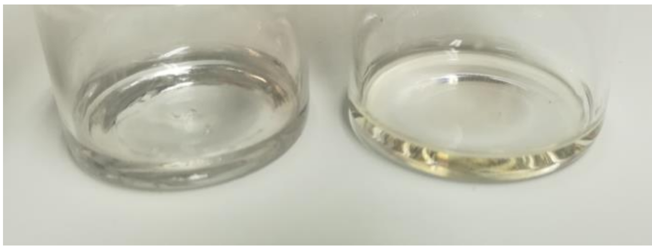

Figure 23: Photograph of not heated and heated [Emim] [OTf] (left: not heated; right: heated).

A slight yellowish coloring can be observed after the applied heat-treatment. A very similar behavior is received for PEG. This effect might contribute to the color change during sputtering described in chapter 4.1.1, but it is not sufficient to explain the deeper yellow color observed in Figure 15 or even the dark brown color obtained for longer sputtering times (compare Figure 26 and Figure 32). However, the observed discoloration in the heating experiment raises the question whether the chemical structure of the liquid changes significantly by the temperature rise. To approach this issue, the Raman spectra of the not heated and heated substances are considered. Figure 24 shows the spectra for [Emim] [OTf].

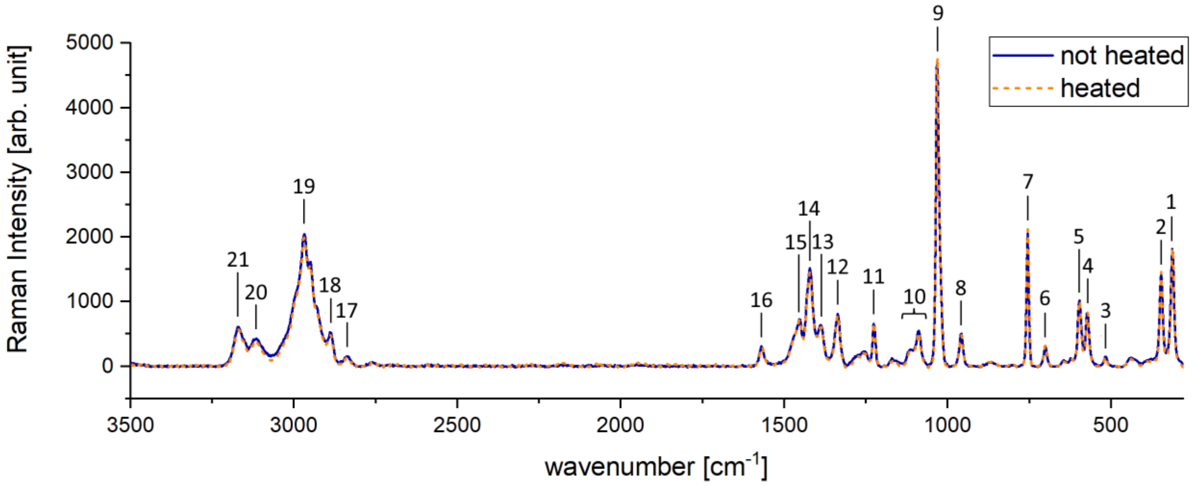

Figure 24: Raman spectra of not heated and heated [Emim] [OTf].

The peaks labeled in Figure 24 are assigned to certain bond vibrations in Table 6 [132, 133]. Hereby, ν describes a stretching, ρ a rocking, δ a scissor vibration, σ a bond oscillation, π a wagging and τ a twisting. The indices ‘s’ and ‘as’ identify the vibration as symmetric or antisymmetric.

Table 6: Peak assignment for [Emim] [OTf] Raman spectra.

Peak number	Molecule	Vibration description
1	$[OTf]^-$	ν_s(C-S)
2	$[OTf]^-$	$\rho(SO_3)$
3	$[OTf]^-$	δ_{as}(O-S-O) + δ_{as}(F-C-F)
4	$[OTf]^-$	δ_s(O-S-O) + δ_s(F-C-F)
5	$[OTf]^-$	σ(S-O)
6	$[Emim]^+$	σ(C-N-C)
7	$[OTf]^-$	δ_s(F-C-F) + ν_s(C-S)
8	$[Emim]^+$	π(N-C-H)
9	$[OTf]^-$	$\nu_s(SO_3)$
10	$[Emim]^+$	Cation vibration (not clearly assignable)
11	$[OTf]^-$	$\nu_{as}(CF_3)$
12	$[OTf]^-$	$\nu_{as}(SO_3)$
13	$[Emim]^+$	π(H-C-H)
14	$[Emim]^+$	δ(H-C-H) + ν_s(C-N)
15	$[Emim]^+$	δ(H-C-H) + ν_s(C-N)
16	$[Emim]^+$	ρ(C-H) + ν_s(C-N) + ν_s(C=C)
17	$[Emim]^+$	ν_s(H-C-H)
18	$[Emim]^+$	ν_s(H-C-H)
19	$[Emim]^+$	ν_{as}(H-C-H)
20	$[Emim]^+$	ν_s(C-H)
21	$[Emim]^+$	ν_s(H-C=C-H)

As can be seen in Figure 24, the Raman spectra for the not heated and the heated [Emim] [OTf] are identical. This means that the chemical structure of the substance is not affected by the heat-treatment, which is fundamental for the IL to perform the intended stabilizing function. The thermal stability of imidazolium-based ILs depends mostly on the type of the anion [134]. Because the [OTf] and [Tf2N] anions exhibit very similar thermal properties [135], it can be assumed that none of the corresponding ILs will change much at 160 °C. These results are in line with the values of the ILs' (short term) decomposition temperatures, which are far above the applied heat-treatment temperature of 160 °C [136]. For the [FAP] based IL, the decomposition onset temperature is somewhat lower than for the [OTf] and [Tf2N] ILs, but still of a similar magnitude [137].

The two spectra including the peak assignments for PEG 600 are shown in Figure 25 [138–140].

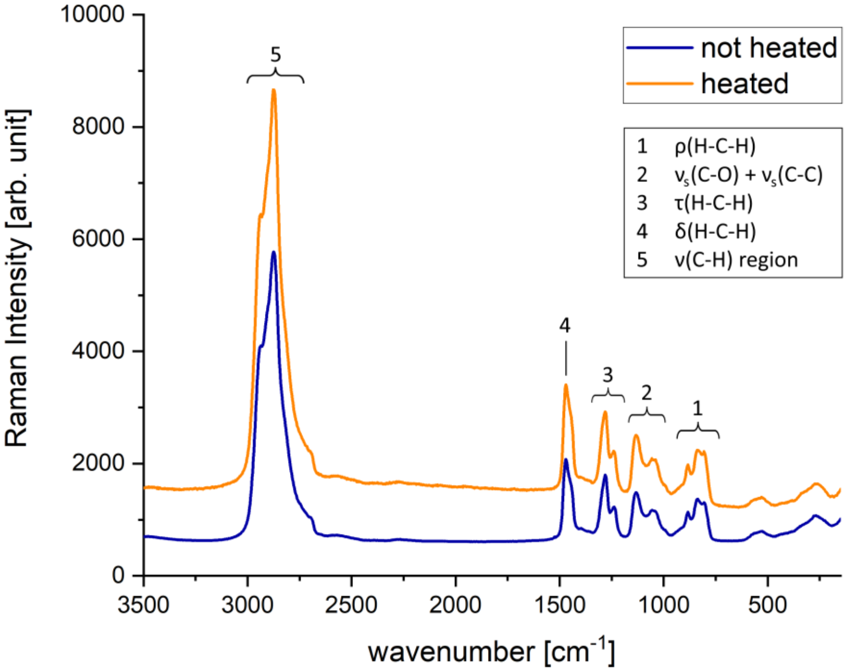

Figure 25: Raman spectra of not heated and heated PEG 600.

Here, the complete spectrum of the heat-treated sample is shifted slightly upwards compared to the spectrum of the not heated one. This implies a higher background, which is typically assigned to fluorescence effects and could possibly originate from fluorescent impurities [137]. The important observation here is that the peak positions and relative intensities remain unchanged during the heat-treatment. A polymer degradation would alter those peak properties. For example, in PEG with an average molecular weight of 400 g/mol a new peak at roughly 1720 cm^{-1} would appear [140]. Since this is not the case, it can be assumed that the heating to 160 °C does not affect the polymer structure significantly.

It is important to clarify once more that the actual temperature of the substrate liquids during sputtering is not known. However, it is not believed that a dramatic temperature increase takes place since the sputtering times are rather short compared to some other studies [65, 67, 69] and most of the power typically results in heating of the target and not the substrate [53]. For this reason, the results of the Raman measurements are considered as a strong argument for the liquid substrate structure not to change during the sputtering process.

4.2 Pt_3Y nanoparticle fabrication

The objective of the experiments conducted for this chapter was to investigate whether Pt_3Y NPs can be produced and to examine their characteristics when fabricated under varying conditions.

4.2.1 Influence of the type of ionic liquid substrate

To start the study on Pt_3Y NPs, different ILs were chosen as liquid substrates. [Emim] [OTf], [Emim] [Tf_2N] and [Emim] [FAP] were applied to investigate potential anion effects. Furthermore, [Dmim] [Tf_2N] was used in order to cover effects induced by an enlargement of the alkyl chain in the cation. The samples were prepared by sputtering at a power of P = 50 W and a target-to-substrate distance of W_d = 8 cm for a time of t = 300 s.

Figure 26: Photograph of Pt_3Y sputtered onto [Emim] [OTf] for t = 300 s.

A photograph of the sample sputtered onto [Emim] [OTf] is given in Figure 26. A very similar color change from colorless before sputtering to brown afterwards can be observed for the other three ILs, which indicates the presence of NPs in solution. The colors observed here are more intense than for the sample prepared in the context of the pre-study (compare chapter 4.1.1, Figure 17). It is important to keep in mind that Pt_3Y (and not Pt) is used here, which may have a certain influence on the color of the produced sample. However, it is very likely that the described color difference results from the longer sputtering time of 300 seconds compared to 120 seconds in the pre-study. As explained in chapter 2.3.2, this leads to a higher concentration of formed species in solution [59, 62, 64, 65, 67] and consequently to a darker color of the sample.

For a more detailed analysis, SAXS experiments for the four different ILs+NPs were conducted in the diluted samples (20 µl of the sample and 600 µl EtOH). Mixtures of 20 µl of the pure IL with 600 µl EtOH were used as references. To cover a preferably big size range of species inside the liquid, the SAXS setup was chosen. The exposure time was set to 30 minutes for each capillary. The results of the measurements as well as the fitted curves are presented in Figure 27. For the purpose of comparison, the ranges of the axes are set equal for the four diagrams.

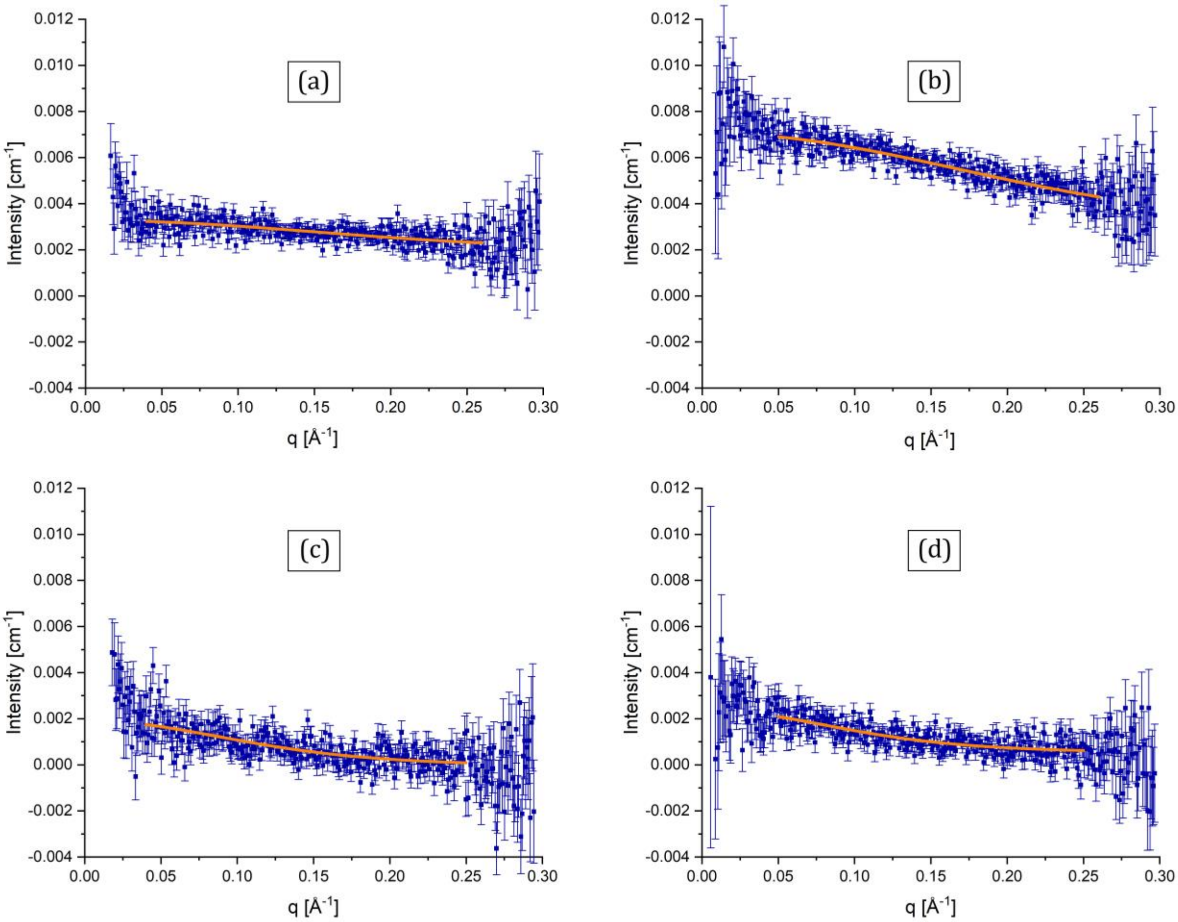

Figure 27: SAXS curves and fits of Pt_3Y sputtered onto different ILs: (a) [Emim] [OTf]; (b) [Emim] [Tf_2N]; (c) [Emim] [FAP]; (d) [Dmim] [Tf_2N]; (blue: raw data; orange: fits).

At a first glance, the large error bars in the experimental data for each of the four samples attract attention. On the one hand, this is a result of the comparatively small measurement time of 30 minutes. On the other hand - and this is the more important factor - the used SAXS setup leads to higher uncertainties in the data (compared to the MAXS setup). This becomes obvious when comparing the four SAXS curves given in Figure 27 to the one prepared in the context of the pre-study in Figure 17. Due to those large error bars, the diagrams in Figure 27 are plotted with linear intensity axes. Standard SAXS plots with logarithmic vertical axes would let the error bars appear even larger and thus make the diagrams very unclear.

The signal-to-noise ratio is small for all four liquid substrates due to short sputtering times and strong dilutions leading to small NP concentrations in the samples. Furthermore, EtOH is not a good solvent for every IL. Regardless, the signals are not flat, which indicates the presence of particles. The measured data at the edges of the q-range exhibit typically very large uncertainties and are therefore neglected for fitting. It can be already observed in Figure 27 that the scattered intensities vary slightly between the four liquid substrates. This points out differences in the particle sizes.

To better compare the data to each other, the resultant fits are plotted together in one diagram in Figure 28. A logarithmic intensity-axis is used since this is more suited to reveal slight differences between the curves. The background of the SAXS profiles originates mostly from incoherent scattering of X-rays at electrons, scattering at the capillaries and residual air as well as the beamline optics [109, 110]. These background contributions may be slightly different for the different ILs and / or capillaries, which is why a sensible comparison of the different fits is ensured by shifting them to the same background. Therefore, the fits are shifted to a background value of 0.001 cm^{-1} at their highest q-value.

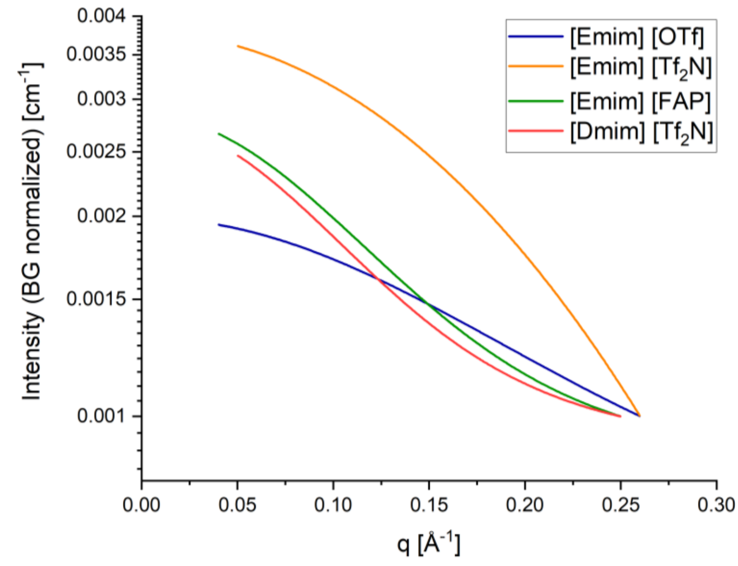

Figure 28: Comparison of SAXS fits of Pt_3Y sputtered onto different ILs.

Regarding Figure 28, one may assume the diameter *d* of the particles in [Emim] [Tf_2N] to be slightly larger than in the other liquids, owing to the larger slope of the curve at high q-values, which is the case as presented in Table 7. The determined diameters of the particles lie all between 1 nm and 2 nm with the particles in [Emim] [Tf_2N] being the largest. However, due to the large uncertainties for every single data-point and the low signal-to-noise ratio (compare Figure 27), the errors in the determined particle sizes given in Table 7 are partially enormous relative to the absolute values of the sizes. For this reason, a reasonable comparison of the sizes of particles dispersed in the different ILs is not possible here. Nevertheless, the SAXS experiments imply the existence of small particles in all four tested liquid substrates.

Table 7: Particle sizes of Pt_3Y sputtered onto different ILs determined by SAXS.

	[Emim] [OTf]	**[Emim] [Tf$_2$N]**	**[Emim] [FAP]**	**[Dmim] [Tf$_2$N]**
***d* [nm]**	1.04 ± 141.18	1.97 ± 0.23	1.54 ± 14.79	1.54 ± 13.04

DLS was used to compare the SAXS results to. This was applied for one of the ILs, namely [Dmim] [Tf$_2$N], as this was soluble in EtOH. 20 µl of the sputtered IL+NPs was diluted with 1000 µl EtOH and measured in the DLS system. To ensure good statistics, three records consisting of 18 individual measurements each were performed. These are plotted in Figure 29(a).

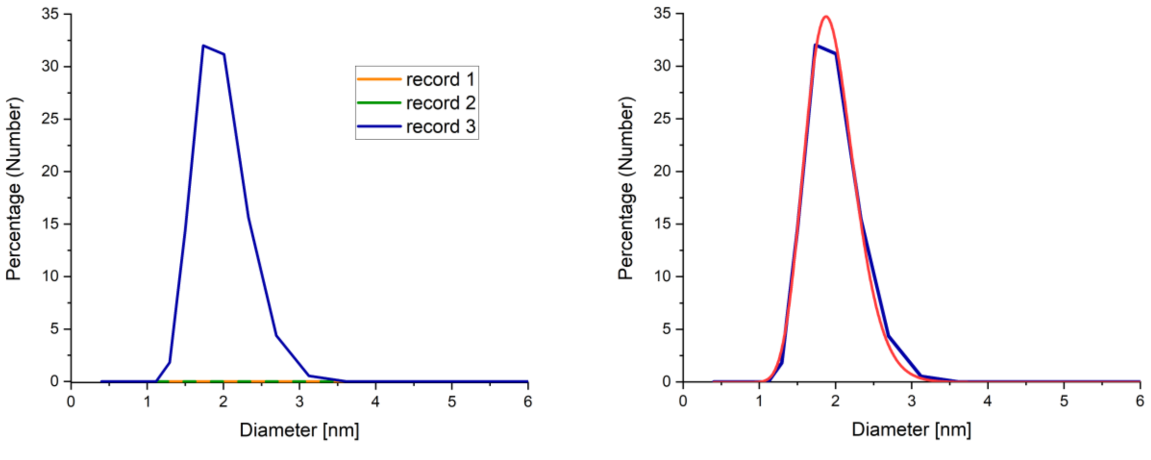

(a)

(b)

Figure 29: DLS number particle size distribution of Pt_3Y sputtered onto [Dmim] [Tf$_2$N]: (a) Plots of the 3 records; (b) Record 3 (blue) and fit (red).

The peak in the third record confirms the existence of particles in the size range of a few nanometers. For a quantitative analysis, this peak is fitted with a lognormal size distribution of the general form

$$p_{\mathrm{n}}(d) = p_{\mathrm{n},0} + \frac{A}{\sqrt{2 \cdot \pi} \cdot w \cdot d} \cdot \exp\left(- \frac{\left(ln\left(\frac{d}{d_{\mathrm{c}}}\right)\right)^2}{2 \cdot w^2} \right) \tag{4.3}$$

where p_{n} is the number percentage, d the particle diameter and $p_{\mathrm{n},0}$, A, w and d_{c} are constants. The result of the fitting procedure is illustrated in Figure 29(b). The mean and standard deviation (given as the error) of the particle diameter can be calculated from the constants in equation (4.3), which is performed by the plotting software (OriginPro 2020):

$$d_{\mathrm{mean}} = (1.96 \pm 0.34)\ \mathrm{nm}$$

The lognormal distribution is very usual to be found for NPs [141, 142]. The fact that the data can be fitted very precisely with this type of distribution thus suggests that the observed peak arises from particles and is not an artefact of the measurement. Taking this as a basis, the distribution points out a narrow spread, i.e., a good control over the NP diameter. This represents an important result for the application of the NPs in catalysis, which typically requires well-defined particle sizes for an optimal performance.

However, only one of the 3 records exhibits this peak, as shown in Figure 29(a). This indicates that DLS may not be the most suited and reliable technique for the characterization of the NPs produced in this work. It might serve as a supporting method, but not as one of the fundamental approaches for size quantifications and comparisons between different samples. For the latter purpose, SAXS, UV-Vis and TEM are more convenient and were therefore applied for further experiments.

Finally, the four samples were subjected to UV-Vis absorption spectroscopy to characterize and compare them to each other. 20 µl sputtered IL+NPs was diluted with 500 µl solvent (acetone for [Emim] [Tf_2N], [Emim] [FAP] and [Dmim] [Tf_2N]; ultrapure water for [Emim] [OTf]) and a mixture of the corresponding volumes of pure IL with solvent was used as a reference. Here, the solvent was selected for the best long-term stability of the NPs in the IL-solvent mixtures (no NP agglomeration after several days to weeks). Figure 30 shows the UV-Vis spectra obtained for the diluted solutions. Since very little information on concentrations and the nature of eventually occurring species in the different samples is present, the spectra are normalized to the absorbance interval from 0 to 1. In this way, a qualitative comparison of the curves can be carried out best.

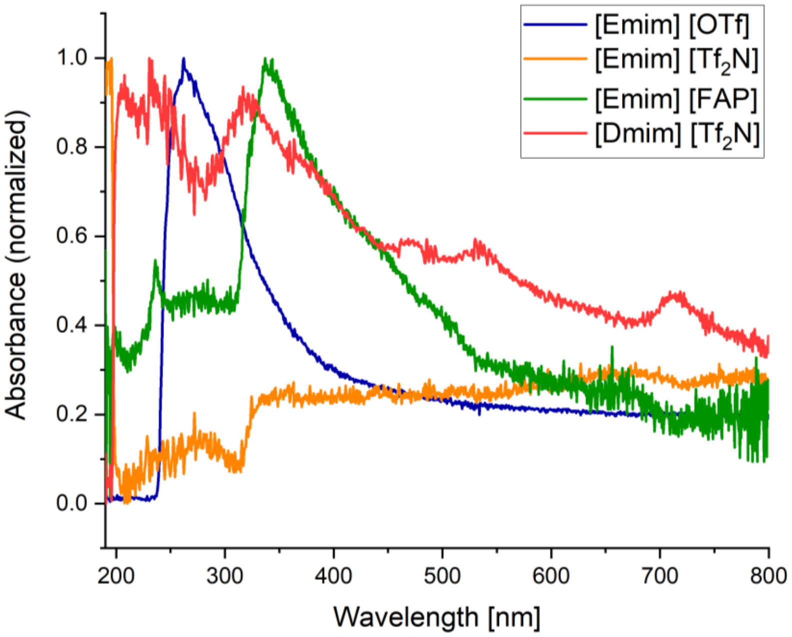

Figure 30: UV-Vis absorption spectra of Pt_3Y sputtered onto different ILs.

As explained in chapter 3.6.6, the absorbance curves are generated by subtracting the absorbance of the pure solvent from the sample absorbance. Hence, the existence of absorbance values larger than zero imply a difference in the absorption behavior between sample and reference. The appearance of certain, well-defined features in the spectra such as peaks and absorption edges proves that certain species with an absorption behavior different from the matrix material have been introduced by the sputtering process.

The UV-Vis spectra of the four sputtered ILs+NPs differ significantly from each other. This indicates a dependence of the occurring processes on the type of IL. Due to Pt_3Y being a not very commonly used material and especially the fabrication of NPs from this alloy being a very novel field of research, there exists, to the best of the author's knowledge, no experimental UV-Vis absorption data for Pt_3Y particles to compare to.

However, a UV-Vis absorption spectrum for spherical NPs in solution most likely exhibits a small number of peaks if no further species are present [143, 144]. A high symmetry reduces the number of peaks, which is why for spherical NPs usually a single peak can be observed [144]. The UV-Vis spectra of Pd_3Y NPs for example exhibit no unusual features compared to more common metallic NPs [145], so the presence of yttrium in itself should not lead to any unconventional effects. On the basis of these considerations, the obtained absorbance curves in Figure 30 can be assessed in more detail. The spectra for [Emim] [Tf_2N], [Emim] [FAP] and [Dmim] [Tf_2N] exhibit more than one single peak or absorption edge in the measured wavelength range. Many features are present and partially seem to overlap, which results in spectra that are very unusual for (especially spherical) NPs. This does not mean that no NPs have been produced in these ILs at all. In fact, the observations made before in the SAXS and DLS experiments suggested the existence of particles. But the results show clearly that if NPs are present, they are not the only species that formed inside the liquid and there are multiple changes to the ILs due to the Pt_3Y sputtering. These observations might be attributed to the combination of Y with ILs. As Y is so oxyphilic, it possibly reacts with the ILs and forms some irregular organometallic structures. This suggestion is supported by results obtained from TEM, EDX and XPS investigations in chapter 4.2.3.

Compared to the other spectra, the absorbance curve of the sputtered [Emim] [OTf] features a clear single peak. As explained before, this characteristic of the spectrum refers to the existence of spherical NPs in the system. This represents a strong indication for the successful fabrication of NPs in this IL. The peak position occurs at a wavelength of 263 nm, which accords perfectly with the values found for Pt NPs by several groups [125, 146, 147]. However, no definitive statement on the particle stoichiometry can be made based on this result. As a final remark, it should be kept in mind that the sputtered [Emim] [OTf] was mixed with water for the UV-Vis study, whereas the other ILs were diluted with acetone. Even though the presence of acetone did not have a major influence on the UV-Vis absorption spectrum of Pd_3Y in a study performed by Brandiele et al. [145], it cannot be ruled out that the acetone (maybe in combination with the ILs) has some effect on the spectra obtained here. Unfortunately, it is not possible to conduct measurements with water as a diluting solvent for [Emim] [Tf_2N], [Emim] [FAP] and [Dmim] [Tf_2N], as they are not soluble.

In any case, the results obtained for sputtering Pt_3Y onto [Emim] [OTf] for the fabrication of NPs are encouraging. Therefore, this system is chosen for further investigations and optimizations in the following chapters.

4.2.2 Influence of sputtering time and sputtering distance

A high concentration of the NPs in the liquid substrate is advantageous since this allows for higher signals in various analysis methods. Furthermore, when considering the possible application of the NPs produced by this method, a high concentration is indispensable for efficient and economic fabrication procedures. For these reasons, the NP concentration was investigated by means of UV-Vis spectroscopy for different sputtering times and distances. Regarding the sputtering theory, both an increased sputtering time t and a decreased target-to-substrate distance W_d should lead to a higher particle concentration (compare chapter 2.3.2). There are however no established quantitative relationships between those parameters, which is why an experimental study was conducted here. As shown in chapter 4.2.1, Pt_3Y-sputtered [Emim] [OTf] exhibits a distinct peak in UV-Vis spectroscopy, which is why this liquid substrate was used for this purpose. The applied sputtering setups were:

(A) W_d = 8 cm; t = 300 s
(B) W_d = 6 cm; t = 300 s
(C) W_d = 8 cm; t = 3 x 300 s
(D) W_d = 4 cm; t = 30 s

The sputtering power was P = 50 W for all samples. For recording the UV-Vis spectra, 20 µl of the pure sputtered sample was mixed with 600 µl ultrapure water. A mixture of the corresponding volumes of pure IL with ultrapure water provided the background intensity. The UV-Vis absorption curves of the four different samples are shown in Figure 31.

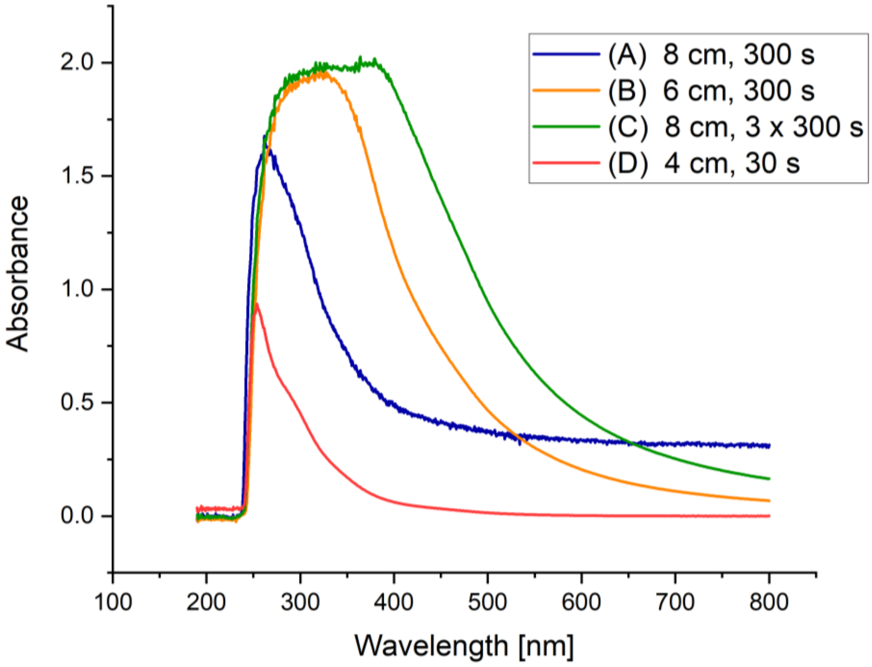

Figure 31: UV-Vis absorption spectra of Pt_3Y sputtered onto [Emim] [OTf] for different sputtering times and distances.

First of all, it can be observed that all four spectra exhibit a single peak and the different sputtering setups do not have any influence on the position of the absorption edge at 250 – 270 nm. This validates a successful sputtering process for all setups and enables a sensible comparison of the different curves.

To start with, different sputtering distances at a constant sputtering time of t = 300 s are examined ((A) and (B)). The decreased target-to-substrate distance for sample (B) results in a higher and somewhat broader absorbance peak. The increased absorbance values in general can be ascribed to an increased particle concentration according to the Bouguer-Lambert-Beer law introduced in chapter 3.6.6. This behavior is easily understandable regarding the sputtering process. The sputtering emission typically follows a cosine angular distribution [54, 148], which means that atoms are distributed from the target in every direction. Therefore, the probability of an atom reaching the substrate is higher for smaller target-to-substrate distances. Hence, more species reach the substrate in the total sputtering time and more NPs can be formed. Interestingly, the absorbance peak is broadened towards higher wavelengths for the decreased sputtering distance. In general, increased absorbance values at higher wavelengths imply the existence of slightly larger particles [59, 60]. It can thus be concluded that the decreased sputtering distance leads to a slightly broader particle size distribution. This might in fact be a result of the increased particle concentration, which results in a somewhat higher probability for small particles to meet and coalesce within the liquid. Alternatively, an increased substrate temperature induced by the decreased sputtering distance could be the origin of this effect.

The argumentation is very similar for increased sputtering times at a constant target-to-substrate distance of W_d = 8 cm ((A) and (C)). Understandably, more sputtered species reach the substrate in the increased time span, which leads to a higher particle concentration for sample (C). The high concentration is reflected in a dark brown color of the liquid sample (compare Figure 32). Also, a broader peak indicating a broader particle size distribution can be observed here.

Figure 32: Photograph of Pt_3Y sputtered onto [Emim] [OTf] for t = 3 x 300 s.

Finally, the combined effect of low sputtering times and distances is analyzed. Sample (D) clearly exhibits the lowest peak absorbance. The effect of the decreased sputtering time predominates and overbalances the decreased target-to-substrate distance. This is a result of the sputtering time being decreased by a much higher factor than the sputtering distance compared to the other samples. However, longer sputtering times at this small distance were not applied in order to obviate a strong heating of the liquid substrate.

The two sputtering setups (B) and (C) exhibit a very similar peak absorbance value, indicating comparable NP concentrations. The setup with the longer sputtering time (C) may result in a slightly broader particle size distribution as deduced from Figure 31. However, there is a risk of enhanced substrate heating at the lower sputtering distance, whereas the longer sputtering time is split into several sputtering intervals and hence does not lead to stronger substrate heating compared to setup (A). Therefore, setup (C) with W_d = 8 cm and t = 3 x 300 s is chosen for further experiments.

4.2.3 Nanoparticle characterization in [Emim] [OTf] and PEG 600

To further investigate the nature of the formed species, more analysis methods were applied to the sample sputtered onto [Emim] [OTf] at a power of P = 50 W and a target-to-substrate distance of W_d = 8 cm for a time of t = 3 x 300 s.

XPS was performed directly in [Emim] [OTf] after sputtering to examine if it contained any Pt or Y, and in which composition. To approach this issue, 15 µl of the sputtered IL+NPs was dropped on a cleaned GCE, which was subsequently inserted into the XPS system. The survey spectrum of the corresponding measurement is shown in Figure 33. Beside the elements that are to be assigned to [Emim] [OTf] (O, F, N, C, S), a small Pt peak can be observed. This proves the existence of sputtered species inside the IL. XPS being an extremely surface sensitive method, only a very small amount of Pt can contribute to the signal, which accounts for the low measured intensity.

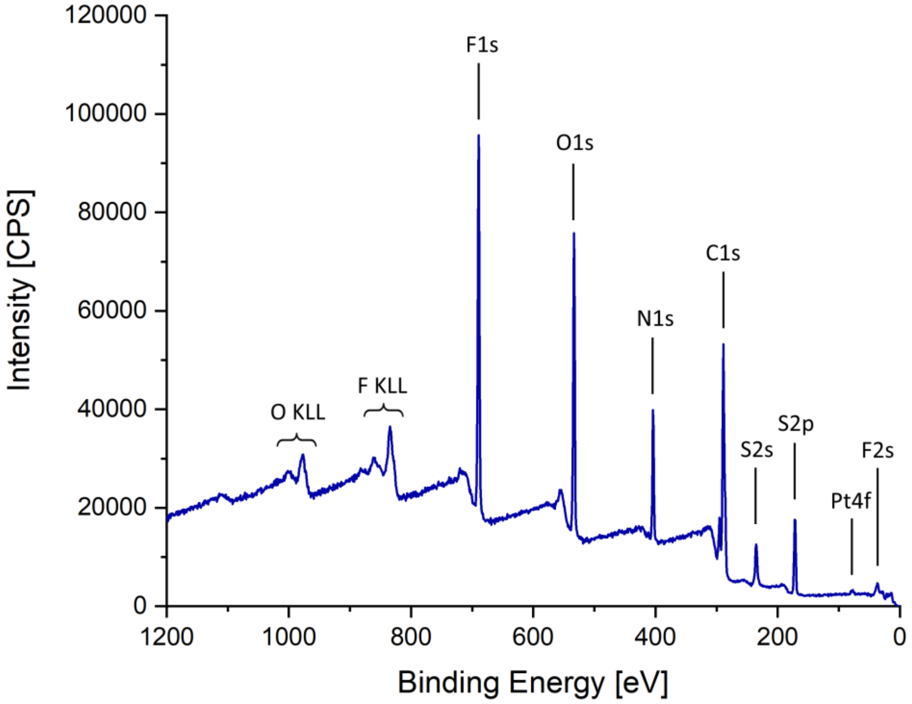

Figure 33: XPS survey spectrum of Pt_3Y-sputtered [Emim] [OTf] drop.

To determine the chemical state of the Pt, a narrow-range scan was executed. Figure 34 shows the spectrum after shifting it to the carbon peak at 284.8 eV [117]. The doublet can be fitted with a reasonable quality with only the pure metallic Pt contribution at 71.2 eV [118]. This assures the occurrence of metallic Pt inside the IL.

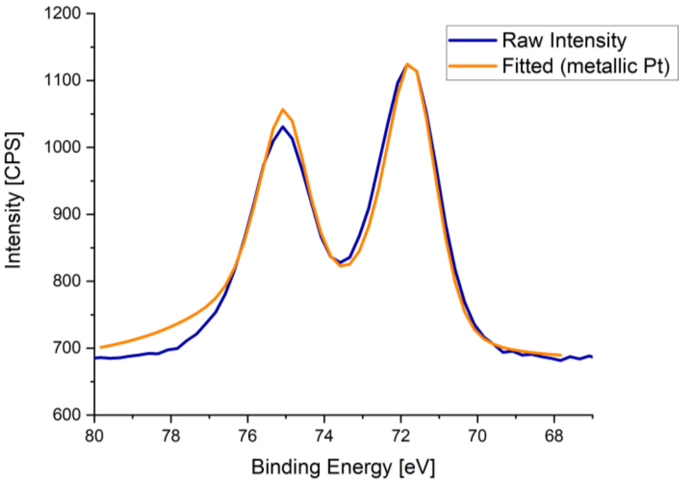

Figure 34: Fitted XPS Pt4f peak of Pt_3Y-sputtered [Emim] [OTf] drop.

Because the overall concentration of Y is even smaller than of Pt, no Y peak is observable in the survey spectrum. Alternatively, the Y is not present at the very surface of the drop (as opposed to Pt), which would mean a separation of Pt and Y inside the IL. This idea is picked up again in the following experiments. In any case, the lack of a Y peak in the spectrum prevents the determination of the Pt:Y ratio in the liquid by means of XPS.

For this reason, the less surface sensitive XRF technique was applied on a sample with exactly the same sputtering parameters. The measurement was conducted in a mixture of 180 µl of the Pt_3Y-sputtered [Emim] [OTf] with 4.8 ml ultrapure water. The obtained weight percentages of Pt and Y in the mixture are

$$wt\%_{\mathrm{Pt}} = 0.067 \pm 0.008$$
$$wt\%_{\mathrm{Y}} = 0.008 \pm 0.003$$

The atomic percentages can be expressed as given in equations (4.4) and (4.5), where all present elements that are neither Pt nor Y are combined in the rest marked by the index r. n represents amounts of components, m total masses and M molar masses. The applied approximations are justified by the mass of the rest (water plus IL) being much higher than the masses of Pt and Y.

$$at\%_{\mathrm{Pt}} = \frac{n_{\mathrm{Pt}}}{n_{\mathrm{Pt}} + n_{\mathrm{Y}} + n_{\mathrm{r}}} = \frac{\frac{m_{\mathrm{Pt}}}{M_{\mathrm{Pt}}}}{\frac{m_{\mathrm{Pt}}}{M_{\mathrm{Pt}}} + \frac{m_{\mathrm{Y}}}{M_{\mathrm{Y}}} + \frac{m_{\mathrm{r}}}{M_{\mathrm{r}}}} \approx \frac{\frac{m_{\mathrm{Pt}}}{M_{\mathrm{Pt}}}}{\frac{m_{\mathrm{r}}}{M_{\mathrm{r}}}} \tag{4.4}$$

$$at\%_{\mathrm{Y}} = \frac{n_{\mathrm{Y}}}{n_{\mathrm{Pt}} + n_{\mathrm{Y}} + n_{\mathrm{r}}} = \frac{\frac{m_{\mathrm{Y}}}{M_{\mathrm{Y}}}}{\frac{m_{\mathrm{Pt}}}{M_{\mathrm{Pt}}} + \frac{m_{\mathrm{Y}}}{M_{\mathrm{Y}}} + \frac{m_{\mathrm{r}}}{M_{\mathrm{r}}}} \approx \frac{\frac{m_{\mathrm{Y}}}{M_{\mathrm{Y}}}}{\frac{m_{\mathrm{r}}}{M_{\mathrm{r}}}} \tag{4.5}$$

Combining the equations (4.4) and (4.5), the Pt:Y ratio can be calculated. The molecular weights of Pt and Y are taken from the NIST database [149].

$$\frac{at\%_{\mathrm{Pt}}}{at\%_{\mathrm{Y}}} = \frac{\frac{m_{\mathrm{Pt}}}{M_{\mathrm{Pt}}}}{\frac{m_{\mathrm{Y}}}{M_{\mathrm{Y}}}} = \frac{wt\%_{\mathrm{Pt}} \cdot M_{\mathrm{Y}}}{wt\%_{\mathrm{Y}} \cdot M_{\mathrm{Pt}}} = 3.82 \tag{4.6}$$

This means, the Pt:Y ratio in the IL is (3.82 ± 1.51). The large error arises from the low concentration of the species of interest in the mixture. Especially for Y, this leads to a high uncertainty of the measured weight percent. However, the final atomic ratio is close to the optimal value of 3. This shows that the target composition of Pt_3Y is preserved after sputtering in the liquid substrate in general.

To observe the NPs, a TEM grid of the sample was prepared (initially there were issues with grid preparation, so this is why some previous samples do not have images alongside). Figure 35 shows TEM images at different magnifications.

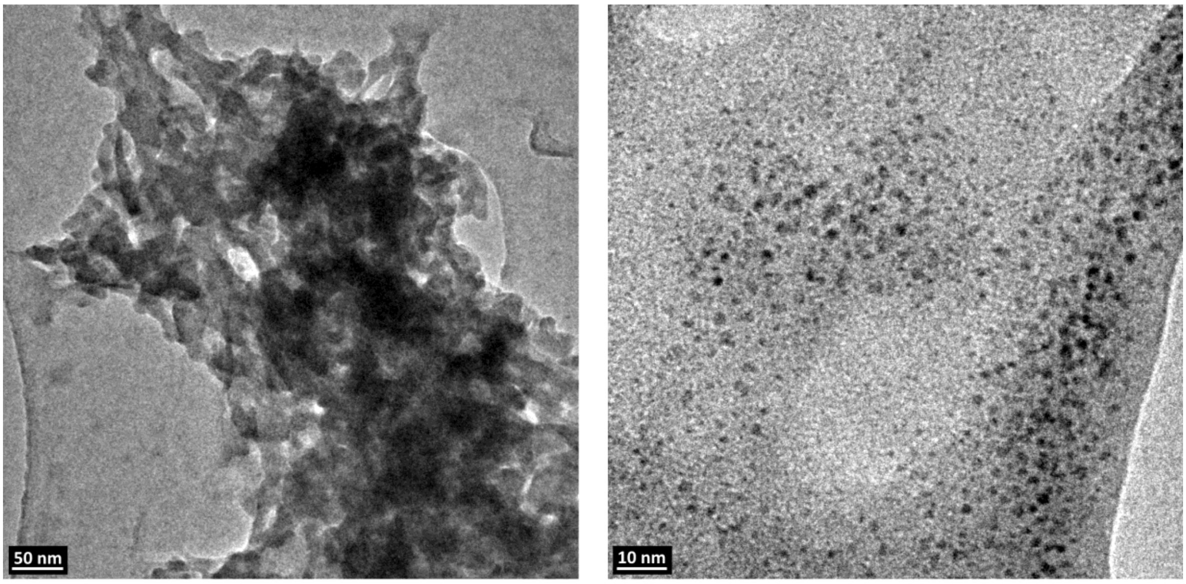

(a) (b)

Figure 35: TEM images of Pt_3Y sputtered onto [Emim] [OTf]: (a) Large aggregate structures at lower magnification; (b) NPs at higher magnification.

At lower magnifications, large aggregate structures of several hundreds of nanometers in diameter can be observed as shown in Figure 35(a). When zooming in, NPs of a few nanometers in diameter can be seen close to the large structures. This visualization of the NPs via TEM represents ultimate evidence for NPs being produced via sputtering onto liquid substrates using the applied setup. However, the aggregate structures constitute an unexpected feature, so they were examined further by EDX. The corresponding spectrum is depicted in Figure 36.

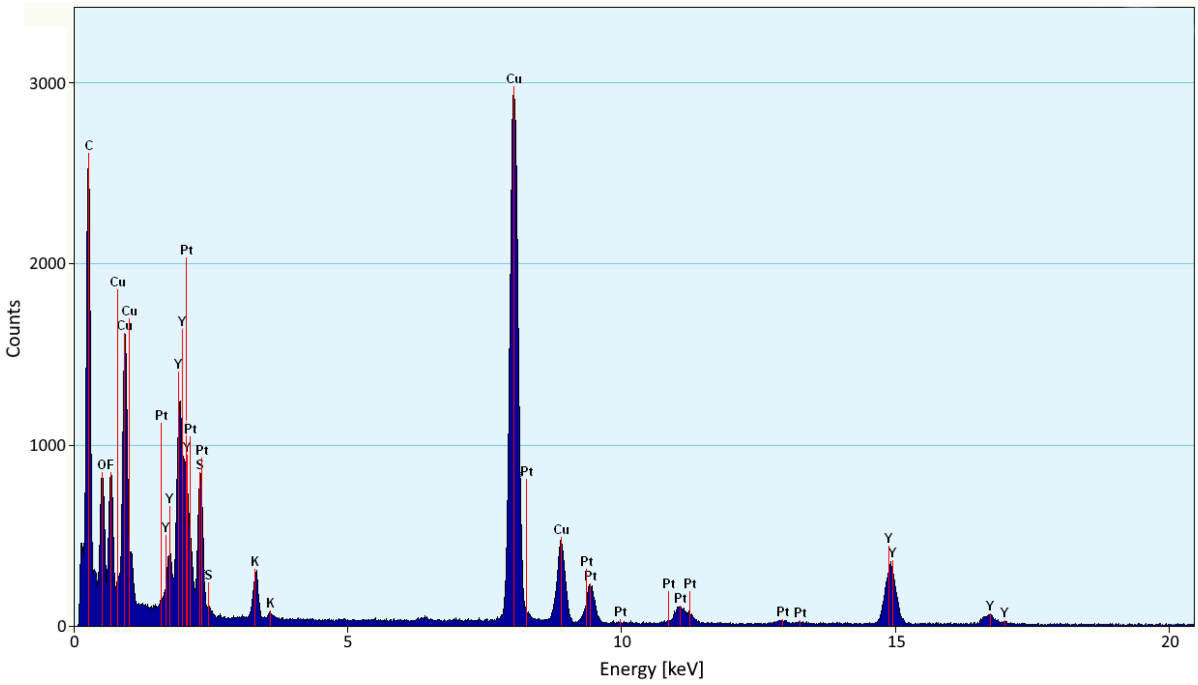

Figure 36: EDX spectrum of Pt_3Y sputtered onto [Emim] [OTf] (blue: raw intensity; red: theoretical peak positions).

Beside the grid materials, small amounts of the elements attributable to residual IL and a potassium contamination, Pt and Y peaks can be observed in the spectrum. The Pt:Y ratio is determined to vary between 1:3 and 1:4, meaning that the large aggregate structures contain substantially more Y than Pt. The two elements are separated and Y likely reacts with the IL to form some organometallic structures constituting the large aggregates. Pt rich NPs remain and are partially embedded in these Y-rich structures.

The reaction with Y limits the suitability of ILs as substrates for the fabrication of Pt_3Y NPs. To overcome the problems introduced by this type of substances, a liquid polymer substrate was tested, namely PEG 600. To ensure a good comparison to the [Emim] [OTf] sample, the same sputtering parameters were applied (P = 50; W_d = 8 cm; t = 3 x 300 s). A TEM image and the corresponding particle size distribution determined as explained in chapter 3.6.2 are illustrated in Figure 37. The histogram is fitted with a lognormal size distribution.

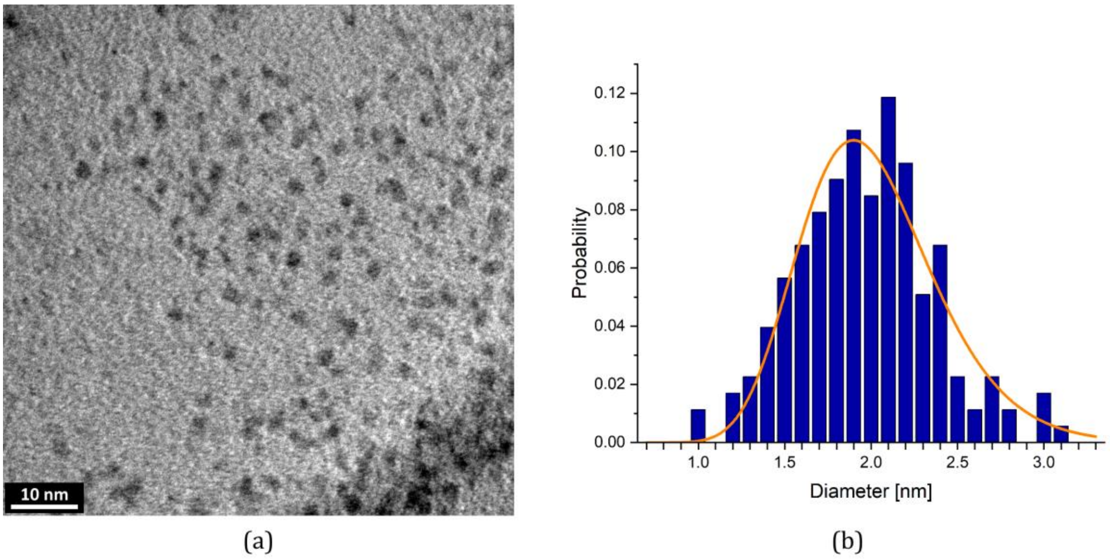

(a) (b)

Figure 37: TEM investigations of Pt_3Y sputtered onto PEG 600: (a) TEM image; (b) Particle size distribution (colums: raw data; curve: fitted lognormal distribution).

The particle size distribution in Figure 37(b) features a particle size of (2.0 ± 0.4) nm (the values represent the mean and the standard deviation). This reveals small NPs with a fairly narrow size distribution. Small NPs, but no large aggregate structures can be observed in the TEM images (compare Figure 37(a)), indicating that no reaction of the Y with the PEG takes place. This represents a favorable result and is reflected in the EDX spectrum given in Figure 38. The zoomed in area clearly exhibits Pt and Y peaks. Quantification by the software points out a Pt:Y ratio of (1.75 ± 1.15). The large error arises from the low Pt and Y content compared to the large amounts of detected C and Cu. However, considering this error, the obtained ratio lies in the range of the optimal value of 3. A NP composition close to Pt_3Y can consequently be assumed. This makes PEG 600 a very promising liquid substrate for sputtered Pt_3Y NPs.

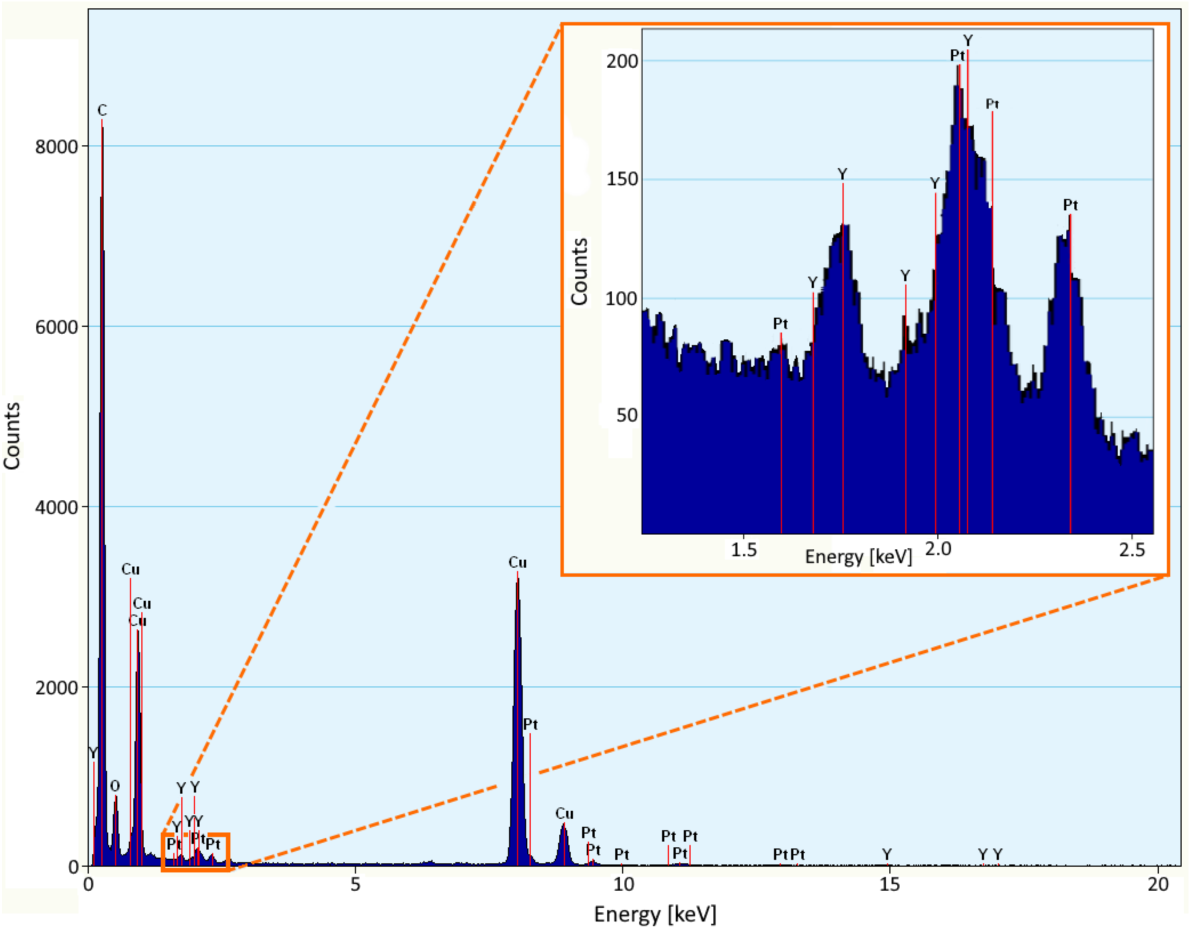

Figure 38: EDX spectrum of Pt_3Y sputtered onto PEG 600 (blue: raw intensity; red: theoretical peak positions).

The different interaction of [Emim] [OTf] and PEG 600 with Pt_3Y can be validated by an XPS study, which shows how the elements are bonded and helps to determine what the large structures are made of. Therefore, the XPS narrow-range spectra of the Y3d region presented in Figure 39 were recorded directly on the TEM grids.

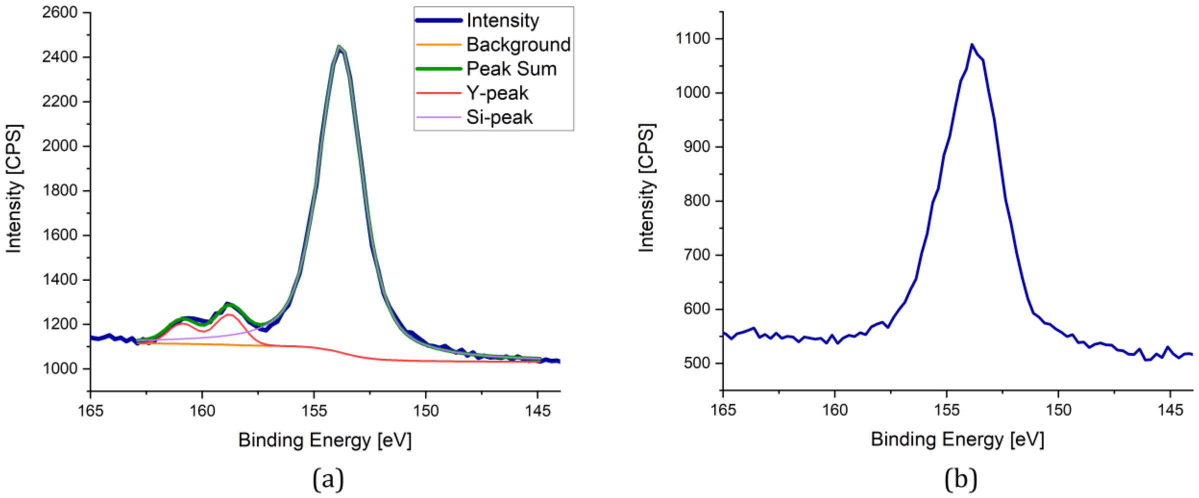

Figure 39: XPS Y3d narrow-range spectra of Pt_3Y sputtered onto different liquid substrates: (a) [Emim] [OTf]; (b) PEG 600.

Unfortunately, an intense silicon contamination is present on the grids. The XPS spectra collected directly in the sputtered IL+NPs droplet did not exhibit any Si peak (compare Figure 33), which is why this impurity is believed to originate from a step in the washing procedure for the TEM grids. However, the spectra for the two liquid substrates differ from each other. In the case of [Emim] [OTf] (compare Figure 39(a)) the Y3d doublet is found at a binding energy of 158.9 eV, which is shifted significantly compared to the metallic peak position. The value conforms to the binding energy found for the Y-F bond reported by Uwamino et al. [150]. Equally high binding energies are sometimes reported for the oxide [119], but in combination with the results from TEM and EDX, the observed peak shift affirms the suggestion of Y reacting with the IL. No shifted Y peak can be observed for PEG 600 as a liquid substrate (compare Figure 39(b)). With the EDX spectrum proving the existence of Y on the grid (compare Figure 38), the Y3d peak in the XPS spectrum is most likely covered by the comparatively huge Si peak. This is only possible with the Y3d peak at binding energies corresponding to the metallic form. Metallic Y being the desired chemical state for a catalytic application of the NPs, this shows once more that PEG 600 is a very favorable liquid substrate for the fabrication of Pt_3Y NPs.

4.3 Pt nanoparticle fabrication

Thus far, results have shown that NPs have been fabricated in ILs and PEG, although Y reacted with the ILs to form undesired irregular structures within the liquid. PEG 600 proved to be a suitable alternative for sputtered Pt_3Y NPs. For a better understanding and a quantitative analysis of the NPs' geometrical characteristics, pure Pt was used for the work shown in this chapter since this has been established in literature before and is hoped to reveal fundamental relationships with regard to the sputtering process.

4.3.1 Influence of the type of liquid substrate

To start with, four different liquid substrates were tested to reveal any substrate effects on the Pt NPs, namely [Emim] [OTf], [Dmim] [OTf], [Dmim] [Tf_2N] and PEG 600. Sputtering was performed at a power of P = 50 W and a target-to-substrate distance of W_d = 8 cm for a time of t = 3 x 300 s.

UV-Vis spectroscopy was applied to gain an impression of the potentially formed species and their basic geometrical characteristics. As a solvent, ultrapure water was used for [Emim] [OTf] and PEG 600, EtOH for [Dmim] [OTf] and [Dmim] [Tf_2N]. The spectra shown in Figure 40 were recorded in a mixture of 700 µl solvent with 15 µl of the sample, where corresponding mixtures of the pure liquid substrates with the solvents were used for the background line.

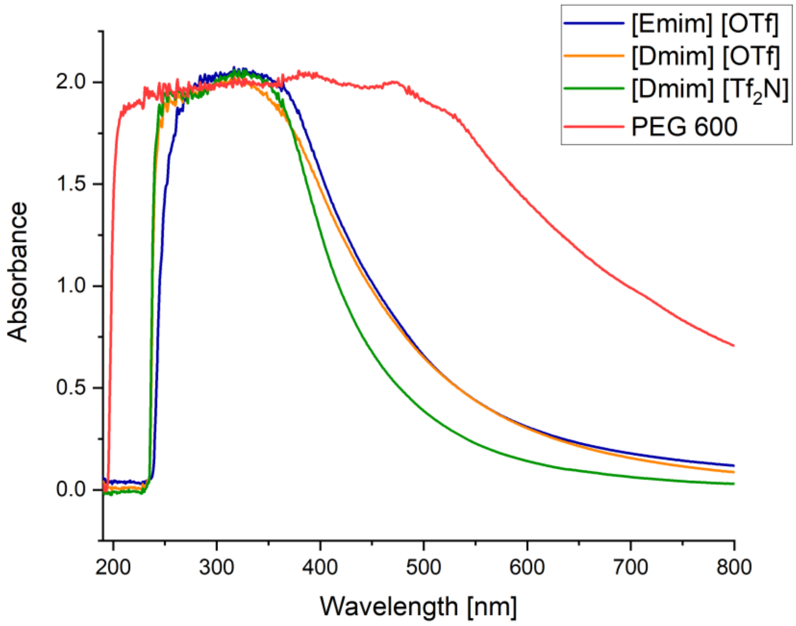

Figure 40: UV-Vis absorption spectra of Pt sputtered onto different liquid substrates.

First, the peak absorbance for all four tested substrates is basically the same, indicating an equivalent particle concentration. This is an unsurprising result given the unchanged sputtering parameters. Furthermore, the spectra of the three ILs appear very similar. They exhibit a single, well-defined peak, indicating the existence of spherical NPs [144]. The peak position is in accordance with previously reported values for Pt NPs [125, 146, 147]. The absorbance curve of the PEG 600 sample stands out to some extent. It exhibits a comparable peak position revealing the existence of Pt NPs, but the width of the peak is significantly larger than for the ILs. Whereas an increased absorbance at small wavelengths indicates the presence of smaller particles, higher absorbance at larger wavelengths corresponds to bigger particles [59]. This allows the conclusion that PEG 600 as a liquid substrate results in a slightly broadened particle size distribution compared to the ILs. This effect can be attributed to the lower stabilization capability of PEG 600, as introduced in chapter 2.4.2, which leads to less defined particle sizes. This is also reflected in the time dependent absorption spectra presented in Figure 41. Over time, the absorbance at longer wavelengths increases. According to the relationships given above, this implies a slow growth of the NPs due to imperfect stabilization by (water diluted) PEG 600.

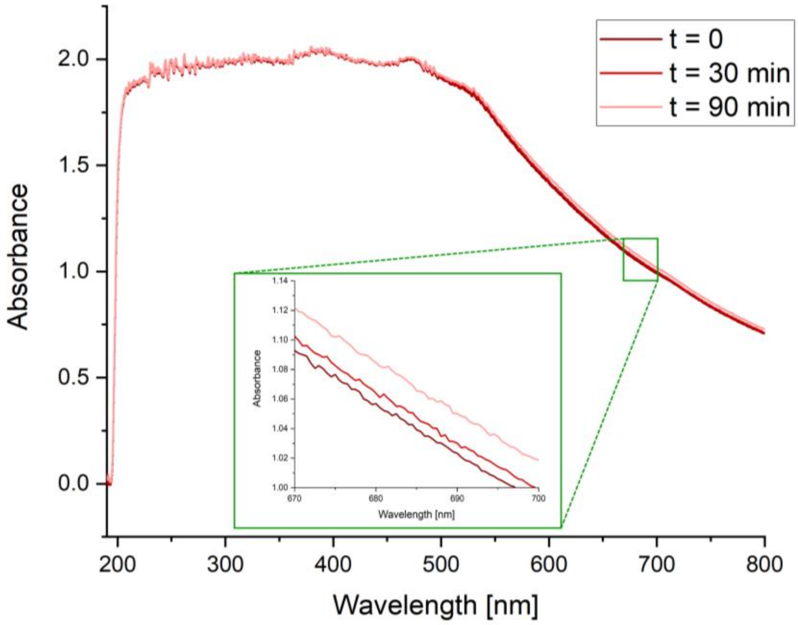

Figure 41: Time dependent UV-Vis absorption spectra of Pt sputtered onto PEG 600.

TEM investigations were performed to observe the NPs and determine the actual size distributions of the particles in the different samples. The existence of NPs in all four liquid substrates could be confirmed. The images of the [Emim] [OTf] sample as an example for an IL and the PEG sample are shown in Figure 42.

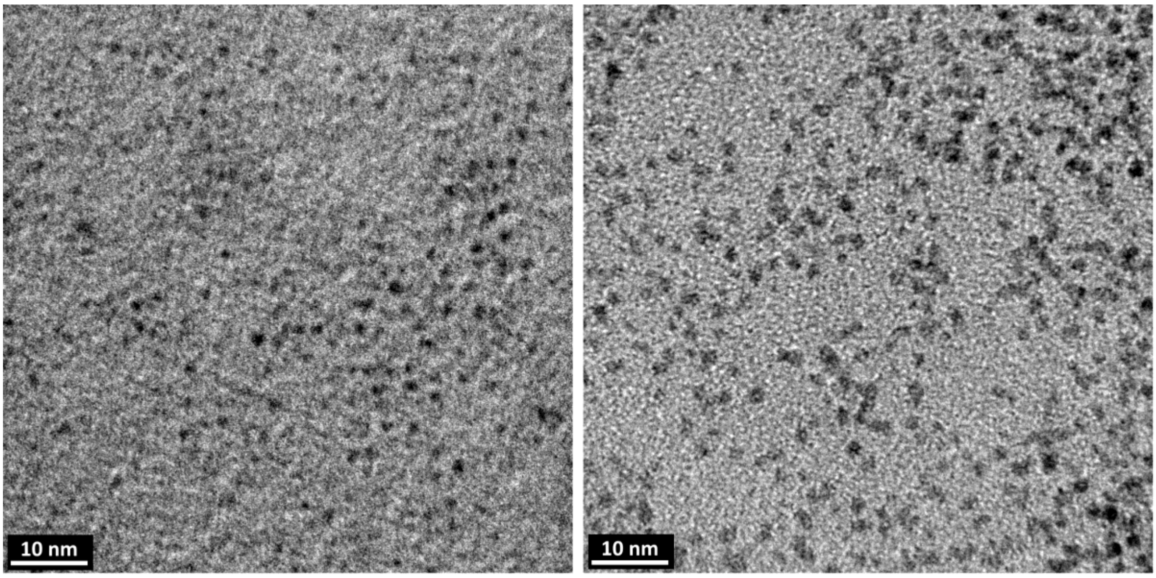

(a) (b)

Figure 42: TEM images of Pt sputtered onto different liquid substrates: (a) [Emim] [OTf]; (b) PEG 600.

Figure 43 presents the particle size distributions determined as explained in chapter 3.6.2 and fitted with lognormal distributions.

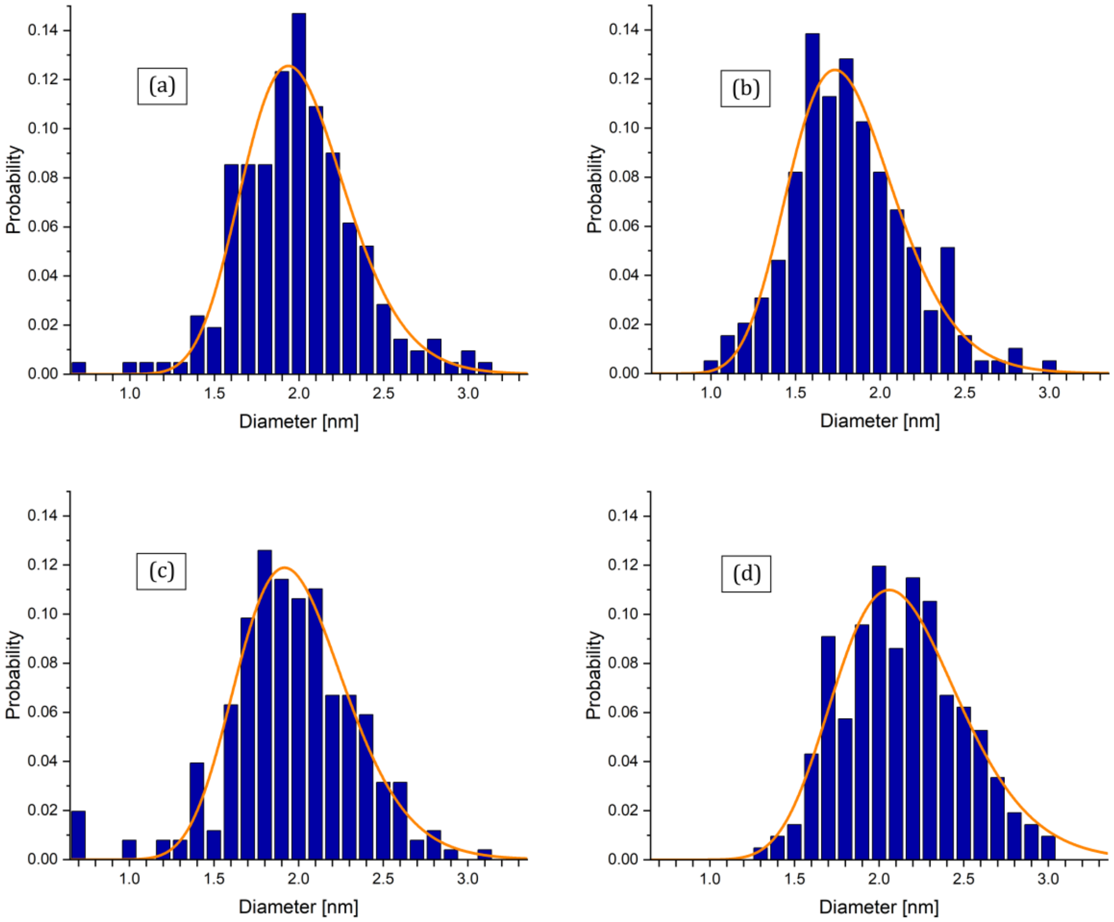

Figure 43: Particle size distributions of Pt sputtered onto different liquid substrates: (a) [Emim] [OTf]; (b) [Dmim] [OTf]; (c) [Dmim] [Tf_2N]; (d) PEG 600 (colums: raw data; curves: fitted lognormal distributions).

The distributions reveal similar geometrical properties of the particles for the different liquid substrates. All of them result in small particles with diameters of d = 1 – 4 nm, a mean particle size around 2 nm and narrow size distributions. An observable difference is the particles in PEG 600 exhibiting a slightly broader size distribution than the NPs in the ILs, which validates the conclusion drawn from the UV-Vis investigation. For a comparison of the four liquid substrates, the mean and the standard deviation of the particle size distributions from Figure 43 are given in Table 8 and plotted in Figure 45 (as diameter and error) together with the results from SAXS.

To receive more information on the NPs and the NP-liquid systems, SAXS was applied. The measurements were performed in the undiluted sputtered liquids+NPs in order to eliminate any effects from solvents. Due to the high absorption coefficients of the undiluted liquid substrates, each sample was measured for 5 h. Since very small particles were expected to appear, the MAXS setup was used. The pure liquid substrates served as the corresponding references. Figure 44(a)-(d) shows the scattering data as well as the generated fits for the four liquid substrates. Figure 44(e) summarizes the four fits after shifting them to the same background value of 0.001 cm^{-1} for the purpose of comparison.

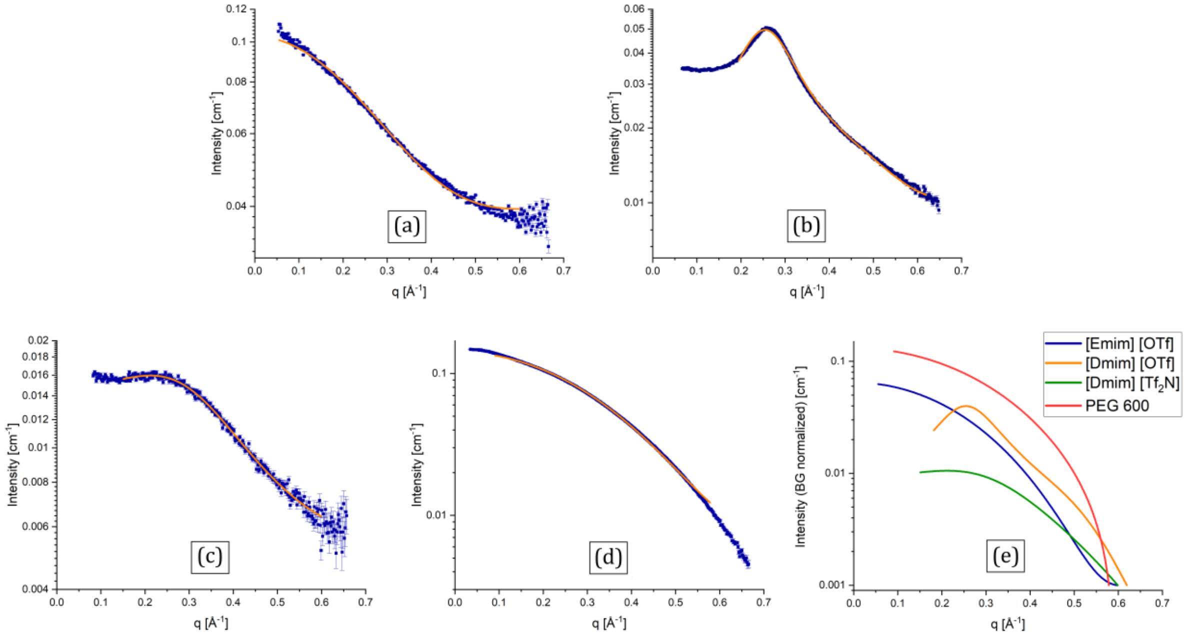

Figure 44: SAXS curves and fits of Pt sputtered onto different liquid substrates: (a) [Emim] [OTf]; (b) [Dmim] [OTf]; (c) [Dmim] [Tf$_2$N]; (d) PEG 600 (blue: raw data; orange fits); (e) comparison of background corrected fits.

A reasonable fit can be achieved with a spherical form factor for all four liquid substrates, which validates the spherical shape of the produced NPs. The ILs with the [Dmim] cation additionally require the implementation of a structure factor to modulate the peak in the scattering data. This can be retraced to strong interparticle repulsion, which typically leads to a lowered intensity at small q-values [110]. With the [Dmim] ILs possessing the same charge as the [Emim] IL, the enhanced particle repulsion for the [Dmim] ILs is attributed primarily to a strong steric stabilization by the long decyl chains. The peak position q_{peak} allows a calculation of the interparticle distance D_{p} via equation (4.7) [110].

$$D_{\mathrm{p}} = \frac{2 \cdot \pi}{q_{\mathrm{peak}}} \tag{4.7}$$

Here, this leads to:

$$D_{\mathrm{p,[Dmim][OTf]}} = \frac{2 \cdot \pi}{0.256\ \text{Å}^{-1}} = 24.54\ \text{Å}$$

$$D_{\mathrm{p,[Dmim][Tf_2N]}} = \frac{2 \cdot \pi}{0.221\ \text{Å}^{-1}} = 28.43\ \text{Å}$$

Taking the standard geometry of an alkyl chain (C-C bond length of $l = 1.54$ Å and angle of $\theta = 109.5°$ [151]) as a base, the decyl chain length a of the [Dmim] cation is $a = 9 \cdot \sin(\theta/2) \cdot l = 11.32$ Å. Two decyl chains repelling each other (compare Figure 9(b)) thus have nearly the length of the interparticle distances. The residual part of the interparticle distance can be supposed to be occupied by the imidazole part of the cation as well as the anion. The smaller [OTf] anion (compared to [Tf_2N]) justifies the smaller interparticle distance for [Dmim] [OTf]. These results indicate an effective steric stabilization by long alkyl chains of the cation. Hereby, it is likely that the anion coordinates directly to the NP and the cation with the alkyl chain forms the outer shell. This is an interesting suggestion since there have been some discussions and contradictory hypotheses on this topic in literature [80, 88, 152, 153].

Of course, the fitted SAXS curves can be used to determine the particle sizes. The results are presented together with the sizes obtained from the TEM analysis in Table 8 and Figure 45. The errors in the SAXS data represent the fitting errors given by the software.

Table 8: Particle sizes of Pt sputtered onto different liquid substrates.

Liquid substrate	***d* [nm] from TEM**	***d* [nm] from SAXS**
[Emim] [OTf]	2.01 ± 0.32	1.49 ± 0.01
[Dmim] [OTf]	1.82 ± 0.33	1.26 ± 0.01
[Dmim] [Tf_2N]	2.00 ± 0.34	1.16 ± 0.07
PEG 600	2.16 ± 0.39	1.24 ± 0.01

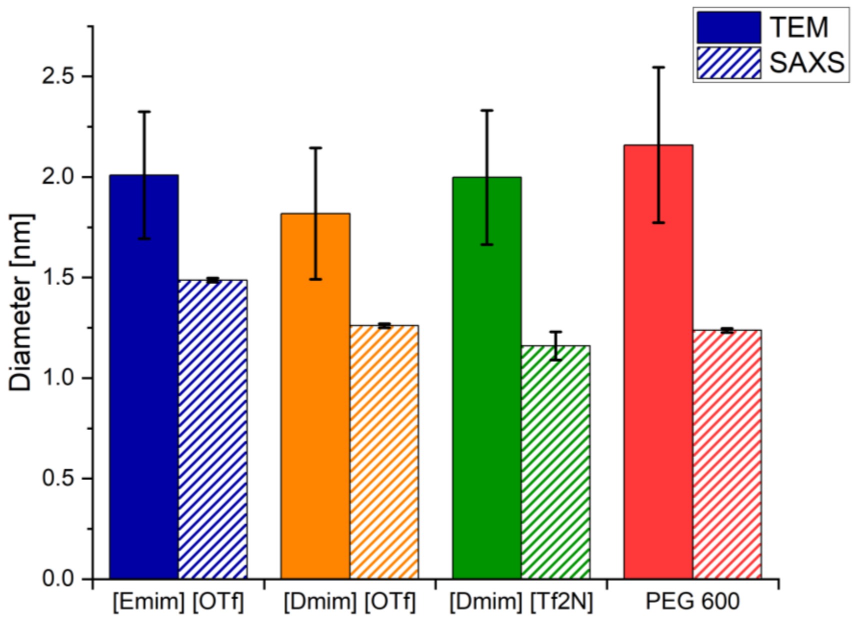

Figure 45: Particle sizes of Pt sputtered onto different liquid substrates.

It can be observed that SAXS systematically delivers somewhat smaller mean particle sizes than TEM. The accurate absolute values obtained from both methods should therefore always be handled with care. Difficulties in the correct and exact recognition of particle edges surely lead to uncertainties in the TEM data. The small errors for the SAXS data represent the small uncertainties for each single measurement point in the SAXS curves (due to the applied MAXS setup and long measurement times), but do not include errors made during the non-trivial data treatment and fitting procedure. The absolute differences of particle sizes in the different liquid substrates are very small. Furthermore, the trends of the particle size in dependence of the liquid substrate are not the same for the two measurement methods. For these reasons, the data is not believed to reveal any such trends. The results show that the liquid substrate does not exercise major control on the particle size within the tested liquids.

4.3.2 Post heat-treatment of the sputtered nanoparticles

A potential way to increase the size of the produced particles is the application of a post heat-treatment. The heat-treatment procedure specified in chapter 3.3 was applied immediately after sputtering at a power of P = 50 W for a time of t = 3 x 300 s at a target-to-substrate distance of W_d = 8 cm for the two liquid substrates [Emim] [OTf] and PEG 600.

UV-Vis absorption spectroscopy was applied to gain an impression of the influence of the post heat-treatment. To record the spectrum, 15 µl of the sample was mixed with 700 µl ultrapure water. A mixture of equivalent amounts of the pure IL with ultrapure water provided the baseline. The result for the [Emim] [OTf] sample is shown in Figure 46.

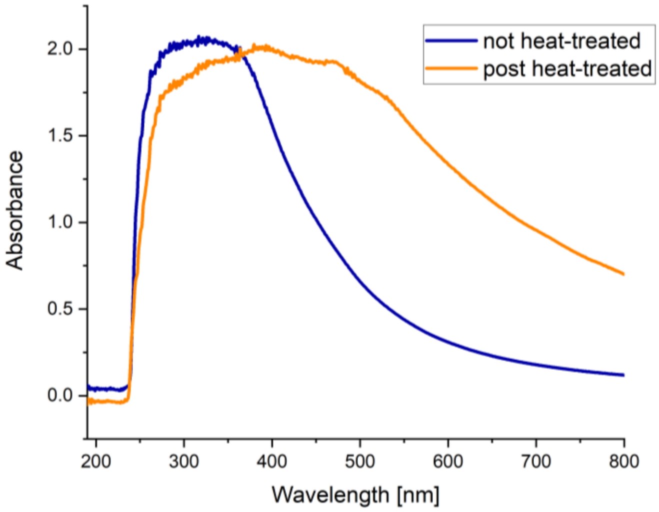

Figure 46: Effect of post heat-treatment on UV-Vis absorption spectrum of Pt sputtered onto [Emim] [OTf].

A broadening of the peak in the UV-Vis spectrum is introduced by the post heat-treatment and it is important to note that this broadening takes place only one-sided, leading to increased absorbance values at larger wavelengths, but not at shorter ones. This results in a shift of the peak position accompanying the broadening. In relation to the particles' properties, this implies a growth of the NPs during the heat-treatment. This growth does not occur uniformly, which leads to a broadening of the particle size distribution as indicated by the increased width of the UV-Vis peak.

The actual particle size distributions are constructed by an analysis of TEM images as explained in chapter 3.6.2 and fitted with lognormal distributions. They are plotted for the not heat-treated sample and the post heat-treated one for both tested liquid substrates in Figure 47 and verify the assumptions based on the UV-Vis results.

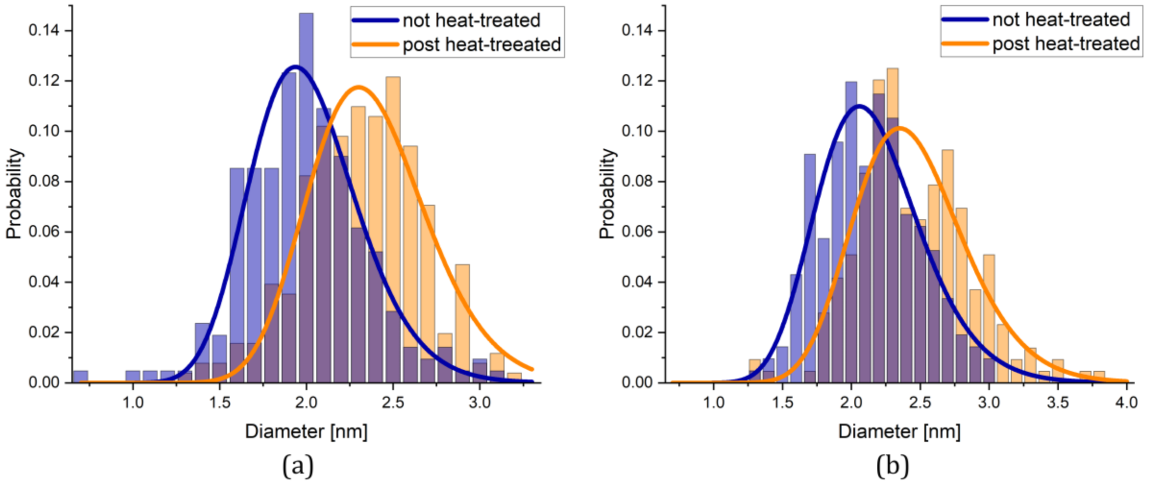

Figure 47: Effect of post heat-treatment on particle size distributions of Pt sputtered onto different liquid substrates: (a) [Emim] [OTf]; (b) PEG 600 (colums: raw data; curves: fitted lognormal distributions).

For both liquids, the post heat-treatment causes a particle growth and a broadening of the particle size distribution. These observations can be traced back to increased kinetics at elevated temperatures, which enables a faster diffusion of atoms, nuclei and particles through the liquid. This increases the collision frequency between those species. On the one hand, not all atoms might be immediately incorporated in NPs during sputtering. The particle growth during the heat-treatment could then be a result of the attachment of those atoms to existing NPs. On the other hand, coalescence of existing particles might induce particle growth. In any case, the post heat-treatment accelerates the occurring processes, which leads to the observable increase in particle size. Furthermore, a decreasing viscosity of the liquid with rising temperature has the same effect.

For a quantitative comparison between the two liquid substrates, SAXS was conducted since this method is believed to best clarify trends in the particle size. The measurements were recorded in the undiluted samples for an illumination time of 5 hours in the MAXS geometry. The pure liquid substrates served as the reference. Hereby, the references for the heat-treated samples were subjected to the same heat-treatment procedure in order to eliminate any (unlikely) effects of the heat-treatment on the liquid substrate. The SAXS data and the fitted curves are given in Figure 48. They are shifted to a common background of 0.01 cm^{-1} for the purpose of comparison.

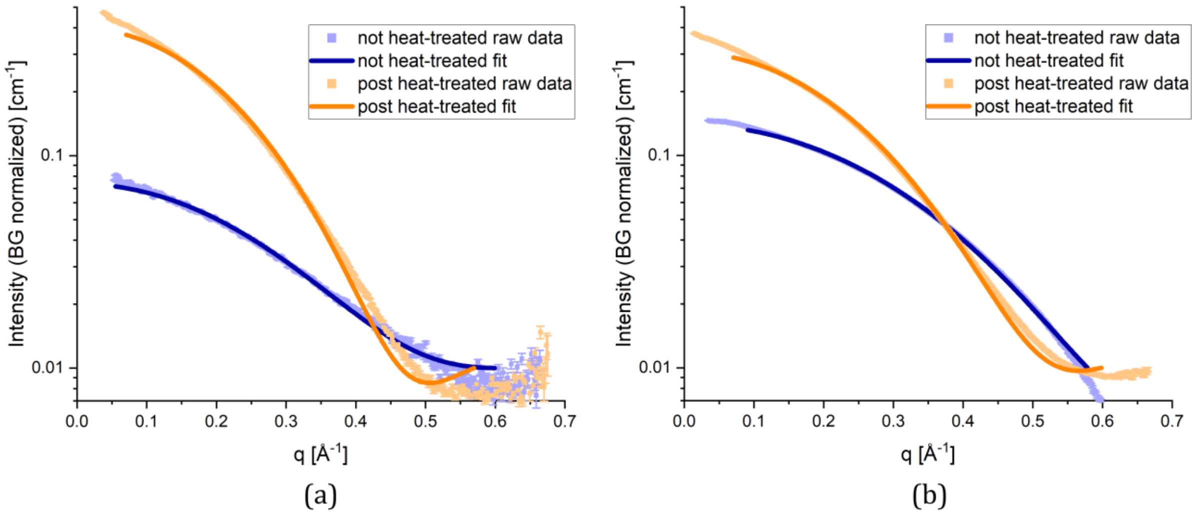

Figure 48: Effect of post heat-treatment on SAXS curves and fits of Pt sputtered onto different liquid substrates: (a) [Emim] [OTf]; (b) PEG 600.

The extracted particle sizes *d* are listed in Table 9. Again, the particle sizes obtained by SAXS are slightly smaller than the sizes revealed by the TEM analysis. However, the trends observed by TEM and SAXS analysis agree with each other. The errors in the temperature represent estimated uncertainties in the room- and heat-treatment temperature. The errors in the particle sizes provided by the software are partially even smaller than the specified 0.01 nm. As mentioned in the previous chapter, the final uncertainties including errors in the data treatment and fitting procedure are certainly larger. This justifies rounding up the errors to 0.01 nm at least.

Table 9: Influence of post heat-treatment on particle sizes determined by SAXS.

	$d_{\text{[Emim] [OTf]}}$ [nm]	$d_{\text{PEG 600}}$ [nm]
not heat-treated (298 ± 5) K	1.49 ± 0.01	1.24 ± 0.01
post heat-treated (463 ± 5) K	1.78 ± 0.01	1.59 ± 0.01

The diameters are plotted against the temperature in Figure 49 for illustrative reasons.

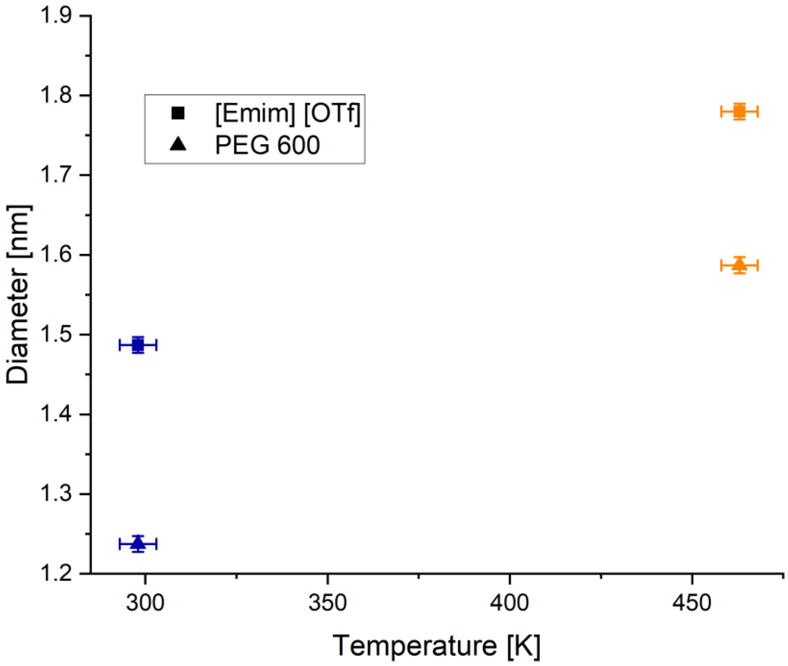

Figure 49: Effect of post heat-treatment on particle sizes of Pt sputtered onto different liquid substrates.

The relative increase of the particle size induced by the post heat-treatment is larger for the liquid polymer. With the diameters given in Table 9, a value of 19% can be calculated for [Emim] [OTf], whereas the particles in PEG 600 grow by 28%. The stronger influence of the post heat-treatment on the particles suspended in PEG 600 can be explained by the superior stabilization behavior of the IL. The latter isolates the NPs very efficiently once formed, which is why growth by collisions between different species is more unlikely. However, it should be kept in mind that the absolute differences in particle sizes are very small, which makes the quantitative analysis challenging. Therefore, more detailed research might be necessary to validate the described trends.

4.3.3 Influence of the sputtering power

Beside a post heat-treatment, the sputtering power has previously been shown to be an easily variable parameter in the sputtering process that may have an influence on the sputtered particle size (compare chapter 2.3.2). The issue has been approached by several groups who obtained partially contradicting results [61, 64, 67, 72, 77]. The relationship between sputtering power and particle size may even depend on the system, which justifies the importance of according investigations of individual systems that are believed to be of relevance. Here, this was performed for Pt sputtered onto PEG 600. At a target-to-substrate distance of W_d = 8 cm, samples were sputtered at a power of P = 20 W, P = 50 W and P = 65 W for a time of t = 3 x 300 s each.

Again, UV-Vis absorption spectra of the three batches were measured in mixtures of 700 µl ultrapure water with 15 µl of the sample. A mixture of corresponding amounts of ultrapure water with PEG 600 was used as the reference. The results are plotted in Figure 50.

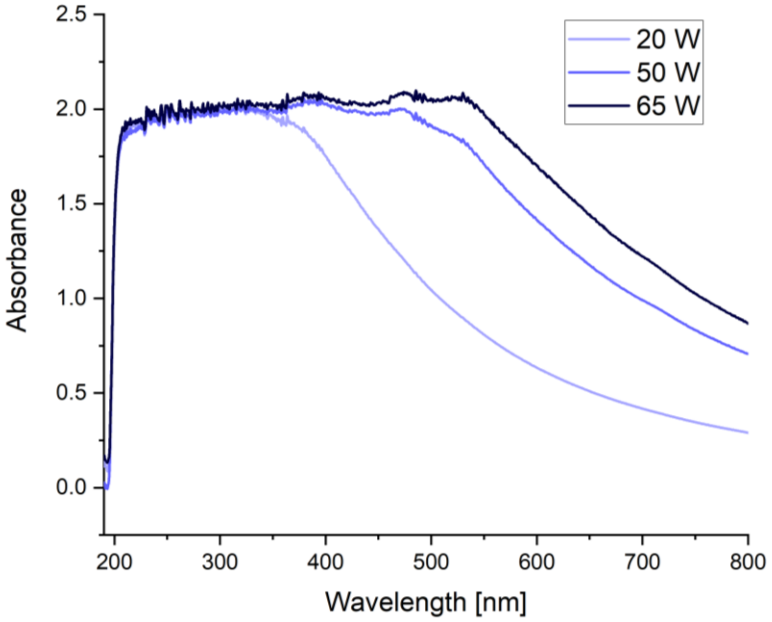

Figure 50: Effect of sputtering power on UV-Vis absorption spectrum of Pt sputtered onto PEG 600.

Clearly, the absorbance at higher wavelengths is increased by enhanced sputtering powers. As explained in earlier chapters, this corresponds to the existence of larger particles. The absorbance being unchanged in smaller wavelength ranges, this points out both an increased mean particle size and a broadened size distribution. The peak absorbance on the other hand appears not to be a function of the sputtering power, which implies the particle concentration to not depend on the power. This can be seen as an indication for the particles forming at the surface of the liquid substrate. According to equation (2.9), a higher sputtering power (expressed by a higher ion energy) increases the sputtering yield and thereby leads to a higher arrival rate of sputtered species at the liquid surface. In case the sputtered species directly penetrate the bulk liquid, this should primarily lead to an enhanced particle concentration in the comparatively large space the bulk liquid provides. If the sputtered species stay on the liquid surface for a certain time span, an increased arrival rate results in a drastically increased collision rate between the species at this surface. This results in coalescence processes of the sputtered species and enhanced NP sizes rather than an increased concentration as illustrated in Figure 51. From this point of view, the NP nucleation and growth taking place at the liquid surface seems to be much more likely.

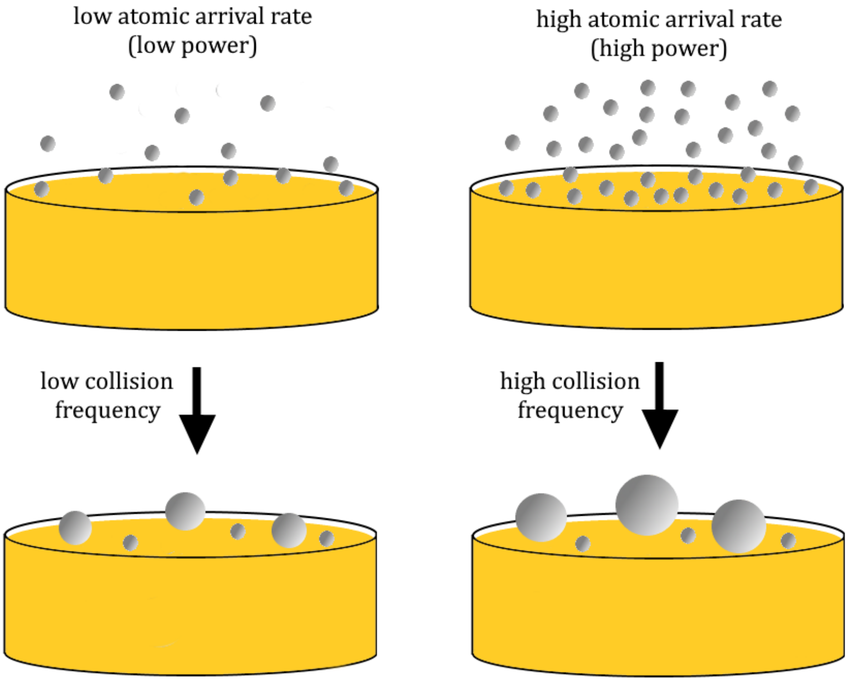

Figure 51: Particle growth at the liquid surface for different atomic arrival rates.

To determine the actual size distributions, TEM was applied and data analysis was performed as explained in chapter 3.6.2. The resulting distributions including lognormal fits are presented in Figure 52(a)-(c). Figure 52(d) shows the fits together in one diagram for comparison. The data confirms the trends already assumed from the UV-Vis spectra. Higher sputtering powers lead to larger particle sizes and broader size distributions.

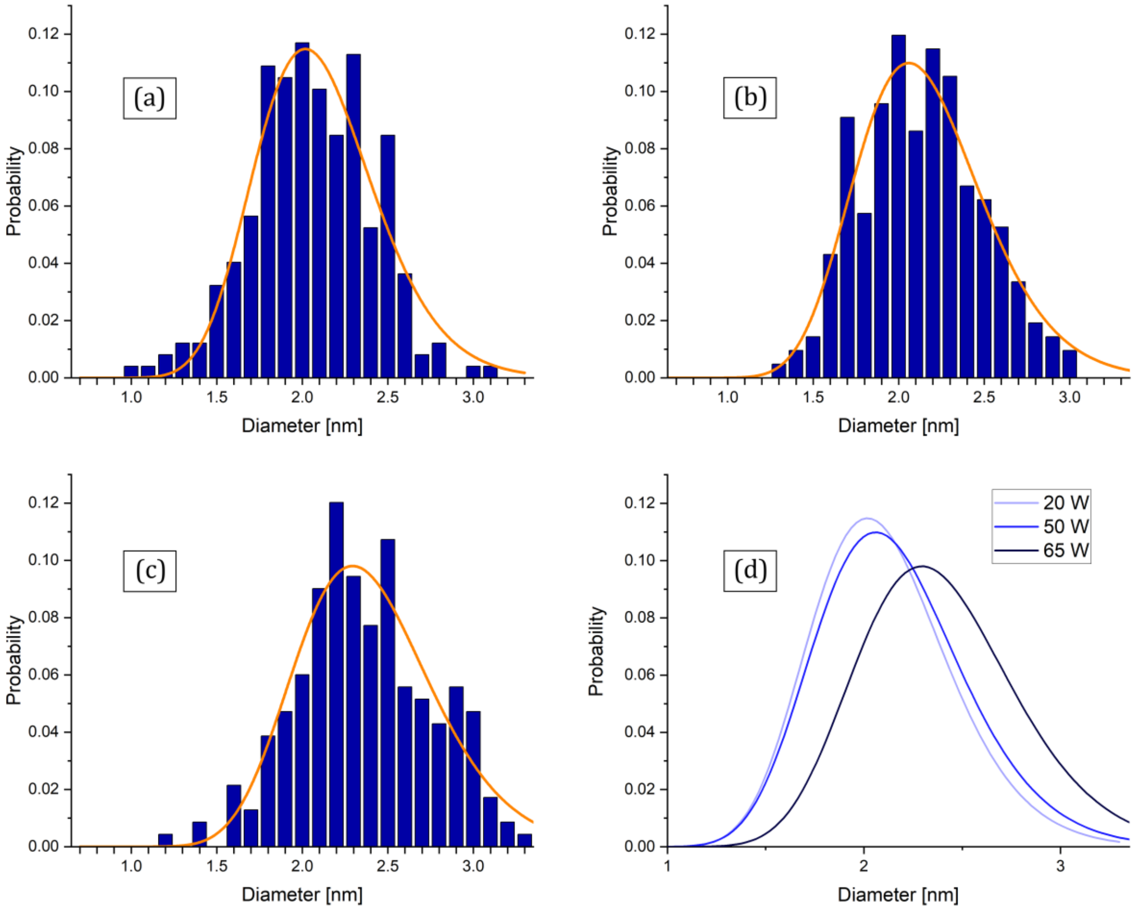

Figure 52: Effect of sputtering power on particle size distribution of Pt sputtered onto PEG 600: (a) *P* = 20 W; (b) *P* = 50 W; (c) *P* = 65 W (colums: raw data; curves: fitted lognormal distribution); (d) Comparison of fitted lognormal size distributions.

For a quantitative comparison between the different sputtering powers, a SAXS analysis was conducted. The measurements were executed in the undiluted sputtered PEG+NPs for a time of 5 hours each in the MAXS setup. Pure PEG 600 served as the reference. The SAXS data and the fitted curves for the different sputtering powers are shown in Figure 53(a). They are shifted to a common background of 0.01 cm^{-1} for the purpose of comparison. The curves clearly reflect the variations in particle size. Primarily the higher slope at high q-values indicates an increased particle size for enhanced sputtering powers.

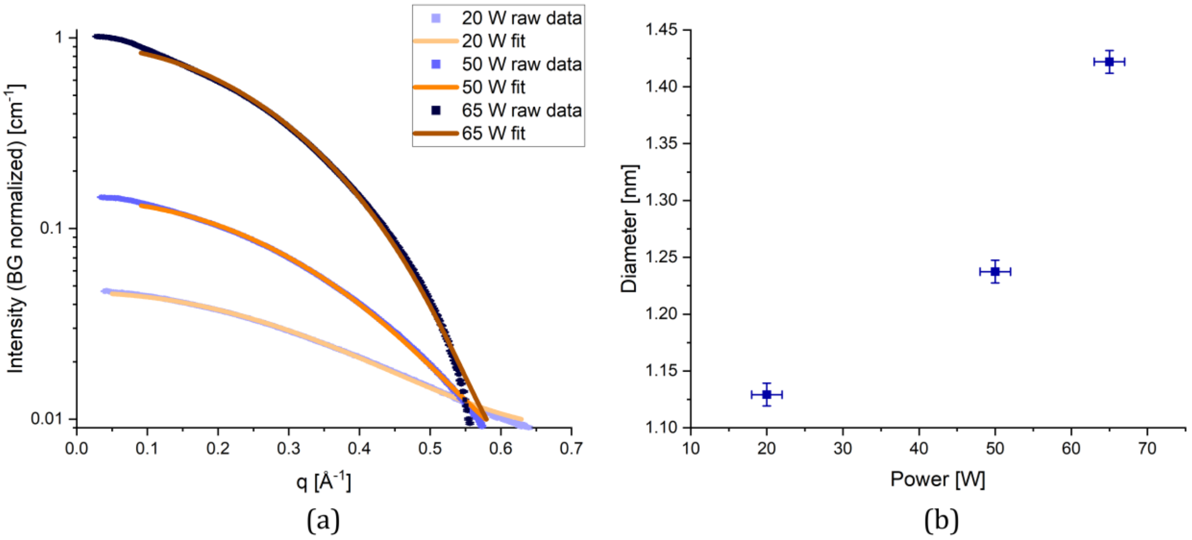

Figure 53: SAXS results of Pt sputtered onto PEG 600 at different sputtering powers: (a) Effect of sputtering power on SAXS curves and fits; (b) Effect of sputtering power on particle sizes.

From the fitted scattering data, the particle sizes d are extracted, listed in Table 10 and plotted in Figure 53(b). As in the previous chapter, the errors in the particle size are rounded up to 0.01 nm to account for errors made during the data treatment and fitting procedure. The uncertainties in the power reflect estimated fluctuations during the sputtering process.

Table 10: Effect of sputtering power on particle sizes determined by SAXS.

Power [W]	***d* [nm]**
20 ± 2	1.13 ± 0.01
50 ± 2	1.24 ± 0.01
65 ± 2	1.42 ± 0.01

Again, the particle sizes obtained by SAXS are slightly smaller than the ones revealed by a TEM analysis, but the trends agree with each other. The relative increase in particle size between 20 W and 65 W, as determined by SAXS, is 26%. Beside the increasing particle size with sputtering power, a stronger increase in size between 50 W and 65 W than between 20 W and 50 W is recognizable. A possible explanation of this behavior could be different contributions of discharge voltage U and current I to the power P, which are based on equation (4.8) [54].

$$P = U \cdot I \tag{4.8}$$

Unfortunately, the voltage and current could not be adjusted independently of each other with the used sputter coater. To still determine to what extent the voltage change and the current change contribute to the total power change, the following calculation is executed.

A change in power can be expressed as:

$$\partial P = \left.\frac{\partial P}{\partial U}\right|_{I} \cdot \partial U + \left.\frac{\partial P}{\partial I}\right|_{U} \cdot \partial I = I \cdot \partial U + U \cdot \partial I \tag{4.9}$$

For convenience, it is assumed that the total voltage change between two measuring points takes place at the constant average current I_a and that the total current change appears at the constant average voltage U_a:

$$\Delta P = \left.\frac{\partial P}{\partial U}\right|_{I_\mathrm{a}} \cdot \Delta U + \left.\frac{\partial P}{\partial I}\right|_{U_\mathrm{a}} \cdot \Delta I = \underbrace{I_\mathrm{a} \cdot \Delta U}_{\substack{\text{voltage}\\ \text{contribution}}} + \underbrace{U_\mathrm{a} \cdot \Delta I}_{\substack{\text{current}\\ \text{contribution}}} \tag{4.10}$$

The exact voltages, currents and powers at the three measuring points are listed in Table 11.

Table 11: Sputtering voltages and currents at different powers.

Measuring point	Voltage [V]	Current [A]
20 W	373	0.051
50 W	424	0.119
65 W	444	0.145

Between the measuring points at 20 W and 50 W the ratio between the current contribution and the voltage contribution to the total power change is

$$\frac{U_\mathrm{a} \cdot \Delta I}{I_\mathrm{a} \cdot \Delta U} = \frac{\frac{U_{20\mathrm{W}} + U_{50\mathrm{W}}}{2} \cdot (I_{50\mathrm{W}} - I_{20\mathrm{W}})}{\frac{I_{20\mathrm{W}} + I_{50\mathrm{W}}}{2} \cdot (U_{50\mathrm{W}} - U_{20\mathrm{W}})} = 6.25 \tag{4.11}$$

The equivalent calculation between the measuring points at 50 W and 65 W leads to

$$\frac{U_\mathrm{a} \cdot \Delta I}{I_\mathrm{a} \cdot \Delta U} = 4.27 \tag{4.12}$$

It can be concluded from the two ratios that the contribution of the voltage to the power change is larger between 50 W and 65 W than between 20 W and 50 W. The particle size increase is also greater in the interval between 50 W and 65 W, so discharge voltage could have a larger effect on the particle size than discharge current. Beside an increased arrival rate of sputtered species at the liquid surface, a higher voltage increases the kinetic energy of the sputtered species, which further increases the collision frequency and could account for the described behavior.

However, different voltage and current influences have been reported in literature in dependence of the used liquids, targets and sputtering conditions [61, 64, 67, 72, 77]. This points out that the here observed results should not be considered to hold universally, but are rather specific for the applied system. Further experiments should be carried out to validate the proposed relative influences of sputtering voltage and current.

4.4 Sputtered nanoparticle formation and growth process

So far, only the characteristics of the final particles have been investigated in this study. However, the formation process of the NPs is an interesting and relevant topic for the understanding of the overall method of sputtering onto liquid substrates to fabricate NPs.

As demonstrated in chapter 4.3.3, the effects of sputtering power on particle size and concentration represent an indication of a particle formation and growth mechanism at the surface of the liquid substrate. To review this assumption, the visual appearance of some liquid covered wafers is now examined in more detail. Figure 54 shows Pt_3Y-sputtered [Emim] [OTf] on the wafers for different sputtering times t and / or target-to-substrate distances W_d, but constant sputtering powers of P = 50 W.

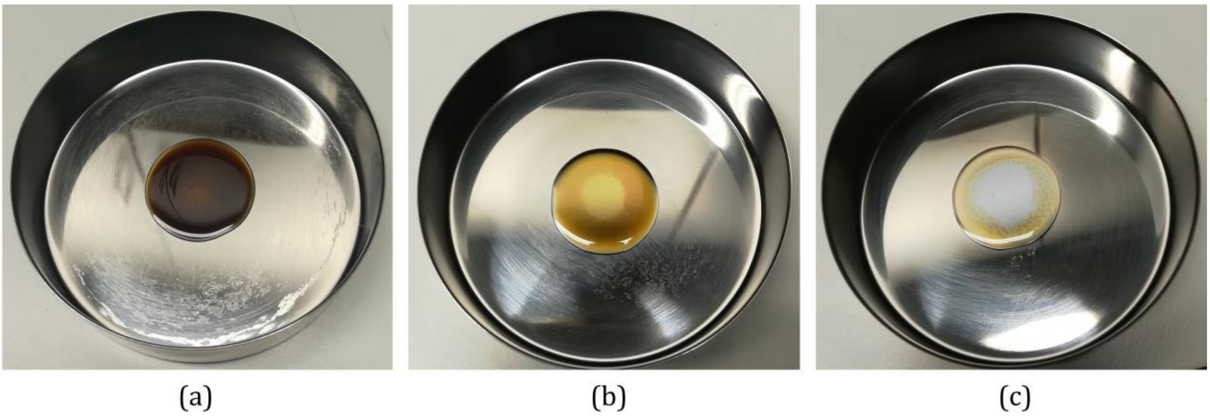
(a) (b) (c)

Figure 54: Visual appearance of sputtered [Emim] [OTf] on wafers: (a) t = 3 x 300 s, W_d = 8 cm; (b) t = 300 s, W_d = 8cm; (c) t = 30 s, W_d = 4 cm.

After a sputtering time of t = 3 x 300 s, the liquid substrate on the wafer shows a homogeneous dark brown color, as can be seen in Figure 54(a). The general origin of the color change compared to the not-sputtered colorless liquid is explained in chapter 4.1.1. Due to the long sputtering time as well as the breaks of 20 minutes after each 300 s cycle, the formed particles have enough time to distribute homogenously throughout the bulk substrate - irrespectively of where they are formed initially. This explains the uniform color and allows no conclusion on the growth process of the NPs. However, at shorter sputtering times the situation changes, as can be observed in Figure 54(b) and (c). In general, the color of the liquid is less dark owing to the lower concentration of particles (compare chapter 4.2.2). More interesting here is the development of kind of a ring structure on the liquid substrate. On the outer part of the wafer, an area of clearly darker color is recognizable, whereas the liquid in the center of the wafer exhibits a less intense coloring. This can certainly be traced back to a higher particle concentration towards the edge of the wafer. Exactly the same observation could be made for other liquid substrates used in this thesis.

At first view, this might look like an angular distribution effect of the sputtering process. However, sputtering theory predicts a cosine law as a first approximation to the emission distribution [54, 148]. This should lead to the highest particle concentration in the center of the wafer. If still an angular effect was the reason for the formation of the ring structure on the wafer, a shorter target-to-substrate distance should lead to a smaller radius r of this ring. This is illustrated in Figure 55, where the grey marked lines of the highest sputtering emission would characterize the ring structure. These considerations are in contradiction to the experimental observations. The radius of the ring at a sputtering distance of 4 cm (Figure 54(c)) is substantially larger than at 8 cm (Figure 54(b)).

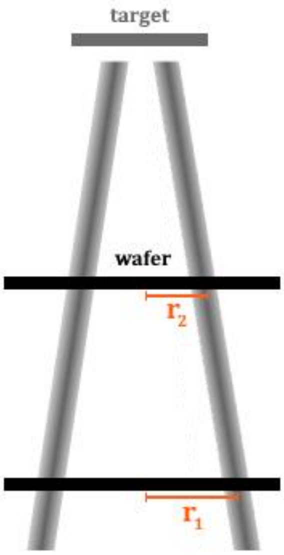

Figure 55: Effect of potential angular effect on ring structure on wafer (grey: lines of highest sputtering emission; r_1: radius of the ring structure at a large sputtering distance; r_2: radius of the ring structure at a short sputtering distance).

For the given reason, it is not believed that an angular effect leads to the ring structure on the wafer. To approach the given observations, the so-called Cheerios effect is considered. The name of this phenomenon originates from the aggregation behavior of cereal floating on milk [154]. This can be explained by a combination of gravity and surface tension [155] and is illustrated in Figure 56 by means of two particles of a higher density than the liquid.

Despite their higher density, the two particles float on the surface due to the surface tension of the liquid. Thereby, a meniscus is formed in the vicinity of the particles. Due to the existence of an adjacent second particle, the meniscus around each of the particles is not symmetric, but is lowered somewhat in the direction of the second particle. The two menisci interact, which leads to the two particles moving towards each other. [154–156]

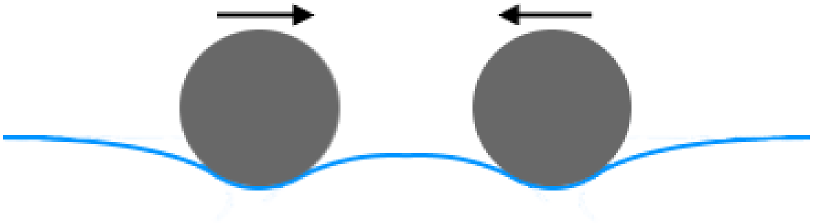

Figure 56: Cheerios effect on two floating particles.

This behavior can be transferred to the situation on the liquid substrate. For an individual particle, it does not matter if the second meniscus is generated by another particle or by any other effect. The bare liquid on the wafer forms a drop and thereby has a convex meniscus itself. These circumstances and a more detailed explanation of the Cheerios effect in this case are demonstrated in Figure 57.

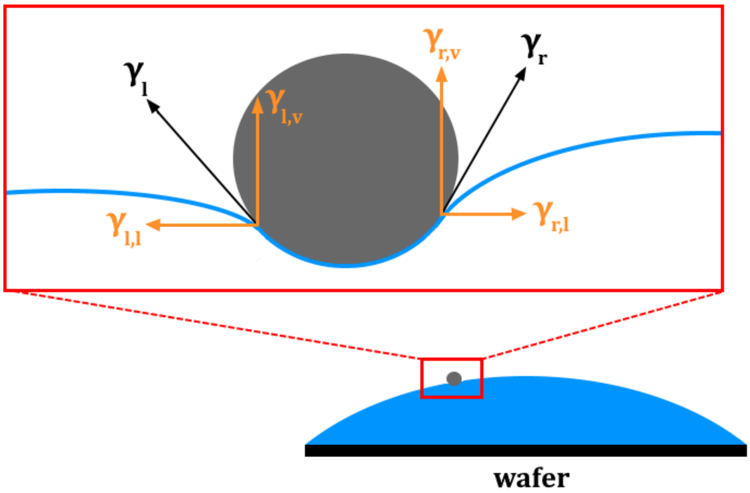

Figure 57: Cheerios effect on floating particle on liquid substrate drop.

Again, the particle is held at the surface by the surface tension γ, which can be illustrated by the two constituents of the surface tension γ_l and γ_r at the left and the right triple phase contact points in the two-dimensional picture. The surface tension on both sides of the particle can be divided into a vertical ($\gamma_{l,v}$ and $\gamma_{r,v}$) and a lateral ($\gamma_{l,l}$ and $\gamma_{r,l}$) component. In case of a symmetric meniscus, the lateral component of the surface tension cancels out and only the vertical component counteracting the gravity remains. However, the meniscus introduced by the drop shape of the liquid leads to an asymmetry in the local meniscus around the particle. Thereby, the liquid contact angles on the different sides of the particle are not equivalent and the total lateral component of the surface tension varies from zero ($\gamma_{l,l} + \gamma_{r,l} \neq 0$). As a result, a net lateral force drags the particle to the left in this example - in general to the side of the wafer. The same result can be obtained by an energetic elucidation. The particle of a higher density moves to the lowest point of the liquid surface to reduce the potential energy of the whole system. [154–156]

This mechanism can readily explain the ring structure observed in the liquid substrates after sputtering. However, it only takes effect if the sputtered species stay at the liquid surface for some time and the NPs form there instead of inside the bulk liquid. Only then can the interaction of the menisci of the particles and the liquid drop lead to a drag of the particles to the side of the wafer. If the sputtered species directly penetrated the bulk, where the nucleation would take place, the Cheerios effect could not operate and the particle concentration would be homogenous directly after sputtering. As mentioned in chapter 2.3.1, there has been some controversy on the exact particle formation mechanism. The results presented in this chapter provide strong evidence, that the NP nucleation and growth mechanism follows path (b) or a combination of (a) and (b) with respect to Figure 8.

4.5 Electrochemical characterization of sputtered nanoparticles

The main part of this work was dedicated to the investigation of the sputtering process onto liquid substrates itself as well as the geometrical characterization and modulation of the produced NPs. This was important to understand the basic relationships for a successful operation of this NP fabrication process. However, as described in earlier chapters, the final use-oriented objective is the application of the NPs as catalysts for the ORR in fuel cells. For this reason, this chapter will finalize the study with an electrochemical characterization of the NPs. It is hereby intended to examine whether the fabricated particles are transferrable from the liquid substrate to a catalyst ink and exhibit a catalytic activity there.

Sputtering of Pt and Pt_3Y onto PEG 600 was performed at a power of P = 50 W and a target-to-substrate distance of W_d = 8 cm for a time of t = 3 x 300 s. Catalyst inks of both Pt and Pt_3Y NPs in PEG were prepared and immobilized onto a GCE as explained in chapter 3.4. To gain a first impression of the quality of the formed catalyst films, SEM images were taken and are shown in Figure 58.

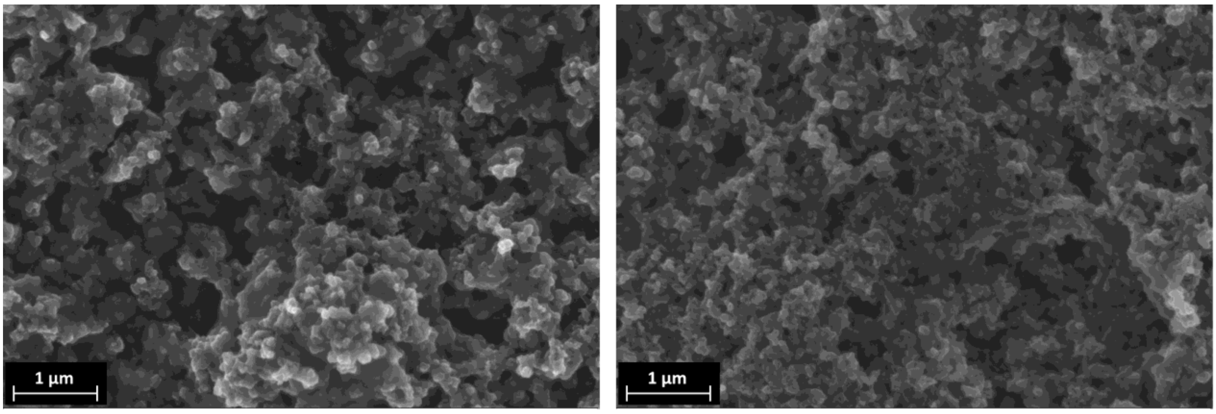

(a) (b)

Figure 58: SEM images of carbon supported catalyst on GCE. (a) Pt; (b) Pt_3Y.

The structure of the carbon supported catalyst layers look very similar for both the Pt and the Pt_3Y sample. They exhibit a macroscopically smooth surface without significant cracks or other failures, which is an important property of a good film for the electrochemical characterization [28]. Furthermore, as shown in Figure 58, a porous structure of the carbon support can be observed, which enables a large surface area and allows contact of the reactive species with the catalyst particles. In fact, the porosity is an important feature of the triple-phase boundary as introduced in chapter 2.1.

Individual NPs cannot be observed in the SEM images, which is why voltammetric measurements are necessary to reveal if they are present or not. The CVs of both samples measured in 1 M $HClO_4$ in Ar-atmosphere with a scan rate of 10 mV/s are presented in Figure 59. The data is corrected for the solution resistance and shifted to the RHE. The electrochemically active surface area (ECSA) necessary to normalize the currents is calculated from the hydrogen adsorption peak, where the non-faradaic region is used as the baseline. Figure 62 in Appendix C illustrates the areas under the curves considered for the hydrogen adsorption. The ECSA is calculated according to equation (4.13) with surface coverage θ, scan rate v, current I and voltage U [28, 157, 158].

$$\mathrm{ECSA} = \frac{1}{\theta} \cdot \frac{\frac{1}{v} \cdot \int_{\mathrm{H-ads}} I \, \mathrm{d}U}{210 \, \frac{\mu\mathrm{C}}{\mathrm{cm}^2}} \tag{4.13}$$

The applied value for the surface coverage is $\theta = 0.77$ [158]. The actual calculation is given in Appendix C. The current densities are obtained by dividing the current values by the ECSA.

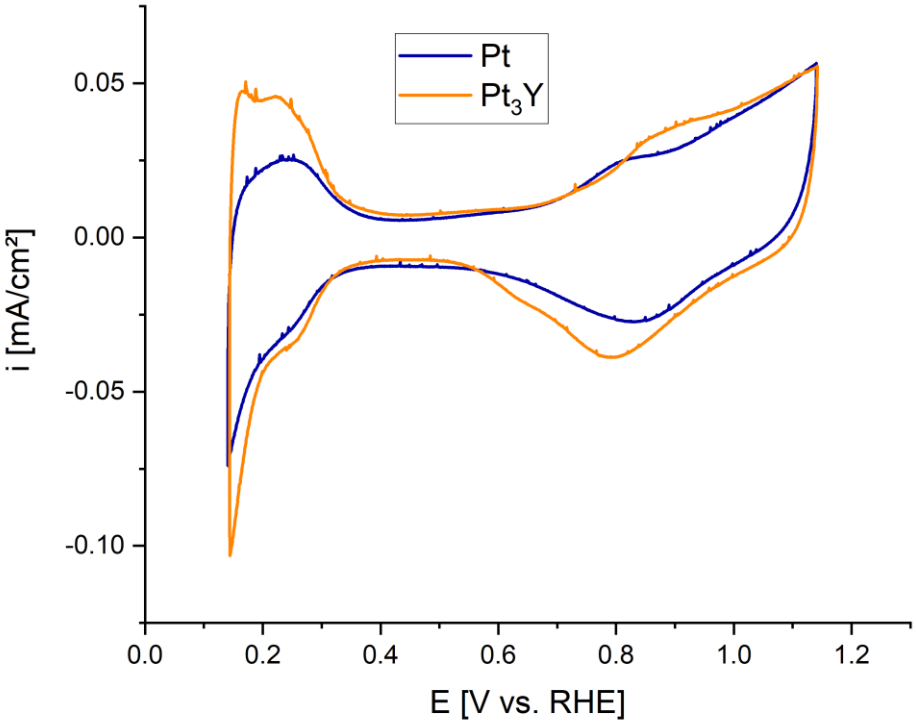

Figure 59: CVs of carbon supported catalysts on GCE.

The CVs given in in Figure 59 exhibit the typical characteristics of Pt catalysts in terms of shape and peak positions (compare chapter 2.1.1). In particular, they qualitatively appear very similar to the CV obtained by Torimoto et al. [99] (to be found in their supplementary information), whose ink formulation was taken as a base for the recipe used in this thesis. Pt and Pt_3Y respectively being the only ink ingredient coming into consideration to lead to those peaks, these results prove the successful transfer of the NPs from the liquid substrate to the ink and the electrode. This is very important since it represents evidence for the capability of the fabricated NPs to be immobilized in a catalyst structure, which is of practical use.

To gain an impression of the ORR activity of the produced catalyst inks, the potential was swept with a scan rate of 10 mV/s and the working electrode was rotated with 1600 rpm in the oxygen saturated electrolyte. The resulting curves after correction for the solution resistance and shifting to the RHE are given in Figure 60.

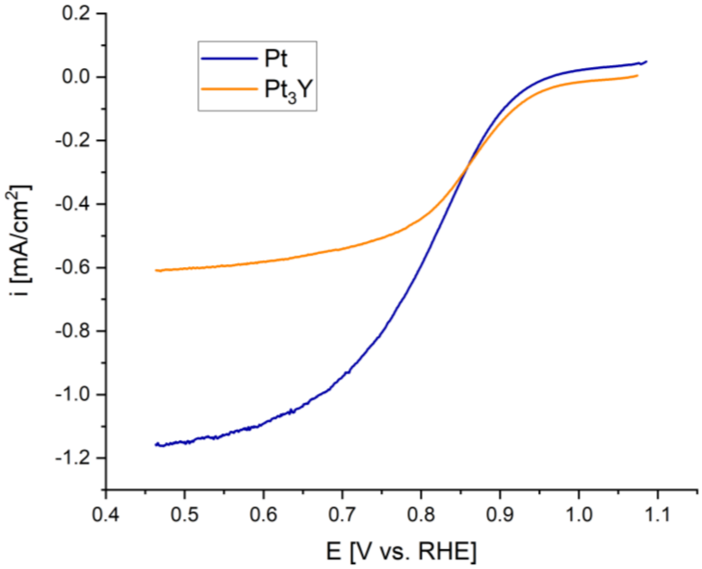

Figure 60: ORR polarization curves of carbon supported catalysts on GCE.

For both catalysts, the current ascribable to the ORR can be observed. The NPs can hence not only be transferred to the electrode, but they are also able to catalyze the ORR and thus fulfil their function. The catalytic activity at 0.9 V expressed by the kinetic current density i_k can be calculated with equation (4.14) based on the ORR polarization curves, where i_lim is the limiting current density of the plateau at low potentials (diffusion limiting current) and $i_{0.9}$ is the current density at 0.9 V [28]. This relationship follows directly from the Koutecký-Levich equation [159].

$$i_\mathrm{k} = \frac{i_\mathrm{lim} \cdot i_{0.9}}{i_\mathrm{lim} - i_{0.9}} \tag{4.14}$$

The values of i_lim and $i_{0.9}$ as well as their errors are estimated from the plots in Figure 60:

$$\begin{aligned} i_\mathrm{lim,Pt} &= (-1.18 \pm 0.03)\,\frac{\mathrm{mA}}{\mathrm{cm}^2} & \qquad i_{\mathrm{lim,Pt_3Y}} &= (-0.62 \pm 0.03)\,\frac{\mathrm{mA}}{\mathrm{cm}^2} \\ i_\mathrm{0.9,Pt} &= (-0.11 \pm 0.01)\,\frac{\mathrm{mA}}{\mathrm{cm}^2} & \qquad i_{\mathrm{0.9,Pt_3Y}} &= (-0.15 \pm 0.01)\,\frac{\mathrm{mA}}{\mathrm{cm}^2} \end{aligned}$$

Using equation (4.14), the catalytic activity at 0.9 V for the Pt and Pt_3Y NPs can be calculated (the absolute values of the current densities are inserted into the equation in order to obtain positive values for the catalytic activities):

$$i_\mathrm{k,Pt} = (0.12 \pm 0.02)\,\frac{\mathrm{mA}}{\mathrm{cm}^2}$$
$$i_{\mathrm{k,Pt_3Y}} = (0.20 \pm 0.02)\,\frac{\mathrm{mA}}{\mathrm{cm}^2}$$

The errors of the values do not include the determination of the ECSA, which can in fact lead to comparatively large uncertainties. This follows from the method of hydrogen adsorption relying on several assumptions, which may not all be completely valid [160]. The fundamental idea of the technique is, that the charge per surface area transferred to the metal by hydrogen adsorption is a known constant. In reality, this quantity depends on different factors such as the surface coverage and crystal orientation for example [160]. Also, uncomplete charge transfer processes to the metal as well as the hydrogen adsorption overlapping with hydrogen evolution can cause errors in the calculation [160]. Finally, surface changes upon adsorption and a dependence of the peak position and heights on the used electrolyte might lead to uncertainties in the determined surface area [160]. Nevertheless, the method is frequently applied to calculate the ECSA [160].

It is difficult to compare the here obtained values of the electrocatalytic activities to values reported in literature mainly due to the mentioned uncertainties in the ECSA. Furthermore, the activities strongly depend on the applied scan rate and rotation speed. However, they lie in the range of commercial pure Pt NPs [161], which certainly illustrates the practical applicability of the fabricated NPs. This proves the technique of sputtering onto liquid substrates to be a very interesting approach for the fabrication of nanoparticulate ORR catalysts.

For Pt_3Y NPs prepared by gas aggregation, catalytic activities of up to 14 mA/cm^2 have been measured by Hernandez-Fernandez et al. [12], which is much higher than the value reported in this work. On the one hand, this is doubtless a result of a non-optimized ink-formulation. The achievable catalytic activity is extremely sensitive on the ratio between carbon, catalyst NPs and Nafion [162]. For instance, a too high Nafion content can hinder the mass transport, whereas insufficient Nafion causes difficulties in proton conductivity [162]. Furthermore, unsatisfactory washing of the NPs may lead to residual PEG in the final ink, which can exhibit detrimental effects. Also, the rather low scan rate of 10 mV/s enhances impurity effects degrading the catalytic activity [28]. On the other hand, the here produced Pt_3Y NPs are much smaller than the gas-aggregated ones exhibiting the highest catalytic activity (8 – 9 nm) [12]. For the small NPs in this work, there is most likely an excessive removal of Y and the alloy core is too small to lead to a considerable strain effect. However, even for those small NPs produced here, the measured catalytic activity for Pt_3Y is enhanced by a factor of 1.67 compared to the pure Pt NPs. The idea of alloying Pt with Y to improve the ORR activity can thus be confirmed. At small particle sizes of roughly 4 nm, the catalytic activity of the gas-aggregated NPs decreased to a value close to 1 mA/cm^2 [12]. This shows that the NPs produced by sputtering onto liquid substrates may result in considerably enhanced activities as well, once their size can be increased. Altogether, these results are highly promising and can serve as a good starting point for further research and optimizations.

5 Conclusion

This thesis aimed to shed light on the method of sputtering onto liquid substrates to form Pt and Pt_3Y NPs. For this purpose, the particles' geometrical characteristics were investigated considering different parameters in the sputtering process. Additionally, the electrochemical properties of the particles with regard to the ORR catalysis were a subject of interest due to the potential application in fuel cells.

It could be shown that it is generally possible to form NPs of diameters in the range of 1 – 4 nm by sputtering onto different liquid substrates. Hereby, ILs were shown to be unsuitable for Pt_3Y deposition as they react with the Y to form undesired, irregular structures inside the liquid. In contrast, PEG proved to be a suitable substrate for the formation of Pt_3Y NPs, not reacting with Y and resulting in a dispersion of the NPs, even though it generally provided slightly reduced stabilization properties compared to ILs.

The fabrication of Pt NPs was less sensitive to the liquid substrate and was successfully conducted in different imidazolium-based ILs beside PEG. The IL type had a minor influence on the particle size and no significant trends with anion or cation properties could be observed. However, PEG resulted in a somewhat broader particle size distribution compared to the ILs, owing to the absent electrostatic stabilization mechanism. For ILs containing the [Dmim] cation, peaks in the SAXS scattering data implying strong repulsive interactions between the particles could be observed. A more detailed investigation of the peak positions provided indications on an effective steric stabilization via the decyl chains in an outer cationic layer around the NPs.

Table 12 provides a summary of which applied liquid substrates turned out to be suitable (✔) and unsuitable (✖) for the formation of NPs.

Table 12: Summary of liquid substrates used for Pt and Pt_3Y. *NPs could be observed alongside large yttrium structures indicating a reaction of Y with the IL.

	Pt	**Pt_3Y**
[Emim] [OTf]	✔	✔/✖*
[Emim] [Tf_2N]	-	✖
[Emim] [FAP]	-	✖
[Dmim] [OTf]	✔	-
[Dmim] [Tf_2N]	✔	✖
PEG 600	✔	✔

A post heat-treatment of the particle suspensions at 165 °C immediately after sputtering was applied and resulted in an increased particle size by 19% in [Emim] [OTf] and by 28%

in PEG 600. This effect was ascribed to enhanced kinetics and reduced liquid viscosities at elevated temperatures. The different extent of the post heat-treatment effect between the IL and the liquid polymer reflected the diverging stabilization abilities. As another possibility to tune the particle size, a variation of the sputtering power was applied. Higher sputtering powers led to increased collision frequencies of sputtered species and consequently to particle sizes in PEG increased by 26% between 20 W and 65 W. Hereby, the discharge voltage appeared to have a stronger influence than the discharge current. The NP concentration on the contrary was not changed significantly by enhanced sputtering powers, which suggested a particle formation and growth at the surface of the liquid substrate. This could be confirmed by an examination of the visual appearance of the sputtered wafers. The liquid covering the wafers exhibited a ring-like feature for short sputtering times, which could be understood by means of the Cheerios effect making the sputtered species at the liquid surface moving to the edge of the wafer.

Finally, Pt and Pt_3Y NPs in PEG were electrochemically characterized after a transfer of the NPs to a catalyst ink composed of Vulcan carbon, Nafion and the catalytic particles. Both Pt and Pt_3Y showed characteristic peaks in the CV, proving the successful immobilization of the NPs on the electrode surface. In terms of the catalytic activity towards the ORR, RDE experiments revealed an enhancement factor of 1.67 of Pt_3Y compared to pure Pt NPs. This confirmed the favorable effect of alloying Pt with RE metals. The absolute measured catalytic activities were found to lie in the range of commercially available Pt NPs, but did not reach the high performance of modern state-of-the-art catalysts.

These results provide strong motivation for further research on this topic. So far, the thesis proved the capability of sputtering onto liquid substrates to form catalytically active NPs with Pt as a base material. Regarding an application for the ORR catalysis in PEM fuel cells, especially the particles prepared by sputtering Pt_3Y onto PEG are highly promising. However, several challenges still need to be faced to put them into practical use. The composition and crystal structure of the individual particles need to be elucidated in more detail to clarify what exactly they are made of. High resolution TEM could be a suitable method to approach this issue. Another main question to be answered is certainly how to effectively increase the particle size of Pt_3Y NPs to enhance the strain effect. Furthermore, efforts need to be made to optimize the ink formulation and thereby enable as efficient catalytic processes as possible. If this succeeds, the method of sputtering Pt_3Y onto liquid substrates may represent a realistic approach for the commercial and effective production of nanoparticulate fuel cell catalysts.

6 References

[1] K. Raiser, H. Naims, and T. Bruhn, "Corporatization of the climate? Innovation, intellectual property rights, and patents for climate change mitigation," *Energy Research & Social Science*, vol. 27, pp. 1–8, 2017, doi: 10.1016/j.erss.2017.01.020.

[2] J. L. Moan and Z. A. Smith, *Energy use worldwide: A reference handbook*. Santa Barbara, Calif.: ABC-CLIO, 2007. [Online]. Available: http://www.netlibrary.com/urlapi.asp?action=summary&v=1&bookid=198574

[3] D. Gielen, F. Boshell, D. Saygin, M. D. Bazilian, N. Wagner, and R. Gorini, "The role of renewable energy in the global energy transformation," *Energy Strategy Reviews*, vol. 24, pp. 38–50, 2019, doi: 10.1016/j.esr.2019.01.006.

[4] S. Srinivasan, *Fuel cells: From fundamentals to applications*. New York: Springer, 2006. Accessed: Feb. 9 2020.

[5] J. Zhang, *PEM Fuel Cell Electrocatalysts and Catalyst Layers*. London: Springer London, 2008. Accessed: Feb. 9 2020.

[6] F. Barbir, "Transition to renewable energy systems with hydrogen as an energy carrier☆," *Energy*, vol. 34, no. 3, pp. 308–312, 2009, doi: 10.1016/j.energy.2008.07.007.

[7] S. J. Peighambardoust, S. Rowshanzamir, and M. Amjadi, "Review of the proton exchange membranes for fuel cell applications," *International Journal of Hydrogen Energy*, vol. 35, no. 17, pp. 9349–9384, 2010, doi: 10.1016/j.ijhydene.2010.05.017.

[8] J. M. Andújar and F. Segura, "Fuel cells: History and updating. A walk along two centuries," *Renewable and Sustainable Energy Reviews*, vol. 13, no. 9, pp. 2309–2322, 2009, doi: 10.1016/j.rser.2009.03.015.

[9] W. Xing, G. Yin, and J. Zhang, Eds., *Rotating electrode methods and oxygen reduction electrocatalysts*. Amsterdam: Elsevier, 2014.

[10] M. Escudero-Escribano *et al.,* "Tuning the activity of Pt alloy electrocatalysts by means of the lanthanide contraction," *Science (New York, N.Y.)*, vol. 352, no. 6281, pp. 73–76, 2016, doi: 10.1126/science.aad8892.

[11] K. I. Ozoemena and S. Chen, *Nanomaterials for Fuel Cell Catalysis*. Cham: Springer International Publishing, 2016. Accessed: Feb. 9 2020.

[12] P. Hernandez-Fernandez *et al.,* "Mass-selected nanoparticles of PtxY as model catalysts for oxygen electroreduction," *Nature chemistry*, vol. 6, no. 8, pp. 732–738, 2014, doi: 10.1038/nchem.2001.

[13] M. Escudero-Escribano, K. D. Jensen, and A. W. Jensen, "Recent advances in bimetallic electrocatalysts for oxygen reduction: design principles, structure-function relations and active phase elucidation," *Current Opinion in Electrochemistry*, vol. 8, pp. 135–146, 2018, doi: 10.1016/j.coelec.2018.04.013.

[14] N. Lindahl *et al.,* "High Specific and Mass Activity for the Oxygen Reduction Reaction for Thin Film Catalysts of Sputtered Pt 3 Y," *Adv. Mater. Interfaces*, vol. 4, no. 13, p. 1700311, 2017, doi: 10.1002/admi.201700311.

[15] R. P. O'Hayre, S.-W. Cha, W. G. Colella, and F. B. Prinz, *Fuel cell fundamentals*. Hoboken New Jersey: John Wiley & Sons Inc, 2016. Accessed: Feb. 22 2020.

[16] M. Schalenbach, T. Hoefner, P. Paciok, M. Carmo, W. Lueke, and D. Stolten, "Gas Permeation through Nafion. Part 1: Measurements," *J. Phys. Chem. C*, vol. 119, no. 45, pp. 25145–25155, 2015, doi: 10.1021/acs.jpcc.5b04155.

[17] J. Töpler and J. Lehmann, *Hydrogen and Fuel Cell*. Berlin, Heidelberg: Springer Berlin Heidelberg, 2016. Accessed: Feb. 9 2020. [Online]. Available: https://iolitec.de/sites/iolitec.de/files/2017-05/TDS%20IL-0029_UP%20BMIM%20BTA.pdf

[18] J. K. Nørskov *et al.,* "Origin of the Overpotential for Oxygen Reduction at a Fuel-Cell Cathode," *J. Phys. Chem. B*, vol. 108, no. 46, pp. 17886–17892, 2004, doi: 10.1021/jp047349j.

[19] I. E. L. Stephens, A. S. Bondarenko, U. Grønbjerg, J. Rossmeisl, and I. Chorkendorff, "Understanding the electrocatalysis of oxygen reduction on platinum and its alloys," *Energy Environ. Sci.*, vol. 5, no. 5, p. 6744, 2012, doi: 10.1039/c2ee03590a.

[20] J. de Paula and P. W. Atkins, *Physical chemistry,* 9th ed. New York: W.H. Freeman and Company, 2010.

[21] EG & G Services, Science Applications International Corporation, *Fuel Cell Handbook (Sixth Edition)*: DIANE Publishing, 2000.

[22] H. Ariza, A. Correcher, C. Sánchez, Á. Pérez-Navarro, and E. García, "Thermal and Electrical Parameter Identification of a Proton Exchange Membrane Fuel Cell Using Genetic Algorithm," *Energies*, vol. 11, no. 8, p. 2099, 2018, doi: 10.3390/en11082099.

[23] S. A. Vilekar and R. Datta, "The effect of hydrogen crossover on open-circuit voltage in polymer electrolyte membrane fuel cells," *Journal of Power Sources*, vol. 195, no. 8, pp. 2241–2247, 2010, doi: 10.1016/j.jpowsour.2009.10.023.

[24] X. Ren *et al.,* "Current progress of Pt and Pt-based electrocatalysts used for fuel cells," *Sustainable Energy Fuels*, vol. 4, no. 1, pp. 15–30, 2020, doi: 10.1039/C9SE00460B.

[25] D. Astruc, *Nanoparticles and catalysis*. Weinheim: Wiley-VCH, 2008. [Online]. Available: http://search.ebscohost.com/login.aspx?direct=true&scope=site&db=nlebk&db=nlabk&AN=518559

[26] E. Zamburlini, K. D. Jensen, I. E.L. Stephens, I. Chorkendorff, and M. Escudero-Escribano, "Benchmarking Pt and Pt-lanthanide sputtered thin films for oxygen electroreduction: fabrication and rotating disk electrode measurements," *Electrochimica Acta*, vol. 247, pp. 708–721, 2017, doi: 10.1016/j.electacta.2017.06.146.

[27] Y. Zhang *et al.,* "Study of the degradation mechanisms of carbon-supported platinum fuel cells catalyst via different accelerated stress test," *Journal of Power Sources*, vol. 273, pp. 62–69, 2015, doi: 10.1016/j.jpowsour.2014.09.012.

[28] Y. Garsany, O. A. Baturina, K. E. Swider-Lyons, and S. S. Kocha, "Experimental methods for quantifying the activity of platinum electrocatalysts for the oxygen reduction reaction," *Analytical chemistry*, vol. 82, no. 15, pp. 6321–6328, 2010, doi: 10.1021/ac100306c.

[29] E. M. Hudak, J. T. Mortimer, and H. B. Martin, "Platinum for neural stimulation: voltammetry considerations," *Journal of neural engineering*, vol. 7, no. 2, p. 26005, 2010, doi: 10.1088/1741-2560/7/2/026005.

[30] W. Xia, A. Mahmood, Z. Liang, R. Zou, and S. Guo, "Earth-Abundant Nanomaterials for Oxygen Reduction," *Angewandte Chemie (International ed. in English)*, vol. 55, no. 8, pp. 2650–2676, 2016, doi: 10.1002/anie.201504830.

[31] A. Velázquez-Palenzuela *et al.,* "The enhanced activity of mass-selected Pt Gd nanoparticles for oxygen electroreduction," *Journal of Catalysis*, vol. 328, pp. 297–307, 2015, doi: 10.1016/j.jcat.2014.12.012.

[32] J. Greeley *et al.,* "Alloys of platinum and early transition metals as oxygen reduction electrocatalysts," *Nature chemistry*, vol. 1, no. 7, pp. 552–556, 2009, doi: 10.1038/nchem.367.

[33] F. Li, S. Bashir, and J. L. Liu, Eds., *Nanostructured Materials for Next-Generation Energy Storage and Conversion: Fuel Cells*. Berlin, Heidelberg: Springer Berlin Heidelberg, 2018. [Online]. Available: http://dx.doi.org/10.1007/978-3-662-56364-9

[34] W. Gao, D. Wen, J. C. Ho, and Y. Qu, "Incorporation of rare earth elements with transition metal–based materials for electrocatalysis: a review for recent progress," *Materials Today Chemistry*, vol. 12, pp. 266–281, 2019, doi: 10.1016/j.mtchem.2019.02.002.

[35] M. Luo and S. Guo, "Strain-controlled electrocatalysis on multimetallic nanomaterials," *Nat Rev Mater*, vol. 2, no. 11, p. 877, 2017, doi: 10.1038/natrevmats.2017.59.

[36] C. Kim, F. Dionigi, V. Beermann, X. Wang, T. Möller, and P. Strasser, "Alloy Nanocatalysts for the Electrochemical Oxygen Reduction (ORR) and the Direct Electrochemical Carbon Dioxide Reduction Reaction (CO2 RR)," *Advanced materials (Deerfield Beach, Fla.)*, vol. 31, no. 31, e1805617, 2019, doi: 10.1002/adma.201805617.

[37] Y. Hu, J. O. Jensen, L. N. Cleemann, B. A. Brandes, and Q. Li, "Synthesis of Pt-Rare Earth Metal Nanoalloys," *Journal of the American Chemical Society*, vol. 142, no. 2, pp. 953–961, 2020, doi: 10.1021/jacs.9b10813.

[38] P. Liu and J. K. Nørskov, "Ligand and ensemble effects in adsorption on alloy surfaces," *Phys. Chem. Chem. Phys.*, vol. 3, no. 17, pp. 3814–3818, 2001, doi: 10.1039/b103525h.

[39] G. Ertl, *Handbook of heterogeneous catalysis,* 2nd ed. Weinheim, Chichester: Wiley-VCH, 2008. [Online]. Available: http://onlinelibrary.wiley.com/book/10.1002/9783527610044

[40] R. Brown *et al.,* "Unraveling the Surface Chemistry and Structure in Highly Active Sputtered Pt3Y Catalyst Films for the Oxygen Reduction Reaction," *ACS applied materials & interfaces*, vol. 12, no. 4, pp. 4454–4462, 2020, doi: 10.1021/acsami.9b17817.

[41] P. Malacrida *et al.,* "Direct observation of the dealloying process of a platinum-yttrium nanoparticle fuel cell cathode and its oxygenated species during the oxygen reduction reaction," *Physical chemistry chemical physics : PCCP*, vol. 17, no. 42, pp. 28121–28128, 2015, doi: 10.1039/c5cp00283d.

[42] N. Lindahl *et al.,* "Fuel Cell Measurements with Cathode Catalysts of Sputtered Pt3 Y Thin Films," *ChemSusChem*, vol. 11, no. 9, pp. 1438–1445, 2018, doi: 10.1002/cssc.201800023.

[43] J. S. Kanady *et al.,* "Synthesis of Pt3Y and Other Early-Late Intermetallic Nanoparticles by Way of a Molten Reducing Agent," *Journal of the American Chemical Society*, vol. 139, no. 16, pp. 5672–5675, 2017, doi: 10.1021/jacs.7b01366.

[44] A. Jain *et al.,* "Commentary: The Materials Project: A materials genome approach to accelerating materials innovation," *APL Materials*, vol. 1, no. 1, p. 11002, 2013, doi: 10.1063/1.4812323.

[45] K. A. Persson, B. Waldwick, P. Lazic, and G. Ceder, "Prediction of solid-aqueous equilibria: Scheme to combine first-principles calculations of solids with experimental aqueous states," *Phys. Rev. B*, vol. 85, no. 23, p. 2569, 2012, doi: 10.1103/PhysRevB.85.235438.

[46] V. Jalan and E. J. Taylor, "Importance of Interatomic Spacing in Catalytic Reduction of Oxygen in Phosphoric Acid," *J. Electrochem. Soc.: Accelerated Brief Communication*, vol. 130, no. 11, pp. 2299–2302, 1983. [Online]. Available: https://journals.aps.org/prl/pdf/10.1103/PhysRevLett.81.2819

[47] M. Mavrikakis, B. Hammer, and J. K. Nørskov, "Effect of Strain on the Reactivity of Metal Surfaces," *Physical Review Letters*, vol. 81, no. 13, pp. 2819–2822, 1998.

[48] B. Hammer and J. K. Nørskov, “Electronic factors determining the reactivity of metal surfaces,” *Surface Science*, vol. 343, pp. 211–220, 1995.

[49] J. C. Slater, “Atomic Radii in Crystals,” *The Journal of Chemical Physics*, vol. 41, no. 10, pp. 3199–3204, 1964, doi: 10.1063/1.1725697.

[50] S. J. Yoo *et al.,* “Pt3Y electrocatalyst for oxygen reduction reaction in proton exchange membrane fuel cells,” *International Journal of Hydrogen Energy*, vol. 37, no. 12, pp. 9758–9765, 2012, doi: 10.1016/j.ijhydene.2012.03.089.

[51] P. M. Martin, *Handbook of deposition technologies for films and coatings: Science, applications and technology,* 3rd ed. Amsterdam, Boston: Elsevier, 2010. [Online]. Available: http://search.ebscohost.com/login.aspx?direct=true&scope=site&db=nlebk&db=nlabk&AN=334611

[52] J. E. Greene, “Review Article: Tracing the recorded history of thin-film sputter deposition: From the 1800s to 2017,” *Journal of Vacuum Science & Technology A: Vacuum, Surfaces, and Films*, vol. 35, no. 5, 05C204, 2017, doi: 10.1116/1.4998940.

[53] K. Wasa, I. Kanno, and H. Kotera, Eds., *Handbook of sputter deposition technology: Fundamentals and applications for functional thin films, nano-materials and MEMS,* 2nd ed. Amsterdam u. a.: Elsevier/Andrew, 2012.

[54] H. Frey and H. R. Khan, *Handbook of Thin-Film Technology*. Berlin, Heidelberg: Springer Berlin Heidelberg, 2015. Accessed: Feb. 16 2020.

[55] E. S. R. Gopal, Ed., *Specific Heats at Low Temperatures*. Boston, MA: Springer US, 1966.

[56] Ye, Zhang, Feng, Ge, and Jiao, “Structural and electrical properties of a metallic rough-thin-film system deposited on liquid substrates,” *Physical review. B, Condensed matter*, vol. 54, no. 20, pp. 14754–14757, 1996, doi: 10.1103/PhysRevB.54.14754.

[57] H. Wender, P. Migowski, A. F. Feil, S. R. Teixeira, and J. Dupont, “Sputtering deposition of nanoparticles onto liquid substrates: Recent advances and future trends,” *Coordination Chemistry Reviews*, vol. 257, 17-18, pp. 2468–2483, 2013, doi: 10.1016/j.ccr.2013.01.013.

[58] M. T. Nguyen and T. Yonezawa, “Sputtering onto a liquid: interesting physical preparation method for multi-metallic nanoparticles,” *Science and Technology of Advanced Materials*, vol. 19, no. 1, pp. 883–898, 2018, doi: 10.1080/14686996.2018.1542926.

[59] L. Deng *et al.,* “Preparation and Growth Mechanism of Pt/Cu Alloy Nanoparticles by Sputter Deposition onto a Liquid Polymer,” *Langmuir : the ACS journal of surfaces and colloids*, vol. 35, no. 25, pp. 8418–8427, 2019, doi: 10.1021/acs.langmuir.9b01112.

[60] Y. Hatakeyama, T. Morita, S. Takahashi, K. Onishi, and K. Nishikawa, “Synthesis of Gold Nanoparticles in Liquid Polyethylene Glycol by Sputter Deposition and Temperature Effects on their Size and Shape,” *J. Phys. Chem. C*, vol. 115, no. 8, pp. 3279–3285, 2011, doi: 10.1021/jp110455k.

[61] H. Wender *et al.,* “Sputtering onto Liquids: From Thin Films to Nanoparticles,” *J. Phys. Chem. C*, vol. 115, no. 33, pp. 16362–16367, 2011, doi: 10.1021/jp205390d.

[62] T. Tsuda, A. Imanishi, T. Torimoto, and S. Kuwabata, “Nanoparticle Preparation in Room-Temperature Ionic Liquid under Vacuum Condition,” in *Ionic Liquids: Theory, Properties, New Approaches*, A. Kokorin, Ed., Rijeka: InTech, 2011, pp. 549–565. Accessed: Feb. 9 2020.

[63] I. Y. Cha, S. J. Yoo, and J. H. Jang, “Recent Progress in Nanoparticle Synthesis via Liquid Medium Sputtering and its Applications,” *Journal of Electrochemical Science and Technology*, vol. 7, no. 1, pp. 13–26, 2016, doi: 10.5229/JECST.2016.7.1.19.

[64] H. Wender *et al.,* “Ionic Liquid Surface Composition Controls the Size of Gold Nanoparticles Prepared by Sputtering Deposition,” *J. Phys. Chem. C*, vol. 114, no. 27, pp. 11764–11768, 2010, doi: 10.1021/jp102231x.

[65] T. Torimoto, K.-i. Okazaki, T. Kiyama, K. Hirahara, N. Tanaka, and S. Kuwabata, “Sputter deposition onto ionic liquids: Simple and clean synthesis of highly dispersed ultrafine metal nanoparticles,” *Appl. Phys. Lett.*, vol. 89, no. 24, p. 243117, 2006, doi: 10.1063/1.2404975.

[66] K.-i. Okazaki, T. Kiyama, K. Hirahara, N. Tanaka, S. Kuwabata, and T. Torimoto, “Single-step synthesis of gold-silver alloy nanoparticles in ionic liquids by a sputter deposition technique,” *Chemical communications (Cambridge, England)*, no. 6, pp. 691–693, 2008, doi: 10.1039/b714761a.

[67] Y. Hatakeyama, K. Onishi, and K. Nishikawa, “Effects of sputtering conditions on formation of gold nanoparticles in sputter deposition technique,” *RSC Adv.*, vol. 1, no. 9, p. 1815, 2011, doi: 10.1039/c1ra00688f.

[68] E. Vanecht, K. Binnemans, J. W. Seo, L. Stappers, and J. Fransaer, “Growth of sputter-deposited gold nanoparticles in ionic liquids,” *Physical chemistry chemical physics : PCCP*, vol. 13, no. 30, pp. 13565–13571, 2011, doi: 10.1039/c1cp20552h.

[69] Y. Hatakeyama, S. Takahashi, and K. Nishikawa, “Can Temperature Control the Size of Au Nanoparticles Prepared in Ionic Liquids by the Sputter Deposition Technique?,” *J. Phys. Chem. C*, vol. 114, no. 25, pp. 11098–11102, 2010, doi: 10.1021/jp102763n.

[70] I. Y. Cha *et al.,* “Synthesis and growth mechanism of carbon-supported nanoparticle catalysts by physical vapor deposition onto a liquid medium substrate,” *Applied Surface Science*, vol. 471, pp. 1083–1087, 2019, doi: 10.1016/j.apsusc.2018.12.144.

[71] T. Tsuda *et al.,* “Electrocatalytic Activity of Platinum Nanoparticles Synthesized by Room-Temperature Ionic Liquid-Sputtering Method,” *Electrochemistry*, vol. 77, no. 8, pp. 693–695, 2009, doi: 10.5796/electrochemistry.77.693.

[72] H. Meyer, M. Meischein, and A. Ludwig, “Rapid Assessment of Sputtered Nanoparticle Ionic Liquid Combinations,” *ACS combinatorial science*, vol. 20, no. 4, pp. 243–250, 2018, doi: 10.1021/acscombsci.8b00017.

[73] Y. Oda, K. Hirano, K. Yoshii, S. Kuwabata, T. Torimoto, and M. Miura, “Palladium Nanoparticles in Ionic Liquid by Sputter Deposition as Catalysts for Suzuki–Miyaura Coupling in Water,” *Chem. Lett.*, vol. 39, no. 10, pp. 1069–1071, 2010, doi: 10.1246/cl.2010.1069.

[74] S. Suzuki *et al.,* “Compositional control of AuPt nanoparticles synthesized in ionic liquids by the sputter deposition technique,” *CrystEngComm*, vol. 14, no. 15, p. 4922, 2012, doi: 10.1039/c2ce25235j.

[75] D. König, K. Richter, A. Siegel, A.-V. Mudring, and A. Ludwig, “High-Throughput Fabrication of Au-Cu Nanoparticle Libraries by Combinatorial Sputtering in Ionic Liquids,” *Adv. Funct. Mater.*, vol. 24, no. 14, pp. 2049–2056, 2014, doi: 10.1002/adfm.201303140.

[76] K. Manojkumar, A. Sivaramakrishna, and K. Vijayakrishna, “A short review on stable metal nanoparticles using ionic liquids, supported ionic liquids, and poly(ionic liquids),” *Journal of nanoparticle research : an interdisciplinary forum for nanoscale science and technology*, vol. 18, no. 4, p. 15, 2016, doi: 10.1007/s11051-016-3409-y.

[77] T. Suzuki, K.-i. Okazaki, T. Kiyama, S. Kuwabata, and T. Torimoto, “A Facile Synthesis of AuAg Alloy Nanoparticles Using a Chemical Reaction Induced by Sputter Deposition of Metal onto Ionic Liquids,” *Electrochemistry*, vol. 77, no. 8, pp. 636–638, 2009, doi: 10.5796/electrochemistry.77.636.

[78] Y. Hatakeyama, M. Okamoto, T. Torimoto, S. Kuwabata, and K. Nishikawa, “Small-Angle X-ray Scattering Study of Au Nanoparticles Dispersed in the Ionic Liquids 1-Alkyl-3-methylimidazolium Tetrafluoroborate,” *J. Phys. Chem. C*, vol. 113, no. 10, pp. 3917–3922, 2009, doi: 10.1021/jp807046u.

[79] C. Verma, E. E. Ebenso, and M. A. Quraishi, “Transition metal nanoparticles in ionic liquids: Synthesis and stabilization,” *Journal of Molecular Liquids*, vol. 276, pp. 826–849, 2019, doi: 10.1016/j.molliq.2018.12.063.

[80] S. Wegner and C. Janiak, “Metal Nanoparticles in Ionic Liquids,” *Topics in current chemistry (Cham)*, vol. 375, no. 4, p. 65, 2017, doi: 10.1007/s41061-017-0148-1.

[81] A. Karatutlu, A. Barhoum, and A. Sapelkin, “Liquid-phase synthesis of nanoparticles and nanostructured materials,” in *Emerging Applications of Nanoparticles and Architecture Nanostructures*: Elsevier, 2018, pp. 1–28.

[82] M. Seipenbusch, “Interparticle forces in Nanoparticle Agglomerates,” Karlsruhe Institute of Technology. Accessed: Mar. 28 2020. [Online]. Available: https://link.springer.com/content/pdf/10.1007/s11051-016-3362-9.pdf

[83] M. Gubernat, J. Tomala, W. Frohs, A. Fraczek-Szczypta, and S. Blazewicz, “De-agglomeration and homogenisation of nanoparticles in coal tar pitch-based carbon materials,” *Journal of nanoparticle research : an interdisciplinary forum for nanoscale science and technology*, vol. 18, p. 56, 2016, doi: 10.1007/s11051-016-3362-9.

[84] P.-C. Aïtcin and R. J. Flatt, Eds., *Science and technology of concrete admixtures*. Amsterdam, Boston, Cambridge, UK, Heidelberg: Elsevier, 2016.

[85] J. H. Adair, E. Suvaci, and J. Sindel, “Surface and Colloid Chemistry,” in *Encyclopedia of Materials: Science and Technology*: Elsevier, 2001, pp. 1–10.

[86] K. Richter, A. Birkner, and A.-V. Mudring, “Stabilizer-free metal nanoparticles and metal-metal oxide nanocomposites with long-term stability prepared by physical vapor deposition into ionic liquids,” *Angewandte Chemie (International ed. in English)*, vol. 49, no. 13, pp. 2431–2435, 2010, doi: 10.1002/anie.200901562.

[87] D. R. MacFarlane, J. M. Pringle, and M. Kar, *Fundamentals of ionic liquids*. Weinheim, Germany: Wiley-VCH, 2017. [Online]. Available: http://search.ebscohost.com/login.aspx?direct=true&scope=site&db=nlebk&AN=1570250

[88] A. S. Pensado and A. A. H. Pádua, “Solvation and stabilization of metallic nanoparticles in ionic liquids,” *Angewandte Chemie (International ed. in English)*, vol. 50, no. 37, pp. 8683–8687, 2011, doi: 10.1002/anie.201103096.

[89] R. R. Deshmukh, R. Rajagopal, and K. V. Srinivasan, “Ultrasound promoted C-C bond formation: Heck reaction at ambient conditions in room temperature ionic liquids,” *Chemical communications (Cambridge, England)*, no. 17, pp. 1544–1545, 2001, doi: 10.1039/b104532f.

[90] P. Migowski and J. Dupont, “Catalytic applications of metal nanoparticles in imidazolium ionic liquids,” *Chemistry (Weinheim an der Bergstrasse, Germany)*, vol. 13, no. 1, pp. 32–39, 2007, doi: 10.1002/chem.200601438.

[91] J. Dupont and J. D. Scholten, “On the structural and surface properties of transition-metal nanoparticles in ionic liquids,” *Chemical Society reviews*, vol. 39, no. 5, pp. 1780–1804, 2010, doi: 10.1039/b822551f.

[92] A. D. Pomogaĭlo and V. N. Kestel'man, *Metallopolymer nanocomposites*. Berlin: Springer, 2005. Accessed: Mar. 29 2020.

[93] R. B. Grubbs, “Roles of Polymer Ligands in Nanoparticle Stabilization,” *Polymer Reviews*, vol. 47, no. 2, pp. 197–215, 2007, doi: 10.1080/15583720701271245.

[94] O. Aschenbrenner, S. Supasitmongkol, M. Taylor, and P. Styring, “Measurement of vapour pressures of ionic liquids and other low vapour pressure solvents,” *Green Chem.*, vol. 11, no. 8, p. 1217, 2009, doi: 10.1039/b904407h.

[95] S. Liufu, H. Xiao, and Y. Li, “Investigation of PEG adsorption on the surface of zinc oxide nanoparticles,” *Powder Technology*, vol. 145, no. 1, pp. 20–24, 2004, doi: 10.1016/j.powtec.2004.05.007.

[96] G. Nabiyouni, A. Barati, and M. Saadat, “Surface Adsorption of Polyethylene Glycol and Polyvinyl Alcohol with Variable Molecular Weights on Zinc Oxide Nanoparticles,” *Iranian Journal of Chemical Engineering*, vol. 8, no. 1, pp. 20–30, 2011.

[97] Royal Society of Chemistry, *Platinum - Element information, properties and uses | Periodic Table.* [Online]. Available: https://www.rsc.org/periodic-table/element/78/platinum (accessed: Feb. 24 2020).

[98] P. Villars and K. Cenzual, *Pt3Y (YPt3) Crystal Structure: Datasheet from "PAULING FILE Multinaries Edition – 2012" in SpringerMaterials (https://materials.springer.com/isp/crystallographic/docs/sd_0528792)*: Springer-Verlag Berlin Heidelberg & Material Phases Data System (MPDS), Switzerland & National Institute for Materials Science (NIMS), Japan. [Online]. Available: https://materials.springer.com/isp/crystallographic/docs/sd_0528792

[99] T. Torimoto *et al.,* “Ultrathin oxide shell coating of metal nanoparticles using ionic liquid/metal sputtering,” *J. Mater. Chem. A*, vol. 3, no. 11, pp. 6177–6186, 2015, doi: 10.1039/c4ta06643j.

[100] K. Yoshii, T. Tsuda, T. Arimura, A. Imanishi, T. Torimoto, and S. Kuwabata, “Platinum nanoparticle immobilization onto carbon nanotubes using Pt-sputtered room-temperature ionic liquid,” *RSC Adv.*, vol. 2, no. 22, p. 8262, 2012, doi: 10.1039/c2ra21243a.

[101] J. R. Ferraro, C. W. Brown, and K. Nakamoto, *Introductory Raman spectroscopy,* 2nd ed. Amsterdam, Boston: Academic Press, 2003. [Online]. Available: http://site.ebrary.com/lib/alltitles/docDetail.action?docID=10186813

[102] T. Dieing, O. Hollricher, and J. Toporski, *Confocal Raman Microscopy*. Berlin, Heidelberg: Springer Berlin Heidelberg, 2011. Accessed: Apr. 13 2020.

[103] T. Owen, “Fundamentals of UV-visible spectroscopy: Primer,” 2000.

[104] H. Bubert and H. Jenett, *Surface and thin film analysis: Principles, instrumentation, applications*. Weinheim: Wiley-VCH, 2002. Accessed: Feb. 12 2020.

[105] D. B. Williams and C. B. Carter, *Transmission electron microscopy: A textbook for materials science,* 2nd ed. New York: Springer, 2008. Accessed: Feb. 12 2020.

[106] R. O. Müller, *Spectrochemical Analysis by X-Ray Fluorescence*. Boston, MA: Springer US, 1972. [Online]. Available: http://dx.doi.org/10.1007/978-1-4684-1797-5

[107] D. Brabazon and A. Raffer, “Advanced characterization techniques for nanostructures,” in *Micro & Nano Technologies Series, Emerging nanotechnologies for manufacturing*, W. Ahmed and M. J. Jackson, Eds., Amsterdam, Boston, Heidelberg, London, New York, Oxford, Paris, San Diego, San Francisco, Singapore, Sydney, Tokyo: William Andrew is an imprint of Elsevier, 2015, pp. 53–85. Accessed: Feb. 26 2020.

[108] L. Reimer, *Scanning Electron Microscopy: Physics of Image Formation and Microanalysis*. Berlin, Heidelberg, s.l.: Springer Berlin Heidelberg, 1998. [Online]. Available: http://dx.doi.org/10.1007/978-3-540-38967-5

[109] T. Li, A. J. Senesi, and B. Lee, “Small Angle X-ray Scattering for Nanoparticle Research,” *Chemical reviews*, vol. 116, no. 18, pp. 11128–11180, 2016, doi: 10.1021/acs.chemrev.5b00690.

[110] H. Schnablegger and Y. Sing, *The SAXS Guide: Getting acquainted with the principles,* 3rd ed. Austria, 2013.

[111] SasView 5.0.1 documentation, *sphere.* [Online]. Available: http://www.sasview.org/docs/user/models/sphere.html (accessed: Apr. 24 2020).

[112] J. Stetefeld, S. A. McKenna, and T. R. Patel, “Dynamic light scattering: a practical guide and applications in biomedical sciences,” *Biophysical reviews*, vol. 8, no. 4, pp. 409–427, 2016, doi: 10.1007/s12551-016-0218-6.

[113] W. Schärtl, *Light Scattering from Polymer Solutions and Nanoparticle Dispersions,* 1st ed. s.l.: Springer-Verlag, 2007. [Online]. Available: http://site.ebrary.com/lib/alltitles/docDetail.action?docID=10189364

[114] H.-H. Perkampus, *UV-VIS Spectroscopy and Its Applications*. Berlin, Heidelberg: Springer Berlin Heidelberg, 1992.

[115] Mettler-Toledo GmbH, “UV/Vis Spectrophotometry: Fundamentals and Applications,” 2015.

[116] S. Hofmann, *Auger- and X-Ray Photoelectron Spectroscopy in Materials Science*. Berlin, Heidelberg: Springer Berlin Heidelberg, 2013. Accessed: Feb. 12 2020.

[117] Thermo scientific XPS, *Carbon.* [Online]. Available: https://xpssimplified.com/elements/carbon.php (accessed: May 10 2020).

[118] J. F. Moulder and J. Chastain, Eds., *Handbook of X-ray photoelectron spectroscopy: A reference book of standard spectra for identification and interpretation of XPS data*. Eden Prairie, Minn.: Perkin-Elmer Corporation, 1992.

[119] C. Powell, “X-ray Photoelectron Spectroscopy Database XPS,Version 4.1, NIST Standard Reference Database 20,” 1989.

[120] R. Reichl and K. H. Gaukler, “An investigation of air-grown yttrium oxide and experimental determination of the sputtering yield and the inelastic mean free path,” *Applied Surface Science*, vol. 26, no. 2, pp. 196–210, 1986, doi: 10.1016/0169-4332(86)90005-X.

[121] N. Elgrishi, K. J. Rountree, B. D. McCarthy, E. S. Rountree, T. T. Eisenhart, and J. L. Dempsey, “A Practical Beginner’s Guide to Cyclic Voltammetry,” *J. Chem. Educ.*, vol. 95, no. 2, pp. 197–206, 2018, doi: 10.1021/acs.jchemed.7b00361.

[122] J. Nikolic, E. Expósito, J. Iniesta, J. González-Garcia, and V. Montiel, “Theoretical Concepts and Applications of a Rotating Disk Electrode,” *J. Chem. Educ.*, vol. 77, no. 9, p. 1191, 2000, doi: 10.1021/ed077p1191.

[123] R. W Raut, A. Sana Mohd. Haroon, Y. S Malghe, B. T Nikam, and S. B Kashid, “Rapid Biosynthesis Of Platinum And Palladium Metal Nanoparticles Using Root Extract Of Asparagus Racemosus Linn,” *AML*, vol. 4, no. 8, pp. 650–654, 2013, doi: 10.5185/amlett.2012.11470.

[124] A. Sennuga, J. van Marwijk, and C. G. Whiteley, “Ferroxidase activity of apoferritin is increased in the presence of platinum nanoparticles,” *Nanotechnology*, vol. 23, no. 3, p. 35102, 2012, doi: 10.1088/0957-4484/23/3/035102.

[125] F. Arockiya Aaarthi Rajathi and Subramanyam Nambaru, V. R. M., “Phytofabrication of nano-crystalline platinum particles by leaves of Cerbera manghas and its antibacterial efficacy,” *International Journal of Pharma and Bio Sciences*, vol. 5, no. 1, pp. 619–628, 2014.

[126] M. R. Luo, *Encyclopedia of Color Science and Technology*. New York, NY: Springer New York, 2016. Accessed: Feb. 24 2020. [Online]. Available: https://iolitec.de/sites/iolitec.de/files/2017-05/TDS%20IL-0029_UP%20BMIM%20BTA.pdf

[127] T. F. Tadros, “Formulation Science and Technology: Volume 4: Agrochemicals, Paints and Coatings and Food Colloids,” in *Formulation Science and Technology*,

Volume 4, *EBOOK PACKAGE COMPLETE 2018 : EBOOK PACKAGE COMPLETE 2018 English : EBOOK PACKAGE Physics, Chemistry, Materials Sc, Geosc 2018 : EBOOK PACKAGE Physics, Chem., Mat.Sc, Geosc 2018 English*, Berlin, Boston: De Gruyter. [Online]. Available: https://www.degruyter.com/doi/book/10.1515/9783110588002

[128] iolitec, *Technical Data Sheet: 1-Butyl-3-methylimidazolium bis(trifluoromethylsulfonyl)imide.* [Online]. Available: https://iolitec.de/sites/iolitec.de/files/2017-05/TDS%20IL-0029_UP%20BMIM%20BTA.pdf (accessed: Feb. 24 2020).

[129] R. Alcalde, M. Atilhan, and S. Aparicio, “Insights on 1-Butyl-3-methylimidazolium Bis(trifluoromethylsulfonyl)imide + Ethanol Liquid Mixtures: A Molecular Dynamics Approach,” *J. Chem. Eng. Data*, vol. 61, no. 8, pp. 2729–2737, 2016, doi: 10.1021/acs.jced.6b00132.

[130] Y. Zhang, J. R. G. Evans, and S. Yang, “Corrected Values for Boiling Points and Enthalpies of Vaporization of Elements in Handbooks,” *J. Chem. Eng. Data*, vol. 56, no. 2, pp. 328–337, 2011, doi: 10.1021/je1011086.

[131] T. L. Barr and S. Seal, “Nature of the use of adventitious carbon as a binding energy standard,” *Journal of Vacuum Science & Technology A: Vacuum, Surfaces, and Films*, vol. 13, no. 3, pp. 1239–1246, 1995, doi: 10.1116/1.579868.

[132] D. K. Singh, B. Rathke, J. Kiefer, and A. Materny, “Molecular Structure and Interactions in the Ionic Liquid 1-Ethyl-3-methylimidazolium Trifluoromethanesulfonate,” *The journal of physical chemistry. A*, vol. 120, no. 31, pp. 6274–6286, 2016, doi: 10.1021/acs.jpca.6b03849.

[133] Z. Liu, S. Z. El Abedin, and F. Endres, “Raman and FTIR spectroscopic studies of 1-ethyl-3-methylimidazolium trifluoromethylsulfonate, its mixtures with water and the solvation of zinc ions,” *Chemphyschem : a European journal of chemical physics and physical chemistry*, vol. 16, no. 5, pp. 970–977, 2015, doi: 10.1002/cphc.201402831.

[134] L. Chancelier, O. Boyron, T. Gutel, and C. Santini, “Thermal stability of imidazolium-based ionic liquids,” *Fr. Ukr. J. Chem.*, vol. 4, no. 1, pp. 51–64, 2016, doi: 10.17721/fujcV4I1P51-64.

[135] P. S. Kulkarni, L. C. Branco, J. G. Crespo, M. C. Nunes, A. Raymundo, and C. A. M. Afonso, “Comparison of physicochemical properties of new ionic liquids based on imidazolium, quaternary ammonium, and guanidinium cations,” *Chemistry (Weinheim an der Bergstrasse, Germany)*, vol. 13, no. 30, pp. 8478–8488, 2007, doi: 10.1002/chem.200700965.

[136] C. Maton, N. de Vos, and C. V. Stevens, “Ionic liquid thermal stabilities: decomposition mechanisms and analysis tools,” *Chemical Society reviews*, vol. 42, no. 13, pp. 5963–5977, 2013, doi: 10.1039/c3cs60071h.

[137] Y. Chen and T. Mu, “Thermal Stability of Ionic Liquids,” in *Encyclopedia of ionic liquids*, S. Zhang, Ed., Singapore: Springer, 2019, pp. 1–13.

[138] A. Z. Samuel and S. Umapathy, “Energy funneling and macromolecular conformational dynamics: a 2D Raman correlation study of PEG melting,” *Polym J*, vol. 46, no. 6, pp. 330–336, 2014, doi: 10.1038/pj.2014.10.

[139] J. L. Koenig and A. C. Angood, “Raman spectra of poly(ethylene glycols) in solution,” *J. Polym. Sci. A-2 Polym. Phys.*, vol. 8, no. 10, pp. 1787–1796, 1970, doi: 10.1002/pol.1970.160081013.

[140] E. A. Sagitova *et al.*, “Raman analysis of polyethylene glycols and polyethylene oxides,” *J. Phys.: Conf. Ser.*, vol. 999, p. 12002, 2018, doi: 10.1088/1742-6596/999/1/012002.

[141] C. G. Granqvist and R. A. Buhrman, "Ultrafine metal particles," *Journal of Catalysis*, vol. 47, no. 5, pp. 2200–2219, 1976, doi: 10.1063/1.322870.

[142] Kiss, L. B., J. Söderlund, G. A. Niklasson, and C. G. Granqvist, "New approach to the origin of lognormal size distributions of nanoparticles," *Nanotechnology*, vol. 10, pp. 25–28, 1999.

[143] Q. Abbas, "Understanding the UV-Vis Spectroscopy for Nanoparticles," *J Nanomater Mol Nanotechno*, vol. 8, no. 3, 2019.

[144] W. Raut Rajesh, Lakkakula Jaya, R., Kolekar Niranjan, S., Mendhulkar Vijay, D., and B. Kashid Sahebrao, "Phytosynthesis of Silver Nanoparticle Using Gliricidia sepium (Jacq.)," *Current Nanoscience*, no. 5, pp. 117–122, 2009.

[145] R. Brandiele *et al.,* "Facile synthesis of Pd3Y alloy nanoparticles for electrocatalysis of the oxygen reduction reaction," *Electrochimica Acta*, vol. 320, p. 134563, 2019, doi: 10.1016/j.electacta.2019.134563.

[146] T. B. Nguyen, T. D. Nguyen, Q. D. Nguyen, and T. T. Nguyen, "Preparation of platinum nanoparticles in liquids by laser ablation method," *Adv. Nat. Sci: Nanosci. Nanotechnol.*, vol. 5, no. 3, p. 35011, 2014, doi: 10.1088/2043-6262/5/3/035011.

[147] D. Tongsakul, K. Wongravee, C. Thammacharoen, and S. Ekgasit, "Enhancement of the reduction efficiency of soluble starch for platinum nanoparticles synthesis," *Carbohydrate research*, vol. 357, pp. 90–97, 2012, doi: 10.1016/j.carres.2012.04.012.

[148] A. H. Simon, "Sputter Processing," in *Handbook of Thin Film Deposition*: Elsevier, 2018, pp. 195–230.

[149] J. S. Coursey, Schwab D. J., J. J. Tsai, and R. A. Dragoset, *Atomic Weights and Isotopic Compositions with Relative Atomic Masses*.

[150] Y. Uwamino, A. Tsuge, T. Ishizuka, and H. Yamatera, "X-Ray Photoelectron Spectroscopy of Rare Earth Halides," *BCSJ*, vol. 59, no. 7, pp. 2263–2267, 1986, doi: 10.1246/bcsj.59.2263.

[151] J. Wiórkiewicz-Kuczera and A. Rabczenko, “Calculation of average values for C ・ C bond lengths and C ・ C ・ C bond angles. PCILO conformational study of n-butane with the newly found and other molecular geometries,” *Journal of Molecular Structure: THEOCHEM*, vol. 137, 1-2, pp. 31–41, 1986, doi: 10.1016/0166-1280(86)80083-5.

[152] G. S. Fonseca *et al.,* "Synthesis and characterization of catalytic iridium nanoparticles in imidazolium ionic liquids," *Journal of colloid and interface science*, vol. 301, no. 1, pp. 193–204, 2006, doi: 10.1016/j.jcis.2006.04.073.

[153] L. S. Ott, M. L. Cline, M. Deetlefs, K. R. Seddon, and R. G. Finke, "Nanoclusters in ionic liquids: evidence for N-heterocyclic carbene formation from imidazolium-based ionic liquids detected by (2)H NMR," *Journal of the American Chemical Society*, vol. 127, no. 16, pp. 5758–5759, 2005, doi: 10.1021/ja0423320.

[154] P. Peruzzo, A. Defina, H. M. Nepf, and R. Stocker, "Capillary interception of floating particles by surface-piercing vegetation," *Physical Review Letters*, vol. 111, no. 16, p. 164501, 2013, doi: 10.1103/PhysRevLett.111.164501.

[155] P. SINGH and D. D. JOSEPH, "Fluid dynamics of floating particles," *J. Fluid Mech.*, vol. 530, pp. 31–80, 1999, doi: 10.1017/S0022112005003575.

[156] M. B. Larosi, "Floating Together on the Top," *The Physics Teacher*, vol. 53, no. 2, pp. 93–94, 2015, doi: 10.1119/1.4905806.

[157] J. M. Doña Rodríguez, J. A. Herrera Melián, and J. Pérez Peña, "Determination of the Real Surface Area of Pt Electrodes by Hydrogen Adsorption Using Cyclic Voltammetry," *J. Chem. Educ.*, vol. 77, no. 9, p. 1195, 2000, doi: 10.1021/ed077p1195.

[158] R. Woods, “Hydrogen adsorption on platinum, iridium and rhodium electrodes at reduced temperatures and the determination of real surface area,” *Journal of Electroanalytical Chemistry and Interfacial Electrochemistry*, vol. 49, no. 2, pp. 217–226, 1974, doi: 10.1016/S0022-0728(74)80229-9.

[159] K. Shinozaki, J. W. Zack, R. M. Richards, B. S. Pivovar, and S. S. Kocha, “Oxygen Reduction Reaction Measurements on Platinum Electrocatalysts Utilizing Rotating Disk Electrode Technique,” *J. Electrochem. Soc.*, vol. 162, no. 10, F1144-F1158, 2015, doi: 10.1149/2.1071509jes.

[160] S. Trasatti and O. A. Petrii, “Real Surface Area Measurements in Electrochemistry,” *Pure & Appl. Chem*, vol. 63, no. 5, pp. 711–734, 1991.

[161] C. Wei *et al.,* “Recommended Practices and Benchmark Activity for Hydrogen and Oxygen Electrocatalysis in Water Splitting and Fuel Cells,” *Advanced materials (Deerfield Beach, Fla.)*, vol. 31, no. 31, e1806296, 2019, doi: 10.1002/adma.201806296.

[162] K. Wuttikid, N. Worayos, and K. Punyawudho, “Analysis of Catalyst Ink Compositions for Fabricating Membrane Electrode Assemblies in PEM Fuel Cells,” *CMUJNS*, vol. 16, no. 4, 2017, doi: 10.12982/CMUJNS.2017.0022.

Appendices

A Sample overview

Table 13: Sample and sputtering parameter overview.

Sample name	**Target material**	**Wafer**	**Substrate material**	***t* [s]**	**p_{base} [10^{-7} mbar]**	**p_{Ar} [10^{-3} mbar]**	***P* [W]**	***U* [V]**	***I* [A]**	**W_d [cm]**	**Purpose**
B3101	Pt	1-inch Si	[Bmim] [Tf_2N]	120	8.0	6.6	50	-	-	5	1
B1102	Pt_3Y	Si-wafer	Si-wafer	240	1.3	6.6	50	355	0.154	8	1
B1902	Pt_3Y	1-inch Si	[Emim] [Tf_2N]	300	9.8	6.6	50	332	0.153	8	2
B2002	Pt_3Y	1-inch Si	[Emim] [OTf]	300	7.1	6.6	50	329	0.152	8	2, 4
B2102	Pt_3Y	1-inch Si	[Emim] [FAP]	300	7.6	6.6	50	326	0.155	8	2
B2402	Pt_3Y	1-inch Si	[Dmim] [Tf_2N]	300	3.0	6.6	50	328	0.154	8	2
B1003	Pt_3Y	1-inch Si	[Emim] [OTf]	3x300	5.6	6.6	50	324	0.154	8	3, 4
B1203	Pt_3Y	1-inch Si	[Emim] [OTf]	30	4.9	6.6	50	325	0.155	4	4
B1303	Pt_3Y	1-inch Si	[Emim] [OTf]	3x300	7.6	6.6	50	324	0.155	8	5
B2003	Pt	1-inch fused silica	[Emim] [OTf]	3x300	3.2	6.9	50	437	0.114	8	6, 8
B2303	Pt	1-inch fused silica	[Dmim] [OTf]	3x300	2.8	7.0	50	432	0.115	8	6
B2403	Pt	1-inch fused silica	[Dmim] [Tf_2N]	3x300	6.2	7.0	50	427	0.117	8	6
B2503	Pt	1-inch fused silica	PEG 600	3x300	6.2	7.1	50	424	0.119	8	6, 8, 9
B0804	Pt_3Y	1-inch fused silica	PEG 600	3x300	9.2	7.1	50	322	0.155	8	7
B1004	Pt	1-inch fused silica	[Emim] [OTf]	3x300	7.3	7.1	50	423	0.118	8	8
B1304	Pt	1-inch fused silica	PEG 600	3x300	2.8	7.2	50	422	0.119	8	8

Table 13 continued: Sample and sputtering parameter overview.

Sample name	**Target material**	**Wafer**	**Substrate material**	***t* [s]**	**p_{base} [10^{-7} mbar]**	**p_{Ar} [10^{-3} mbar]**	***P* [W]**	***U* [V]**	***I* [A]**	**W_d [cm]**	**Purpose**
B1404	Pt	1-inch fused silica	PEG 600	3x300	6.5	7.2	20	373	0.051	5	9
B1504	Pt	1-inch fused silica	PEG 600	3x300	6.4	7.1	65	444	0.145	8	9
B2904	Pt	1-inch fused silica	PEG 600	3x300	6.6	6.8	50	421	0.120	8	10
B3004	Pt_3Y	1-inch fused silica	PEG 600	3x300	8.2	7.0	50	331	0.153	8	10
B0505	Pt_3Y	1-inch fused silica	PEG 600	300	6.8	6.9	50	334	0.152	6	4

Purpose	
1	Pre-Investigations
2	Influence of the type of liquid substrate for Pt_3Y
3	Further analysis methods for Pt_3Y sputtered onto [Emim] [OTf]
4	Influence of sputtering time and sputtering distance
5	XRF measurement
6	Influence of the type of liquid substrate for Pt
7	Test of PEG 600 as liquid substrate for Pt_3Y
8	Influence of post heat-treatment
9	Influence of sputtering power
10	Ink preparation

B EDX quantification

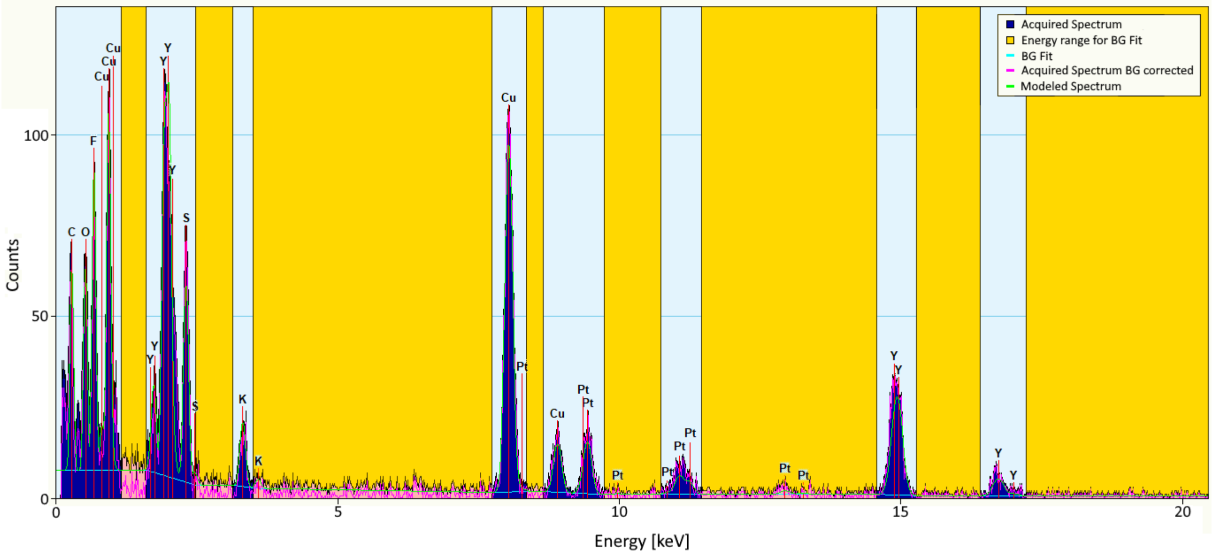

Figure 61: EDX quantification example for a sample containing C, O, F, Cu, Y, S, K and Pt (Pt_3Y sputtered onto [Emim] [OTf] immobilized on Cu-TEM grid).

C Determination of the ECSA via hydrogen adsorption

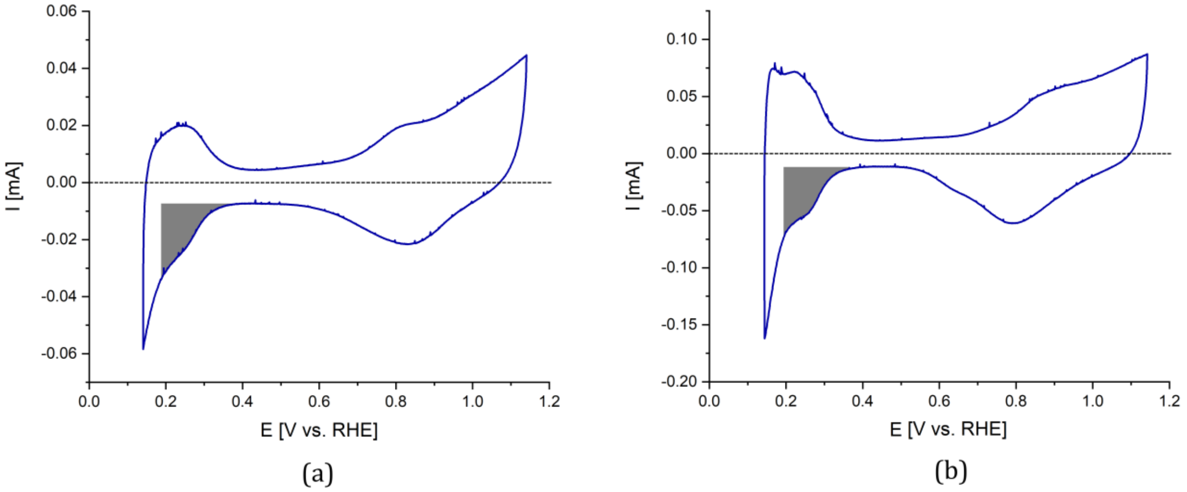

Figure 62: ECSA determination from CVs of carbon supported catalysts on GCE: (a) Sputtered Pt; (b) Sputtered Pt_3Y.

The ECSA for the Pt catalyst is calculated using equation (C1).

$$\mathrm{ECSA} = \frac{1}{\theta} \cdot \frac{\frac{1}{v} \cdot \int_{\mathrm{H-ads}} I \,\mathrm{d}U}{210\,\frac{\mu\mathrm{C}}{\mathrm{cm}^2}} = \frac{1}{0.77} \cdot \frac{\frac{1}{10 \cdot 10^{-3}\,\frac{\mathrm{V}}{\mathrm{s}}} \cdot 1.28 \cdot 10^{-6}\,\frac{\mathrm{C} \cdot \mathrm{V}}{\mathrm{s}}}{210 \cdot 10^{-6}\,\frac{\mathrm{C}}{\mathrm{cm}^2}} = 0.79\ \mathrm{cm}^2 \tag{C1}$$

The ECSA for the Pt_3Y catalyst is calculated using equation (C2).

$$\mathrm{ECSA} = \frac{1}{\theta} \cdot \frac{\frac{1}{v} \cdot \int_{\mathrm{H-ads}} I \,\mathrm{d}U}{210\,\frac{\mu\mathrm{C}}{\mathrm{cm}^2}} = \frac{1}{0.77} \cdot \frac{\frac{1}{10 \cdot 10^{-3}\,\frac{\mathrm{V}}{\mathrm{s}}} \cdot 2.54 \cdot 10^{-6}\,\frac{\mathrm{C} \cdot \mathrm{V}}{\mathrm{s}}}{210 \cdot 10^{-6}\,\frac{\mathrm{C}}{\mathrm{cm}^2}} = 1.57\ \mathrm{cm}^2 \tag{C2}$$